IOWA STATE UNIVERSITY
Digital Repository

2018

Combined Transmission-Distribution System (CoTDS) co-simulation modeling and its applications for dynamic studies

Ramakrishnan Venkatraman
Iowa State University

Follow this and additional works at: https://lib.dr.iastate.edu/etd

 Part of the Electrical and Electronics Commons

Combined Transmission-Distribution System (CoTDS) co-simulation modeling and its applications for dynamic studies

by

Ramakrishnan Venkatraman

A dissertation submitted to the graduate faculty

in partial fulfillment of the requirements for the degree of

DOCTOR OF PHILOSOPHY

Major: Electrical Engineering (Electric Power and Energy Systems)

Program of Study Committee:
Venkataramana Ajjarapu, Co-major Professor
Siddhartha Khaitan, Co-major Professor
Ian Dobson
Umesh Vaidya
Fritz Keinert

The student author, whose presentation of the scholarship herein was approved by the program of study committee, is solely responsible for the content of this dissertation. The Graduate College will ensure this dissertation is globally accessible and will not permit alterations after a degree is conferred.

Iowa State University

Ames, Iowa

2018

TABLE OF CONTENTS

LIST OF TABLES

LIST OF FIGURES

ABSTRACT

Combined Transmission and Distribution Systems (CoTDS) simulation requires development of algorithms and software that are numerically stable and at the same time accurately simulate dynamic events that can occur in practical systems. The dynamic behavior of transmission and distribution systems are vastly different. With the increased deployment of distribution generation, especially power electronic inverters, the complexity is further increased. The time scales of simulation can be orders of magnitude apart making the combined simulation extremely challenging. This has led to increased research in applying coupled simulation (also referred to as co-simulation) techniques for integrated simulation of the two systems.

In this thesis, two methods for co-simulation of CoTDS are proposed using parallel and series computation with integration impact on numerical convergence. The proposed co-simulation methodology is validated against commercial EMTP software. The results show the limits and benefits of applying co-simulation by using test transmission and distribution systems. A detailed phasor domain Distribution Generation (DG) inverter model is developed for power system dynamic simulation using which the effectiveness of the proposed co-simulation methodology is demonstrated in dynamic studies.

The co-simulation method is then applied to model reduction where the CoTDS based dynamic load modeling with distributed load serves as a guiding tool to calculate some of the key aggregated WECC Composite Load Model (CLM) parameters. As a further addition, a Reduced Distribution System Model (RDSM) is proposed with a new single-phase A/C motor model for the WECC CLM with fractional stalling and recovery. Such a model can be used for developing measurement based control schemes that can mitigate events such as fault-induced delayed voltage recovery in distribution systems.

With the addition of DG in the WECC CLM, the co-simulation is applied for studying the effect of high DG penetration on bulk transmission system dynamics in reference to the recommendations of the IEEE 1547 standard for interconnecting distributed energy resources with electric power systems.

CHAPTER 1.   INTRODUCTION

1.1   Project Background

The modern distribution systems are becoming more active with the increased deployment of Distribution Generation (DG), especially with power-electronic inverters and smart grid control technologies which add a new dimension to system dynamics. From the transmission system perspective, the North American Electric Reliability Corporation (NERC) standard TPL-001-4 [1], Section R2.4.1 states that: "System peak load levels shall include a load model which represents the expected dynamic behavior of loads that could impact the study area, considering the behavior of induction motor loads." These are some factors that have necessitated a new interest amongst researchers in modeling system dynamics for an integrated simulation of transmission and distribution systems and to develop algorithms that are numerically stable and at the same time accurately simulate dynamic events that can occur in practical systems.

It is quite a challenging task to simulate the transient behavior with both the transmission and distribution systems. Integration of transmission and distribution system will result in huge set of dynamic equations. Inclusion of distribution system components in detail will lead to very large set of Differential-Algebraic Equations (DAE) and it becomes computationally intractable. Conventional single domain simulators for transmission and distribution systems have been developed and optimized over several years, and applying them to combined simulation often compromises the numerical behavior [2].

The principal issue in an integrated approach to transmission and distribution system simulation is that the dynamic components in bulk transmission and in distribution systems

can have different time constants. To accurately capture the dynamics, the integration time step chosen for the whole system must be according to the smallest time constant which makes the whole simulation very slow. This has led to increased research in applying coupled simulation (also referred to as co-simulation) techniques for integrated simulation of the two systems.

In co-simulation the variables establishing the mutual influence of sub-systems are exchanged at fixed time points. This results in continuous variables being approximated by constant extrapolation (for the exchanged variables). In power systems, this idea is exploited by exchanging variable information at the transmission - distribution system boundary.

A power system comprises of the components of the transmission system and distribution systems. Transmission systems primarily include generators, exciters, governors, power system stabilizers and the network itself. The loads are located in the distribution systems and are made up of various load components such as static loads (ZIP loads), induction motor loads and reactive shunt compensators.

Loads like induction motors needs to be more accurately modeled because of their very critical dynamic characteristics that can result in blackouts due to Fault Induced Delayed Voltage Recovery (FIDVR). It has been studied in recent research that it is not sufficient to represent the induction motor as a single type, but needs 4 different motor types to represent the induction motor load. The Western Electric Co-ordinating Council (WECC) Composite Load Model (CLM) is an aggregated model that captures the average behaviour of all the individual loads spread across the distribution system. This is helpful in bulk transmission system modeling where average behavior dynamic studies needs to be performed for reliability and planning evaluations.

However, the challenge is the difficulty to set up equivalents satisfying the dynamic behavior of the transmission system load represented by the distribution systems at the sub-station. The WECC CLM being one of the most comprehensive load models used in transmission system dynamic studies, is represented by 132 parameters. Since in reality,

there are numerous individual loads of various types, it is a very complex task to determine the parameters of such a load model and ascertain the dynamic performance of the system under study. Due to the lack of a systematic approach to determine the parameter values, most often only generic values are used for the parameters.

With the proliferation of renewable energy sources, DG modeling has become a significant topic of research. Photo-Voltaic (PV) arrays, wind, fuel-cells, biomass and geothermal, steam or gas turbines and reciprocation internal combustion engines are some examples of DG units in operation. Detailed sine-wave dynamic models are widely used in development of power electronic circuits and controls. However, modeling of DGs has been primarily limited to steady-state models in power systems. But with the recent increase in DG penetration, there is a great need to develop efficient dynamic models that can be used in power system studies.

Furthermore, with increasing penetration of DGs in the distribution system, the voltage support on the distribution line is provided by many different sources and so the interaction of the grid with the various DERs and the loads needs to be evaluated for overall grid reliability. Since both the DERs and loads are connected on the distribution line, there is an inherent dependency of the operation of one on the other and proper models are required for representing the dynamic nature of the distribution system to analyze its effect on the transmission system.

So, it can be seen that there is a compelling necessity for an integrated platform to study the performance of transmission and distribution systems. Commercially available software are not suitable as these are optimized for either transmission system (mainly based on balanced phasor domain methods) or distribution system studies (EMTP or steady state power flow based). Currently, there are software like PSS®E, PSLF, and PSAT for the transmission system analysis and tools like OpenDSS and Gridlab-D for the distribution system analysis. But there are hardly any efficient commercial software for combined study

of transmission and distribution systems with the exception of time-consuming Electro-Magnetic Transient Program (EMTP) simulators like EMTP-RV, PSCAD and MATLAB Simscape PowerSystems. Software tools such as DigSILENT, PSS®SINCAL is capable of simulations in different time scales but uses EMT simulation function for detailed dynamic simulation.

Therefore, there is a great need to develop algorithms that enables the dynamic study of transmission and distribution systems in an integrated platform and enabling the estimation of parameters of an aggregated load model. Co-simulation methodologies aim to fulfill these needs by modeling multi-domain sub-systems across multiple simulation tools, while acting as one integral simulation platform that addresses the study of the total system.

1.2   Literature Review

Coupled simulation also referred to as co-simulation can broadly be classified into three categories. First [3, 4], is the capability to solve the power flow of the two systems for obtaining a steady state power flow solution which is particularly suited for optimal power flow, planning algorithms, etc. Here, generally there are no dynamics involved. The second category [5, 6, 2], is to integrate the controls and communications into the steady state power flows for energy management and market clearance. In this category, the dynamics of the system are related to hourly or daily load and generation profiles. Recent developments in co-simulation including GridMat [7], Bus.py [8] cater mainly to the first and second categories. The third category, which is the focus area of this paper, deals with the detailed transient behavior and the interaction of the two systems.

One approach towards transient co-simulation is to use a combination of Transient-Stability type as the main simulator and embedding an EMTP type simulator by an inner calculation loop. In literature, co-simulation of two network systems for transient analysis using this approach are presented in [9] by integrating electromechanical and EMT simulation of transmission systems. The concept is to perform detailed study on a small part

of a large system by dividing the whole system into external phasor domain network and detailed internal networks which interface through Thévenin and Norton equivalents at the boundary. This work is extended in [10, 11, 12] where an EMT-Transient Stability hybrid simulation architecture is proposed. The method is effective but still requires computationally intensive EMTP for the detailed internal network. A similar approach, but extending to a frequency dependent network equivalent is presented in [13].

In [14], dynamic simulation of combined transmission and distribution systems is introduced to address the computational burden of representing all distribution networks in detail. A domain decomposition approach based on level of participation of distribution networks in system dynamics is adopted to distinguish between selecting a simple or detailed model. The networks are however, still solved using the complete set of DAE in phasor domain.

In [15], a co-simulation framework by two independent EMT simulations with a time-delay compensation algorithm is proposed to improve the co-simulation accuracy, but is not suitable for large distribution networks. In [16, 17], a novel three-phase dynamic analyzer algorithm is presented that enables the study of electromechanical transients in unbalanced networks without using EMTP programs. The idea behind this approach is to accurately simulate electromechanical transients using 3-phase approach. However, the method actually solves the system's differential equations in dqo reference frame for instantaneous values and recovers the abc values to solve the network algebraic equations and so the solution, although maintaining higher accuracy will inherently exhibit higher simulation times.

In [18], a dynamic simulation approach that links existing transmission and distribution dynamic simulators through an open-source co-simulation framework (FNCS [19]), is presented. This concept of dynamic co-simulation is highly relevant to the ongoing research in this area. However, there is no detailed analysis on the convergence aspect of dynamic co-simulation. The authors mention that they use a small simulation time step to avoid numerical errors and non-convergence problems. The aspects of stability and convergence

of the numerical methods was not described and the impact of the integration time step in co-simulation is also not studied in detail in any of the existing literature. In addition when the distribution system differential algebraic equations are solved as an entire sub-system it can make the numerical solution tedious and cumbersome.

In all of the existing literature for CoTDS dynamic co-simulation, the distribution system dynamics relies either on complete system simulation or solving the entire distribution system dynamics. In this paper a novel scheme is proposed to utilize a three-phase distribution system power flow solver and interfacing it with a node-level dynamic component modeling. This is then used as the distribution system dynamic model for CoTDS dynamic co-simulation.

In addition to the advantage of employing multiple simulation tools to solve the sub-systems at different time-scales, the co-simulation algorithms in literature also support parallel computation architecture. While parallel computing is beneficial, it is also important to study the impact of the integration time-step on the numerical stability and convergence. In existing literature on co-simulation, there is no detailed analysis on the aspect of numerical convergence.

To study the dynamics of DG in power systems, we need an appropriate dynamic model that can be used in performing time-domain simulations. On the one hand, there are detailed sine-wave models that are used in power electronics circuits and control systems. The detailed sine-wave modeling required for fast switching transient studies. A review of DG inverter models has been presented from a power electronic perspective in [20]. However, in power systems, to perform dynamic simulations in an effective manner, a phasor domain model is required.

A Solar Photo Voltaic Generator (SPVG) based DG model is described in [21] which is a simple model where the d- and the q- axis currents are algebraically calculated and sent through a first order low pass filter into the network. This model does not capture the detailed dynamics of the DG and therefore is limited for performing dynamic studies. [22]

uses this model for deriving the WECC PV system model parameters. This model is also used in and [23] for studying the impacts of high levels of distributed PV and load dynamics on bulk power transient stability

In [24], the limitation of this model has been shown in capturing the detailed dynamic behavior. An alternate model has been proposed using a controlled voltage source converter representation for positive sequence simulation. This model although is shown to capture the details, but is not based on the original control loop of the actual sine-wave model and so requires tuning for each dynamic event. Therefore, there is a need for developing a detailed phasor domain DG model that can be used in power system simulations. However, to overcome numerical issues due to fast dynamics of the DG model, the CoTDS co-simulation is required for effectively using such model.

In summary, development is required of an efficient CoTDS co-simulation algorithm that can be utilized for dynamic studies in the presence of DGs. It should also be capable of being employed as a suitable platform for driving the aggregated modeling of loads. The CoTDS co-simulation method itself may further be used for the aggregated dynamic studies, thereby making it an even more compelling need for this development.

1.3   Project Objectives

The overall objective of this work is to develop a co-simulation methodology to bridge the wide gap between full EMTP methods and conventional balanced phasor methods for dynamic studies of Combined Transmission and Distribution Systems (CoTDS). The following items are addressed in this thesis:

1. Develop a numerical co-simulation method to integrate a phasor domain transmission system dynamic simulation software with a 3-phase distribution system software.

2. Develop a detailed phasor-domain DG inverter model that can be used efficiently in the CoTDS co-simulation for conducting dynamic studies.

3. Using the developed CoTDS simulation methodology, determine the key parameters of the aggregated WECC CLM for a given distribution system load.

4. Use the CoTDS co-simulation for model reduction which can further be used in μPMU based measurement, control and mitigation of undesirable events.

5. Study the impact of DG penetration levels on grid dynamics specifically the FIDVR phenomenon.

1.4 Report Organization

The rest of this report is organized as follows:

In Chapter 2, two methods for co-simulation of CoTDS are proposed for dynamic studies using parallel and series computation of the transmission system and distribution systems along with rigorous mathematical analysis on stability and convergence of the proposed numerical method. The proposed co-simulation method for CoTDS dynamic simulation is validated against full system simulation using PSAT and commercial EMTP software, Simscape PowerSystems.

In Chapter 3, a detailed DG inverter modeling operating in grid-connected mode is formulated in phasor domain to be used for CoTDS dynamic simulation. The developed phasor domain model is compared against conventional model and validated against full sine-wave model using Simscape PowerSystems software.

In Chapter 4, the benefit of the CoTDS co-simulation method using the detailed DG inverter model is demonstrated on distribution side voltage control methods.

In Chapter 5, CoTDS co-simulation is applied to dynamic load modeling of distribution system loads with the capability to represent the entire distribution system network and the loads. This is further used as a guiding tool to determine the aggregated WECC CLM parameter values.

In Chapter 6, A reduced distribution system model for developing control solutions based on μPMU measurements is proposed which is composed of sub-models that are analogous to the WECC CLM and aggregates the distribution system into load areas while ensuring the overall dynamics are retained.

In Chapter 7, impact on transmission system dynamics due to effect of the variation of DG penetration levels and single-phase air-condition motors in view of the IEEE standard 1547 VRT requirements is analyzed using the WECC CLM with the addition of DG model.

The report is concluded in Chapter 8, summarizing the contributions and future work.

CHAPTER 2. DYNAMIC CO-SIMULATION MODELING OF COMBINED TRANSMISSION-DISTRIBUTION SYSTEM

2.1 Mathematical Background

Simulation of a system that consists of well described sub-systems by using appropriate solvers for each sub-system is desired. To couple two or more sub-system solvers in time domain, co-simulation methods are used. In co-simulation the sub-systems are solved separately and the immediate mutual influence of subsystems is replaced by exchanging data at fixed time points [25]. In this section, the co-simulation concept is discussed for series and parallel computation of sub-systems and a convergence analysis of these methods is presented.

2.1.1 Preliminaries

Let us first consider a standard ordinary differential equation (ode) in state variable x given by

$$\dot{x} = f(t, x) \tag{2.1}$$

Convergence of numerical integration methods of such an ode are generally analyzed using the following definitions [26].

Definition 1- Consistency: A numerical method is called *consistent* if the local trunca-tion error, τ_i at the ith time step given by equation (2.2), approaches 0 as the time step, $H \to 0$.

$$\tau(t_i, x_i, H) = \frac{x(t_{i+1}) - x(t_i)}{H} - \phi(t_i, x(t_i), H) \tag{2.2}$$

where, ϕ is the increment function of the numerical solution by a given method.

Definition 2- Stability: A numerical method is called *stable* for a given time step, H, if the numerical solution of equation of the form (2.3) produces a bounded solution [26].

$$\dot{x} = \Lambda x \tag{2.3}$$

Definition 3- Convergence: A numerical method is *convergent* if the numerical solution converges to the exact solution as time step, $H \to 0$ [26].

Dahlquist Equivalence Theorem: If a method is *consistent* and *stable*, it is convergent [26]. *Consistency + Stability $\Rightarrow$ Convergence*

2.1.2 Test System Definition

In order to study the numerical stability and the convergence behavior of co-simulation methods a test model of a coupled system has to be defined. In general, the co-simulation methods are applied on non-linear systems. For the purpose of stability and convergence analysis of numerical time integration methods, a linear test model is used according to the Dahlquists stability theory [27]. It follows from Dahlquist Equivalence Theorem (Sec. 2.1.1) that if a method is consistent and stable, it is convergent.

Since coupling requires a minimum of two sub-systems, we first define a total system of linear *ode* consisting of two state variables, X_A and X_B.

$$\begin{aligned} \dot{X_A} &= \lambda_A X_A - K_A X_B \\ \dot{X_B} &= \lambda_B X_B + K_B X_A \end{aligned} \tag{2.4}$$

where, $\lambda_A < 0, \lambda_B < 0, K_A > 0$ and $K_B > 0$.

The additional constraints on the co-efficients in equation (2.4) is to ensure that the true solution of the system is stable. Examination of the eigen values of this system indicates that this system will always be stable and a true solution with initial values of X_{A0}, X_{B0} is given by Examination of the eigen values of this system indicates that this system will always be stable with a true solution with initial value of X_{A0} and X_{B0} is given by

$$
\begin{bmatrix} X_A \\ X_B \end{bmatrix} = e^{\begin{bmatrix} \lambda_A & -K_A \\ K_B & \lambda_B \end{bmatrix} . t} . \begin{bmatrix} X_{A0} \\ X_{B0} \end{bmatrix}
\tag{2.5}
$$

Now, let us write this same test system in a coupled system format using Differential Algebraic Equations (DAE) with inputs U_A and U_B coming from outputs Y_B and Y_A respectively. The DAE for the A sub-system is given by

$$
\dot{X_A} = \lambda_A X_A + U_A
$$
$$
Y_A = K_B X_A
\tag{2.6}
$$

and the DAE for the B sub-system is given by

$$
\dot{X_B} = \lambda_B X_B + U_B
$$
$$
Y_B = -K_A X_B
\tag{2.7}
$$

where $U_A = Y_B$ and $U_B = Y_A$.

2.1.3 Co-Simulation Algorithms

The algorithms of the two methods of co-simulation of coupled systems is now discussed in further detail. In both these methods, the key idea is to solve the sub-systems independently and at every integration time step, the input to each of the subsystems is updated from the corresponding output of the other subsystem (Fig. 2.1). The input to the sub-systems during an integration time step is assumed to be constant.

2.1.3.1   Method 1: Parallel Computation

1. The initial values of the state variables, $X_{A,i}$, $Y_{A,i}$, $X_{B,i}$, $Y_{B,i}$ are known at $i = 0$ from the steady state solution. Set the time index $i = 0$ and the start time, $t_i = 0$.

2. Set the input $U_{A,i} = Y_{B,i}$ for the A sub-system.

3. Solve the DAEs for the A sub-system.

4. Set the input $U_{B,i} = Y_{A,i}$ for the B sub-system.

5. Solve the DAEs for the B sub-system.

6. Increment the time index, i, go back to step 2 proceed to the next simulation time step until final time is reached.

Since A and B sub-systems use independent solvers, the algorithm lends itself to parallel computation.

2.1.3.2   Method 2: Series Computation

1. Set the time index $i = 0$ and the start time, $t_i = 0$. The initial values of the state variables, $X_{A,i}$, $Y_{A,i}$, $X_{B,i}$, $Y_{B,i}$ are known at $i = 0$ from the steady state solution.

2. Set the input $U_{A,i} = Y_{B,i}$ for the A sub-system.

3. Solve the DAEs for the A sub-system.

4. Set the input $U_{B,i} = Y_{A,i+1}$ for the B sub-system.

5. Solve the DAEs for the B sub-system.

6. Increment the time index, i, go back to step 2 proceed to the next simulation time step until final time is reached.

Here, in this method, although A and B sub-systems are computed in series, it is still possible to perform parallel computation when multiple B sub-systems exist.

2.1.4   Formulation of Difference Equations

The difference equations with an integration time-step, H is now formulated for the total system solution and the proposed co-simulation methods. In numerical integration, the choice of H is a trade-off between faster simulation times and avoiding numerical convergence problems.

2.1.4.1   Total System Simulation

The implicit trapezoidal integration method is a very widely used A-stable solver and so this is used to solve the total system to form a baseline for comparison of the coupled numerical methods. The difference equations for the system of equations shown in equation (2.4) is given by

$$
\begin{aligned}
X_{A,i+1} &= X_{A,i} + H[0.5(\lambda_A X_{A,i} - K_A X_{B,i}) + 0.5(\lambda_A X_{A,i+1} - K_A X_{B,i+1})] \\
X_{B,i+1} &= X_{B,i} + H[0.5(\lambda_B X_{B,i} + K_B X_{A,i}) + 0.5(\lambda_A X_{A,i+1} + K_B X_{A,i+1})]
\end{aligned}
\tag{2.8}
$$

With $\overline{X} = [X_A\ X_B]'$, this can now be written of the form

$$
\overline{X}_{i+1} = \overline{X}_i + H.\phi_T(\overline{X}_i, H)
\tag{2.9}
$$

where $\phi_T(\overline{X}_i, H)$ is the increment function for the total system using the implicit trapezoidal integration method.

2.1.4.2   Co-Simulation

In the co-simulation, the A sub-system and the B sub-system are different solvers and so could use the same or different numerical methods. The purpose of the analysis is to study the effect of the coupling method considering that the individual solvers are convergent while running independently. Therefore, for the purpose of this study, the implicit trapezoidal method is retained for the A sub-system and an explicit Euler method is used for the B sub-system with a smaller step-size, $h = H/n$, n being the number of small steps.

Method 1 (Parallel Computation)

In the parallel computation co-simulation method, from Equations (2.5-2.7), $U_{A,i} = -K_A X_{B,i}$ and $U_{B,i} = K_B X_{A,i}$. So, we can write the difference equations as

$$X_{A,i+1} = X_{A,i} + H[0.5(\lambda_A X_{A,i} - K_A X_{B,i}) + 0.5(\lambda_A X_{A,i+1} - K_A X_{B,i})]$$
$$X_{B,i+1} = X_{B,i}(1 + h\lambda_B)^n + [(\frac{K_B}{\lambda_B})(1 + h\lambda_B)^n - 1]X_{A,i} \tag{2.10}$$

This can be expressed of the form

$$\overline{X}_{i+1} = \overline{X}_i + H.\phi_{C1}(\overline{X}_i, H) \tag{2.11}$$

where $\phi_{C1}(\overline{X}_i, H)$ is the increment function for co-simulation method using parallel computation.

Method 2 (Series Computation)

In the series computation co-simulation method, as the A sub-system is solved first, $U_{B,i} = K_B X_{A,i+1}$. $U_{A,i}$, however, remains the same as that of Method 1. The difference equations is therefore written as

$$X_{A,i+1} = X_{A,i} + H[0.5(\lambda_A X_{A,i} - K_A X_{B,i}) + 0.5(\lambda_A X_{A,i+1} - K_A X_{B,i})]$$
$$X_{B,i+1} = X_{B,i}(1 + h\lambda_B)^n + [(\frac{K_B}{\lambda_B})(1 + h\lambda_B)^n - 1]X_{A,i+1} \tag{2.12}$$

This can be expressed of the form

$$\overline{X}_{i+1} = \overline{X}_i + H.\phi_{C2}(X_i, H) \tag{2.13}$$

where $\phi_{C2}(X_i, H)$ is the increment function for co-simulation method using series computation.

2.1.5 Convergence Analysis

As stated earlier in section 2.1.1, for a numerical integration method to be convergent, we need to demonstrate consistency and stability. Then, by Dahlquist Equivalence Theorem, the method is convergent. In this section we use the difference equations formulated in the previous section and analyze this criteria to establish the convergence of the co-simulation methods and compare the results with the baseline trapezoidal integration method for the total system.

2.1.5.1 Consistency

For consistency, we are particularly interested in showing that the local truncation error, τ_i, diminishes towards zero as the steps size, H approaches zero. The calculation of truncation from equation (2.2), requires the true analytic solution and the numerical increment function. The analytical solution is given in equation (2.5) and the increment functions of each method are obtained from the difference equations as described in (2.9-2.13). From these, it can be shown that as $H \to 0$, $\tau_i \to 0$ for the co-simulation methods.

It can also be confirmed graphically by plotting τ_i for the first time step as $H \to 0$ for two examples of system parameters (λ_A, λ_B, K_A and K_B). For the base case of implicit trapezoidal integration of the total system the error decay is as expected since this method is known to be consistent. It is also clear that both the co-simulation methods are consistent as well.

2.1.5.2 Stability

For first order linear systems, the stability of the numerical method can be determined when the absolute value of $\mid m \mid < 1$ when the x_{i+1} is expressed in terms of x_i as equation 2.14.

$$x_{i+1} = m.x_i \tag{2.14}$$

However, for higher order systems, m becomes a matrix, M and so we consider the eigen values of this matrix. If the eigen values are within the unit circle, then the numerical method is stable for the system. The stability of the test system can be therefore be analyzed by re-writing the difference equations in Section 2.1.4 as

$$\overline{X}_{i+1} = M.\overline{X}_i \tag{2.15}$$

and examining the eigen values of M. For the base case, implicit trapezoidal method, $M =$

$$\begin{bmatrix} 1 - 0.5\lambda_A H & 0.5K_A H \\ -0.5K_B H & 1 - 0.5\lambda_B H \end{bmatrix}^{-1} \begin{bmatrix} 1 + 0.5\lambda_A H & -0.5K_A H \\ 0.5K_B H & 1 + 0.5\lambda_B H \end{bmatrix} \tag{2.16}$$

For the co-simulation Method 1, $M =$

$$\begin{bmatrix} 1 - 0.5\lambda_A H & 0 \\ 0 & 1 \end{bmatrix}^{-1} \begin{bmatrix} 1 + 0.5\lambda_A H & -0.5K_A H \\ (\frac{K_B}{\lambda_B})\{(1 + h\lambda_B)^n - 1\} & (1 + h\lambda_B)^n \end{bmatrix} \tag{2.17}$$

For the co-simulation Method 2, $M =$

$$\begin{bmatrix} 1 - 0.5\lambda_A H & 0 \\ -(\frac{K_B}{\lambda_B})\{(1 + h\lambda_B)^n - 1\} & 1 \end{bmatrix}^{-1} \begin{bmatrix} 1 + 0.5\lambda_A H & -0.5K_A H \\ 0 & (1 + h\lambda_B)^n \end{bmatrix} \tag{2.18}$$

The eigen values of M are not only dependent on the system parameters (λ_A, λ_B, K_A and K_B), but also on the step size, H and h. The base case implicit trapezoidal method is A-stable and so we can expect that the maximum magnitude of the calculated eigen values will be less than 1. However, for the two co-simulation methods, the stability is ascertained for various parameter values and the absolute maximum magnitude of the eigen values for the transformation matrix, M is plotted against H. Fig. 2.3 shows these eigen values for the three simulation methods for the two examples considered.

2.1.5.3 Convergence

By Dahlquist Equivalence Theorem (Sec 2.1.1) convergence follows from consistency and stability. Therefore, the co-simulation methods are convergent as long as the H is chosen to be small enough for the eigen values of the system matrix M to be within the unit

circle. This will be further demonstrated by applying the numerical method to compute the discrete evolution of the system state variables in time domain.

Fig. 2.4(a) shows the results for the first example with λ_A = -1, λ_B = -10, K_A =2 and K_B =2. When we set the step size, $H = 0.1$, it can be clearly inferred from the plot that both the the total system solution and the co-simulation methods match very closely with the true solution. However, when the step size is increased to $H = 1$, the solution takes a longer time to converge. This is evident from the eigen value plots in Fig. 2.3.

Now, let us consider the second example (λ_A = -1, λ_B = -2, K_A =2 and K_B =2) where the maximum eigen value magnitude crosses the unity limit in the co-simulation methods. We first set the time step, H to 0.1 and then to 0.75. The corresponding discrete time domain evolution plots are shown in Fig.2.5. For H=0.1, the results are of the all the simulation results are convergent and follow the true solution. However, with H increased to 0.75, the eigen value of the M for the co-simulation method 1 is almost unity whereas that of method 2 is significantly lower than unity. This would suggest that at this time step, the method 1 is getting dangerously close to instability and hence non-convergent. This is validated in Fig.2.5, where the method 1 shows wild oscillations whereas the method 2 is highly stable and convergent towards the true solution. The total system solution, as expected, is stable and convergent in both the cases.

Therefore, from this analysis we can observe that co-simulation methods are stable and convergent as long as we keep the step size small enough so that the maximum eigen value magnitude of the transformation matrix is lower than 1. This limitation is due to the methodology of the co-simulation even though the original system when simulated as a single total system of equations is numerically stable and converges to the true analytical solution. The coupling terms and the eigen values of the original system influence the convergence of the coupled systems. The analysis also indicates that series computation of the coupled systems has better stability characteristics compared to parallel computation.
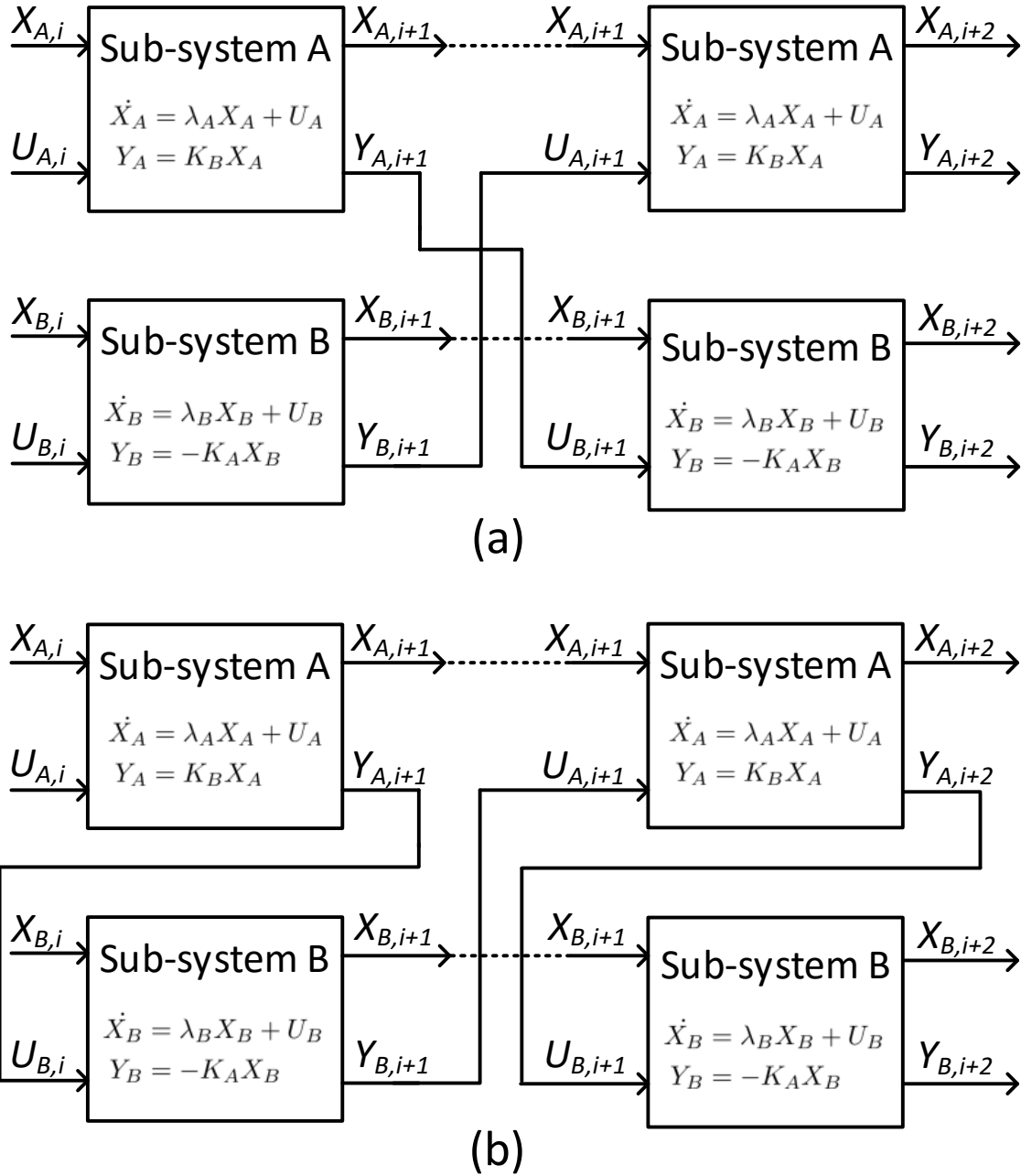
Figure 2.1 Co-Simulation block diagrams. (a) Parallel Computation. (b) Series Computation
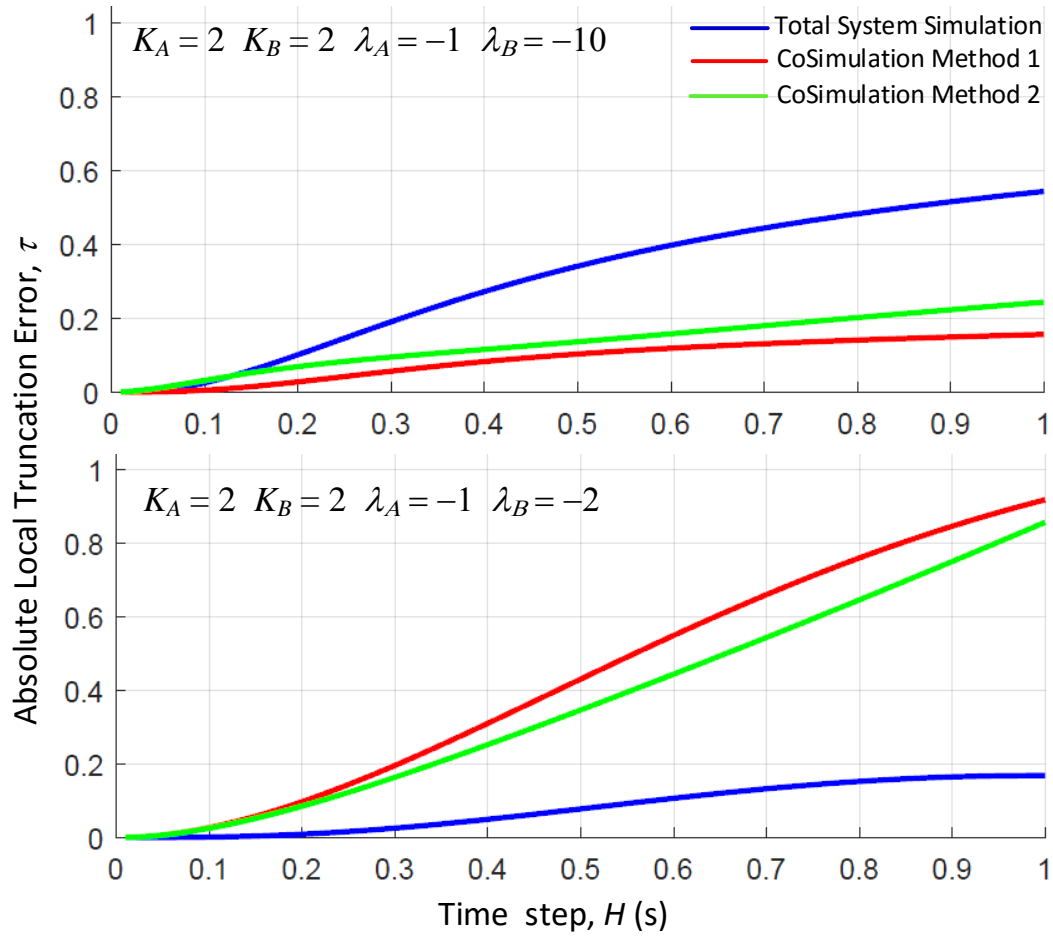
Figure 2.2   Comparison of Local Truncation Error at the first time step for Co-simulation methods and Total system simulation.
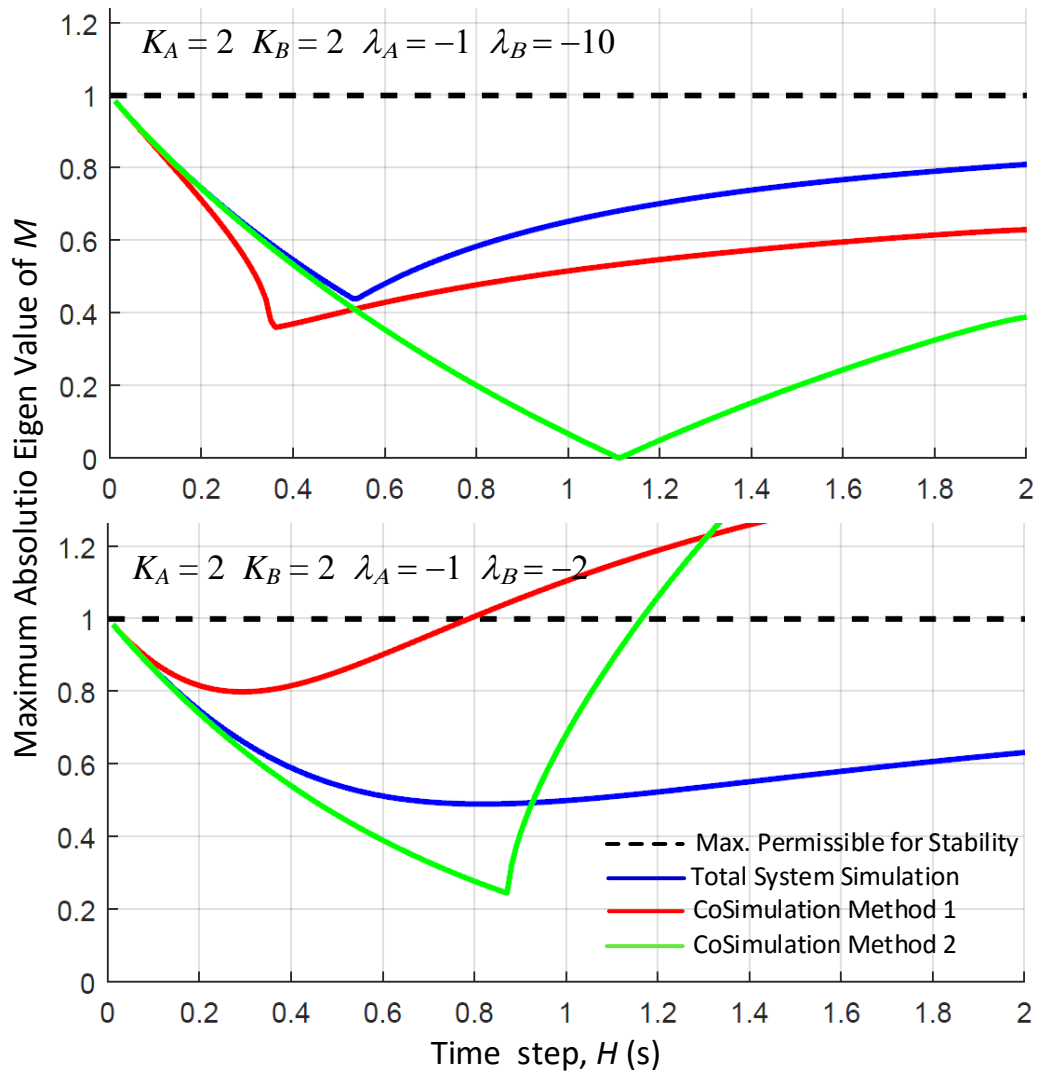
Figure 2.3   Maximum absolute eigen value of transformation matrix, M. for co-simulation
methods and Total system simulation relative to the absolute limit.
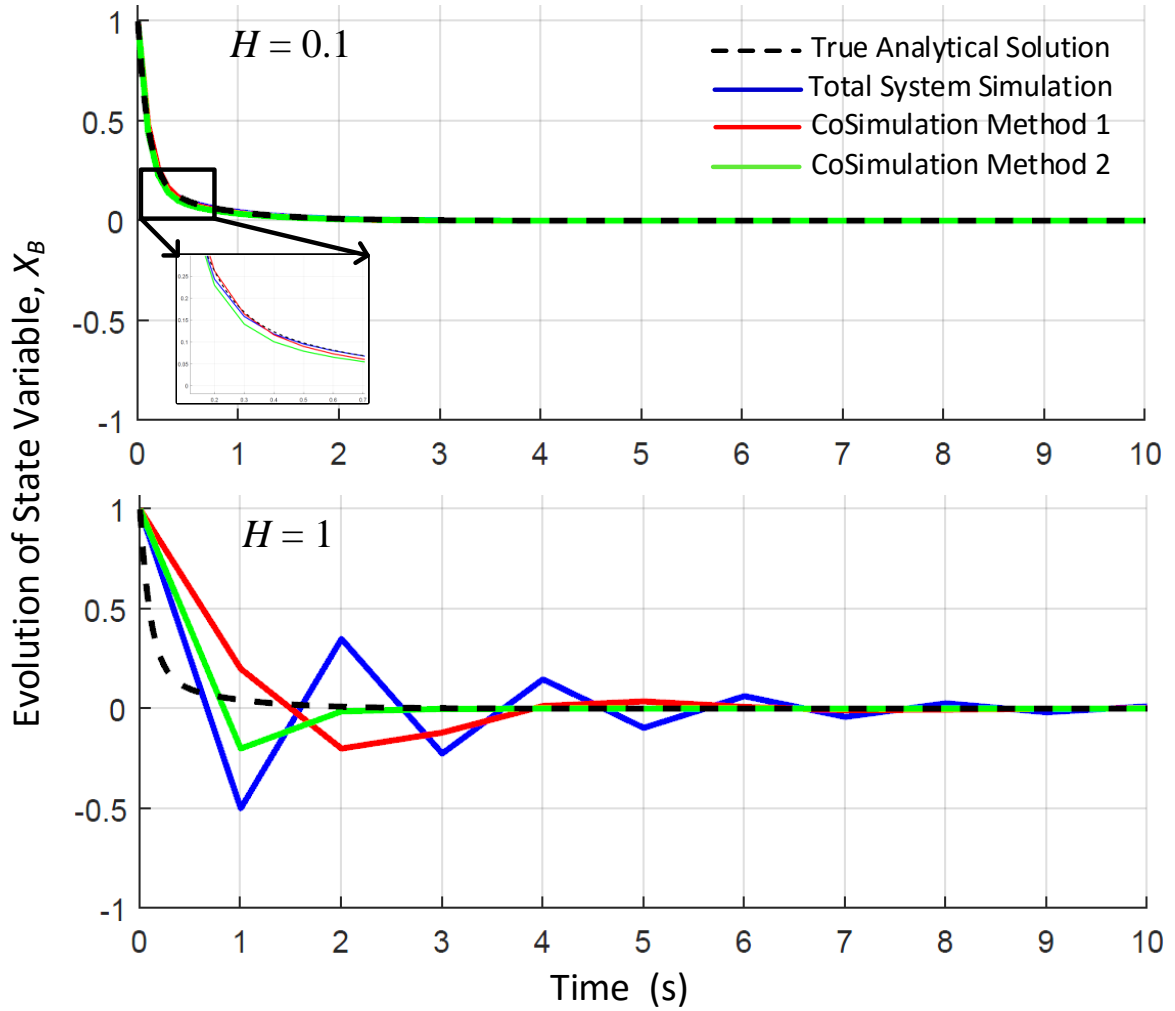
Figure 2.4   Discrete evolution of the system using co-imulation and total system simulation compared with the true solution for (λ_A = -1, λ_B = -10, K_A =2 and K_B =2).

Figure 2.5   Discrete evolution of the system using co-simulation and total system simulation compared with the true solution for ($\lambda_A = $ -1, $\lambda_B = $ -2, $K_A =$2 and $K_B =$2).

2.2 Combined Transmission-Distribution System (CoTDS) Dynamic Co-simulation

The two methods of co-simulation are now utilized in the dynamic study of transmission and distribution systems connected to each other at the interfacing system bus. A straight-forward way of implementing the CoTDS simulation using either of the co-simulation methods is to represent the transmission system as the A sub-system and the distribution system as the B sub-system with the transmission system bus where the distribution feeder originates as the point of coupling. At this point, the load power of the transmission system is its input and the bus voltage its output. In contrast, the source voltage of the distribution system becomes its input and correspondingly the source power becomes the output. The co-simulation of the CoTDS as shown in Fig. 2.6 is further elaborated in this section.
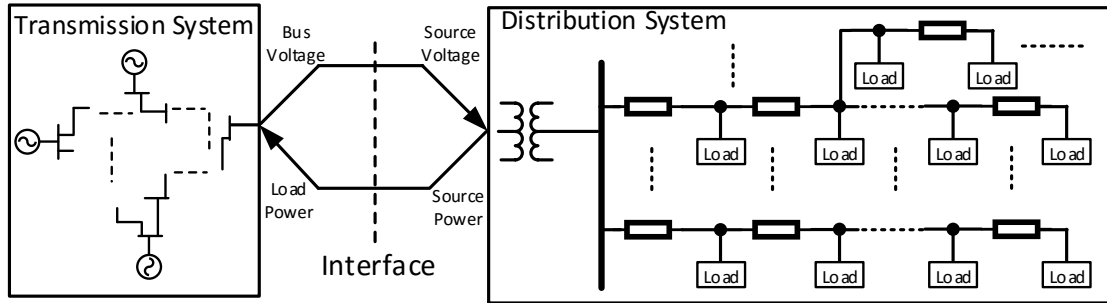
Figure 2.6   Combined Transmission-Distribution System setup

2.2.1   Assumptions and Scope

For the purpose of the study in this paper, it is assumed that the distribution system load at the sub-station end is balanced. Unbalance in distribution system load is handled through node-level dynamic components and three-phase power flow which will be discussed in the subsequent sections. The objective of this study is to demonstrate the co-simulation methods to utilize existing distribution system power flow software in CoTDS co-simulation. This methodology can be further developed to handle unbalanced systems.

2.2.2 Transmission System Dynamic Modeling

The transmission system dynamic model is comprehensively studied in literature and is well documented in [28]. The power system is mathematically represented by a system of differential and algebraic equations (DAEs). The DAEs in the transmission system dynamic model consist of dynamic components such as generators, exciters, governors and the network. While the network is represented only by algebraic equations, the other components comprise of both differential and algebraic equations. Together they form the DAE for the transmission system. The model is given by the following equation (2.19) with x_T and y_T as the set of transmission system differential and algebraic state variables respectively. x_T contains variables related to generator dynamics including the exciter and governor control. And y_T contains the transmission network variables of bus voltages, generator powers and the exciter and governor references. u_T is the set of inputs which is the load power at the load buses where the load is represented by the source power of the distribution system. The corresponding bus voltages at these load buses are the inputs to the distribution system of equations.

$$\dot{x_T} = f_T(x_T, y_T, u_T)$$
$$0 = g_T(x_T, y_T, u_T)$$
(2.19)

2.2.3 Distribution System Dynamic Modeling

The distribution system has loads comprising of various load components such as static loads (ZIP loads), induction motor loads and reactive shunt compensators in each of the nodes. The nodes can also include distribution generator (DG) inverters feeding power into the distribution network supporting a fraction of the total distribution system load. In this paper, we are not considering the DG inverter model as it is outside the scope of the paper and will be considered in a future publication.

The overall structure of the distribution system is also modeled using the DAE formulation. The comprehensive non-linear model are given in the following equation.

$$\dot{X}_D = f_D(X_D, Y_D, U_D)$$

$$0 = g_D(X_D, Y_D, U_D)$$

(2.20)

Here, X_D and Y_D are the distribution system differential and algebraic state variables respectively. U_D is the input to the distribution system which is the source voltage at the sub-station entrance of the distribution system. This is the same as the corresponding load bus voltage of the transmission system.
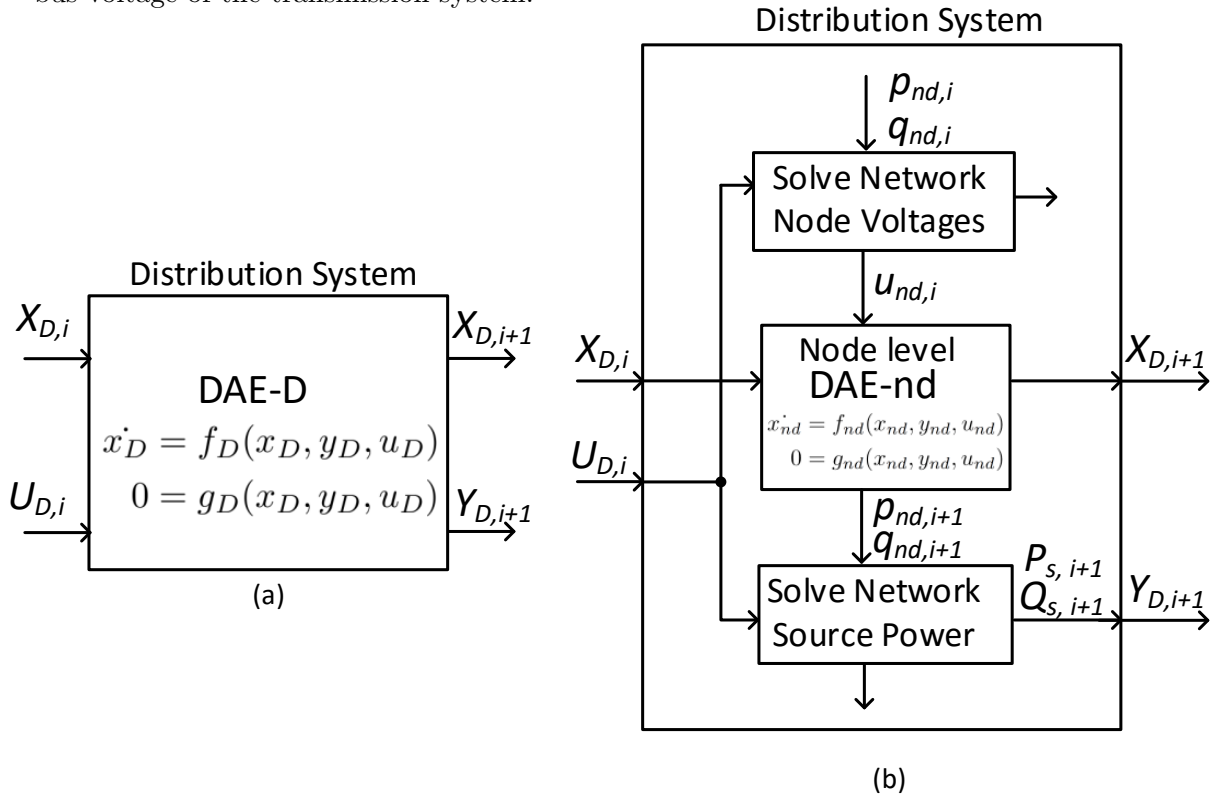
Figure 2.7   Distribution System Dynamic Model (a) Complete set of DAE   (b) Implementation using node-level dynamic component DAE and distribution system power flow solver.

In this work, the distribution system set of DAEs is solved at a node level instead of solving the complete set of DAEs of an entire distribution system together. The advantages

with this approach are: 1. A dynamic component DAE model can be handled individually using the node voltage as its input and interfaced with the network. 2. Dynamic models at various nodes having different time scales can be handled independently. 3. Existing power flow solvers for the distribution system can be directly used to solve for the network node voltages and source power. Equation (2.20) is now written at a node level for each dynamic component as

$$\dot{x_{nd}} = f_{nd}(x_{nd}, y_{nd}, u_{nd})$$
$$0 = g_{nd}(x_{nd}, y_{nd}, u_{nd})$$

(2.21)

The distribution system is solved in the following steps.

1. Using the $U_{D,i}$, the power flow is performed on the distribution network to obtain the node voltages, $u_{nd,i}$.

2. The node voltages, $u_{nd,i}$ are passed to the node-level DAE block where the DAE of the dynamic component at each node is solved.

3. The power at each node ($p_{nd,i}$ and $q_{nd,i}$) are updated and power flow is repeated on the distribution network to obtain the total source power, $Y_{D,i+1}$.

The distribution system has loads comprising of various load components such as static loads (ZIP loads), induction motor loads and reactive shunt compensators. The nodes can also include distribution generator (DG) inverters feeding power into the distribution network supporting a fraction of the total distribution system load. In this chapter, we are not considering the DG inverter model and will be considered later in the thesis. In this chapter, the static loads and the induction motor loads are considered.

2.2.3.1 Static Loads

The static loads, $P_{L,ST}, Q_{L,ST}$ are represented by constant impedance, constant current and constant power type loads conventionally referred to as the ZIP loads. These can be represented by the following algebraic equation (2.22).

$$
\begin{aligned}
P_{L,ST} &= \quad P_1.V_n^2 + P_2.V_n + P_3 \\
Q_{L,ST} &= \quad Q_1.V_n^2 + Q_2.V_n + Q_3
\end{aligned}
\tag{2.22}
$$

Here, V_n is the node voltage on the distribution network and P_1, P_2, P_3, Q_1, Q_2, Q_3 are constants determining the load.

2.2.3.2 Induction Motor Loads

The induction motor is a highly dynamic load, and therefore, it needs to be properly represented with differential and algebraic equations. There are several models of the induction motor in literature ranging from the first to fifth order. In this work, the dynamics of the loads is very critical as the purpose is to study the interaction of transmission system dynamics with the loads in the distribution system. Therefore, the comprehensive fifth order induction motor model as described in [29] is chosen and a summary of the differential equations are given in equation (2.23).

$$
\begin{aligned}
\frac{d\Psi_{ds}}{dt} &= \omega_b[V_{dn} - \frac{R_s.X_{rr}}{X_e^2}.\Psi_{ds} - \Psi_{qs} + \frac{R_s.X_M}{X_e^2}.\Psi_{dr}] \\
\frac{d\Psi_{qs}}{dt} &= \omega_b[V_{qn} - \frac{R_s.X_{rr}}{X_e^2}.\Psi_{qs} + \Psi_{ds} + \frac{R_s.X_M}{X_e^2}.\Psi_{qr}] \\
\frac{d\Psi_{dr}}{dt} &= \omega_b[-\frac{R_r.X_{ss}}{X_e^2}.\Psi_{dr} - (1 - \omega_r).\Psi_{qr} + \frac{R_r.X_M}{X_e^2}.\Psi_{ds}] \\
\frac{d\Psi_{qr}}{dt} &= \omega_b[-\frac{R_r.X_{ss}}{X_e^2}.\Psi_{qr} + (1 - \omega_r).\Psi_{dr} + \frac{R_r.X_M}{X_e^2}.\Psi_{qs}] \\
\frac{d\omega_r}{dt} &= \frac{1}{2H}[(\frac{X_M}{Xe^2}).(\Psi_{ds}.\Psi_{qr} - \Psi_{dr}.\Psi_{qs}) - T_L]
\end{aligned}
\tag{2.23}
$$

where, Ψ_{ds}- Ψ_{qs} and Ψ_{dr}- Ψ_{qr} are the d- and q- axis components of the stator and rotor flux linkages per second. V_{dn} and V_{qn} are the d- and q-axis components of the node voltage, V_n; and R_s, R_r, X_{ss}, X_{rr}, X_M and H are the induction motor parameters with

$X_e = \sqrt{X_{ss}.X_{rr} - X_M^2}$. ω_b and ω_r are the base synchronous speed and the rotor speed respectively. T_L is the load torque. The algebraic power equations for the real and reactive power, $P_{L,IM}$ and $Q_{L,IM}$ consumed by the induction motor at a given node in the distribution system are given in equation (2.24).

$$P_{L,IM} = \frac{V_{dn}}{X_e^2}.(X_{rr}.\Psi_{ds} - X_M.\Psi_{dr}) + \frac{V_{qn}}{X_e^2}.(X_{rr}.\Psi_{qs} - X_M.\Psi_{qr})$$
$$Q_{L,IM} = \frac{V_{dn}}{X_e^2}.(X_{rr}.\Psi_{qs} - X_M.\Psi_{qr}) - \frac{V_{qn}}{X_e^2}.(X_{rr}.\Psi_{ds} - X_M.\Psi_{dr})$$
$$(2.24)$$

2.2.4 CoTDS co-simulation algorithm

With the exchange input output variables of the two systems thus identified, the two sets of DAEs can be represented using the co-simulation methods detailed in the previous section. The co-simulation methods as applied to the CoTDS dynamic simulation is proposed in Fig. 2.8 and Fig. 2.9. The transmission system is denoted by Sub-system T and the distribution system is denoted by sub-system D corresponding to sub-systems A and B in the discussions of Sec. 2.1.

In the proposed method, the distribution system set of DAEs is solved at a node level instead of solving the complete set of DAEs of an entire distribution system together. The advantages with this approach are:

1. A dynamic component can be handled individually using the node voltage as its input and interfaced with the network.

2. Existing power flow solvers for the distribution system can be directly used to solve for the network node voltages and source power.
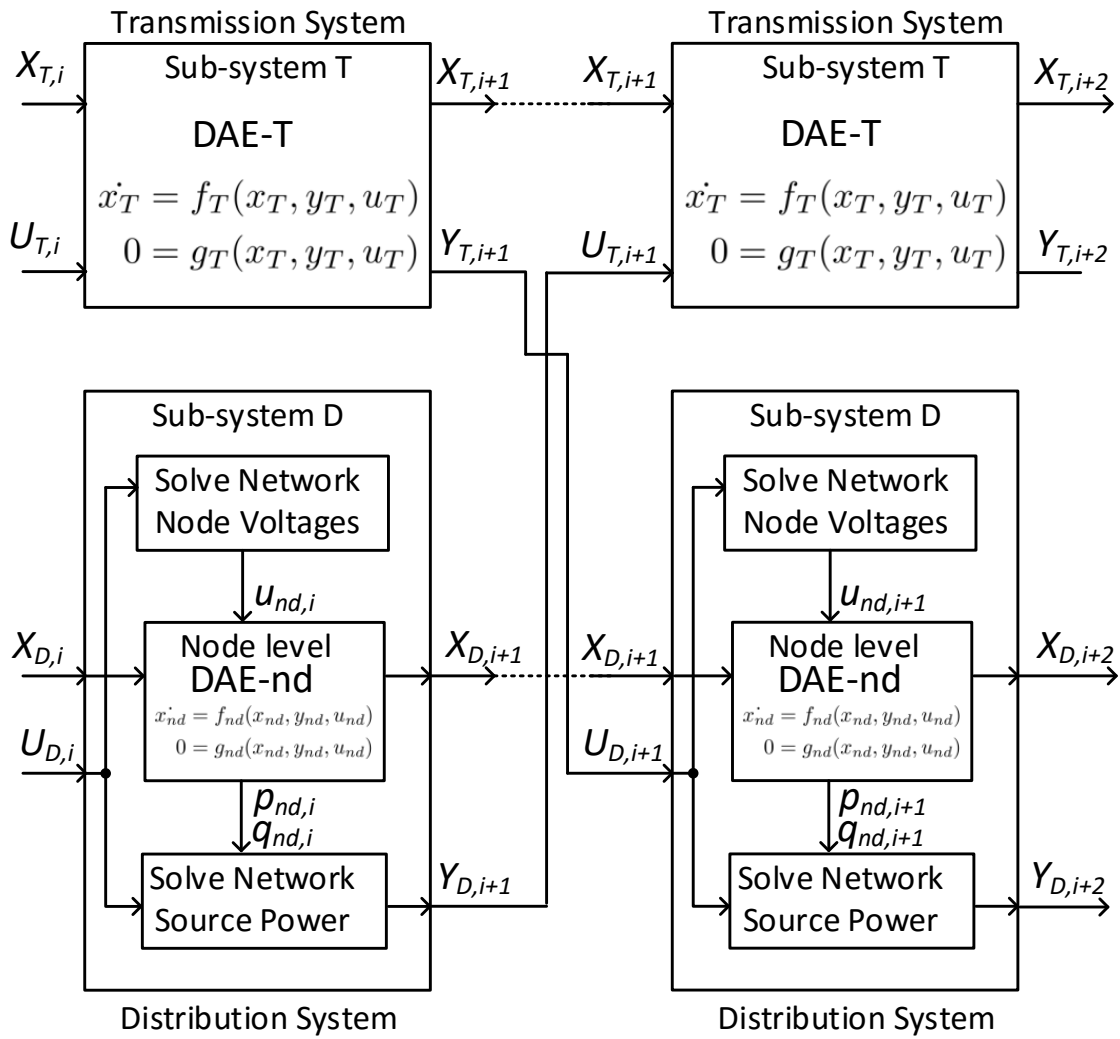
Figure 2.8   CoTDS simulation block diagram using Method 1: Parallel Computation
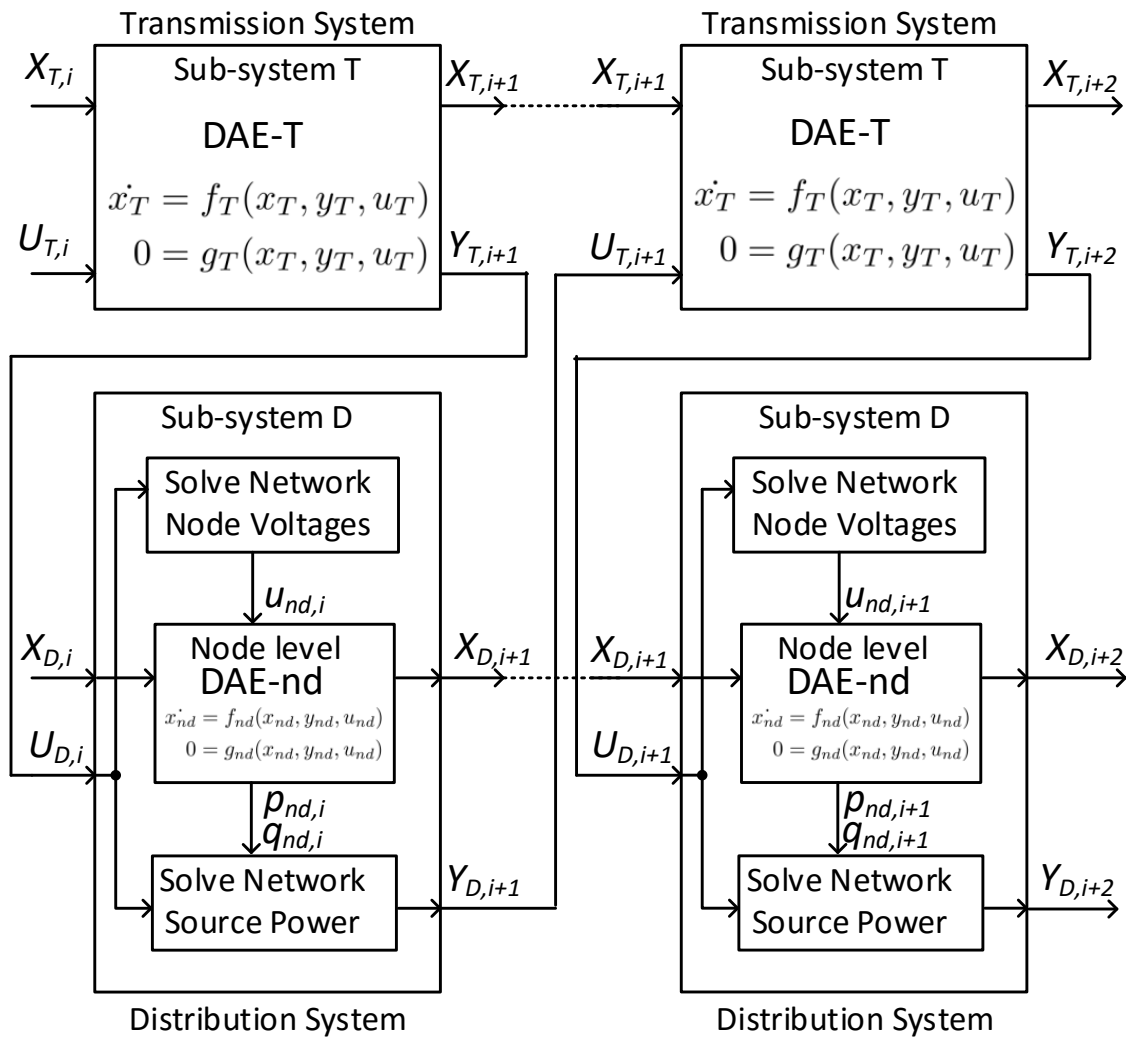
Figure 2.9   CoTDS simulation block diagram using Method 2: Series Computation

The mathematical background of the co-simulation is still applicable as there is no change in the overall scheme of exchanging variable information. Therefore the algorithm presented in Sec. 2.1.3 is employed to the CoTDS dynamic simulation as follows:

1. Solve transmission system power flow and distribution system power flow iteratively [3] to set initial values of all variables. The time index, i and the time t_i are initialized to 0.

2. Set the input $U_{T,i}$ from the source power, $Y_{D,i}$ of the distribution system.

3. Solve the DAE of the transmission system to obtain $X_{t,I+1}$ and $Y_{t,i+1}$.

4. For parallel computation, the $U_{D,i}$ is set by $Y_{T,i}$ and for series computation, $U_{D,i}$ is set by $Y_{T,i+1}$.

5. Solve the DAE for the distribution system using the method described in Section 2.2.3.

6. Increment i by 1, t_i by the simulation time step and go back to step 2 until final time is reached.

The significant difference of this proposed algorithm from [18] is the novel handling of the distribution system dynamics, the description and benefits of which are enumerated in Section 2.2.3. In addition, this algorithm accommodates both the parallel and series computation methods whereas the algorithm in [18] is a parallel computation method.

When there are multiple distribution systems, the step 5 of the co-simulation algorithm for all the distribution systems can be applied simultaneously for both the series and the parallel computation methods. Therefore, the benefit of parallel computing of multiple distribution systems can be realized even in case of series computation method of co-simulation.

From the algorithm, it can be noted that the for the transmission system simulation, we can use existing phasor domain software. For the distribution system, we can easily interface a power flow solver by handling the node level component dynamics through an

intermediary DAE solver and exchange the input output information through this interface. This is a significant benefit as most distribution system software easily handle power flow and can provide the necessary node voltages and the total source power. So by handling the dynamics of the node-level dynamic components using an intermediate software the combined dynamics of the entire system can very easily be studied without the need for changing the software of either of the simulators.

2.2.5 CoTDS co-simulation implementation

The implementation of the CoTDS co-simulation is demonstrated using PSAT [30] as the transmission system simulator and OpenDSS [31] as the distribution system power flow solver as shown in Fig. 2.10. The interface software is implemented in MATLAB. This approach does not require modification of the either PSAT or OpenDSS solvers and therefore this methodology can very easily be extended to other similar platforms.
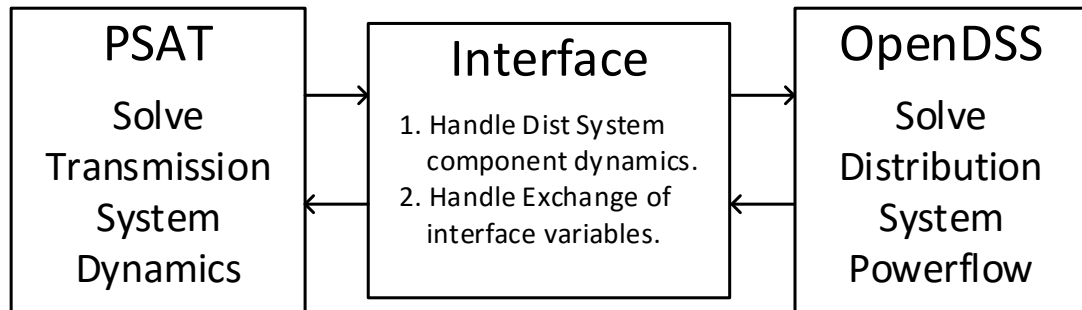
Figure 2.10   Implementation of CoTDS co-simulation

2.3   Validation of CoTDS Dynamic Co-simulation

In section, 2.1 it has been shown that the co-simulation of two coupled systems are numerically stable and convergent as long as the step size is kept small. If the step size is large, although the actual system is stable, the numerical results can be highly unstable. In this section, we validate this result on the CoTDS co-simulation against the total system simulated in a single dynamic solver. In addition further validation of the CoTDS co-simulation is performed against Simscape EMTP simulation to demonstrate the effectiveness of the proposed CoTDS co-simulation approach.

2.3.1   Validation of co-simulation against PSAT simulation for total system

In this section, a test case is setup to simulate a dynamic event first using PSAT which uses implicit trapezoidal integration to solve the total system dynamic equations and provide a reference behaviour for validating the co-simulation methods. The co-simulation is setup using methods 1 and 2 as described in the previous section. The node level component dynamics in the distribution systems are performed using *ode*45 which is an explicit method readily available in MATLAB.

The test system for studying the proposed co-simulation approach is shown in Fig. 2.11. A WECC 9-bus transmission system is interconnected with aggregated distribution systems at the load buses (5, 6 and 8). The distribution system loads are represented by a combination of static loads, induction motor loads and a lumped distribution feeder impedance

In this test case, since there are three load buses, we thereby have sub-system D1, D2 and D3 for the distribution system. In each of the sub-systems D1, D2 and D3, the loads are comprised of 70% static load and 30% induction motor loads. The static loads are further divided into constant impedance (Z), constant current (I) and constant power (P). The induction motor loads are split into two motors, IM1 (60% fraction) and IM2 (40% fraction).
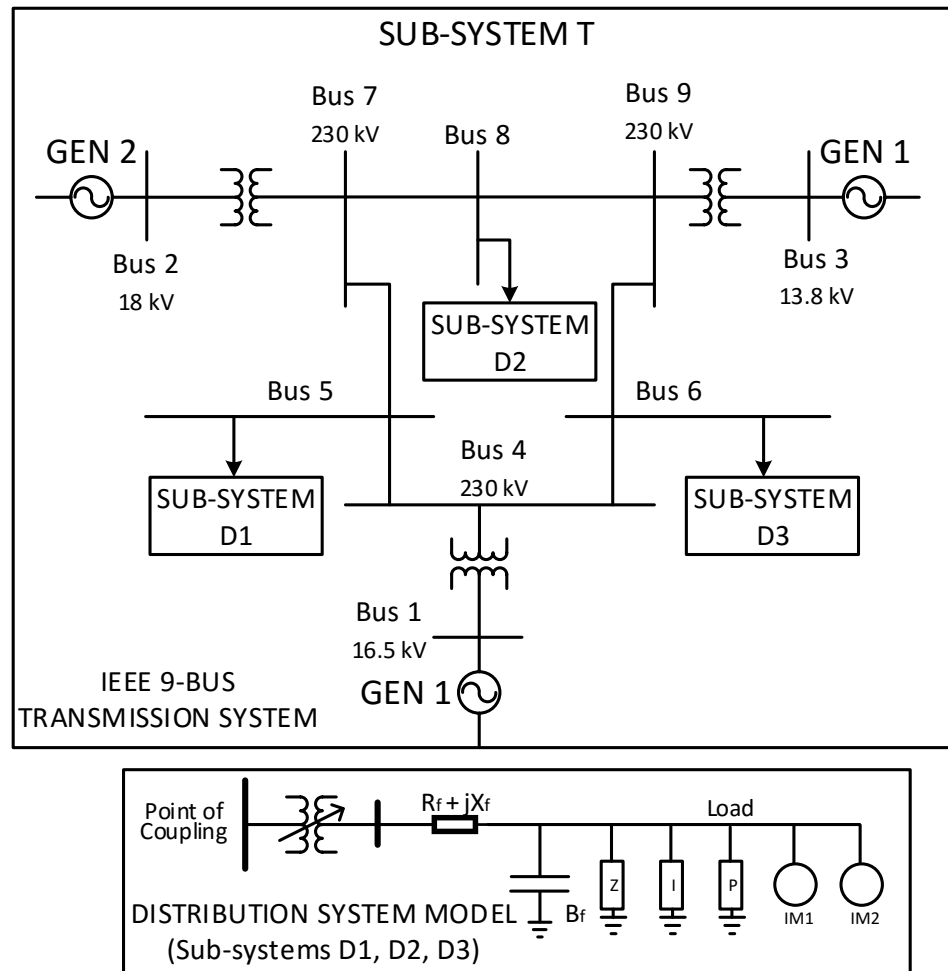
Figure 2.11   Test-case 1 for validation of the CoTDS co-simulation

In this test case, since there are three load buses, we thereby have sub-system D1, D2 and D3 for the distribution system. In each of the sub-systems D1, D2 and D3, the loads are comprised of 70% static load and 30% induction motor loads. The static loads are further divided into constant impedance (Z), constant current (I) and constant power (P). The induction motor loads are split into two motors, IM1 (60% fraction) and IM2 (40% fraction).

A dynamic event is created by initially setting the IM2 on Bus 6 as disconnected from the network and connecting it at $t = 11$s. The start up of the induction motor creates a transient dip in the bus voltage due to the motors drawing a large amount of reactive power. This event is analyzed using the proposed co-simulation methods and comparing it against total system simulation with PSAT.

Fig. 2.12(a) shows the simulation result with a small time step of $H = 0.006$s. This shows both co-simulation methods to give almost identical results and the voltage evolution matches the result obtained from simulating the entire system in PSAT. However, when a higher time step is used, $H = 0.037$s, Fig. 2.12(b) the co-simulation method 1 displays numerical stability issues. The co-simulation method 2 shows a stable and convergent result even at a higher time-step. This result corresponds to that obtained by rigorous mathematical analysis of the coupled system co-simulation methods in Sec. 2.1.

A summary of the impact of the integration time-step on the convergence of the simulation methods in this study is shown in Table 2.1.

Table 2.1   Impact of integration time-step, H on convergence.

Characteristic	Total System Simulation	CoSimulation Method 1	CoSimulation Method 2
Computation Algorithm	Full-DAE solved together	Parallel computation of T and D.	Series computation of T and D
Time-step, H for Stability	Large	Small	Large
Convergence at large H	Slow	Diverges	Fast
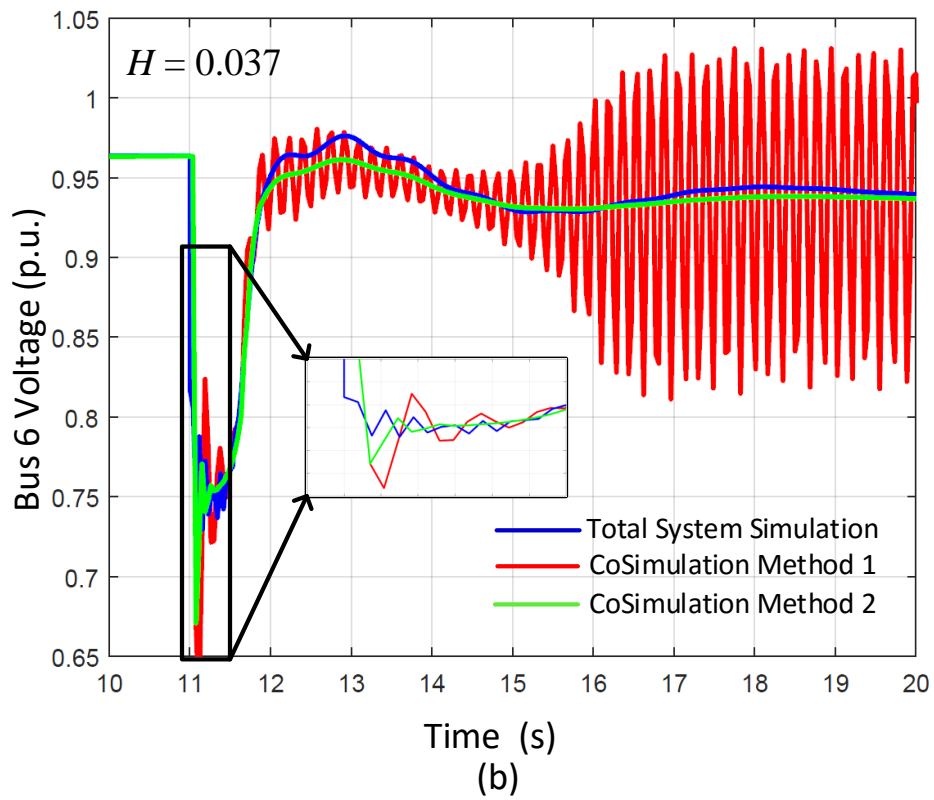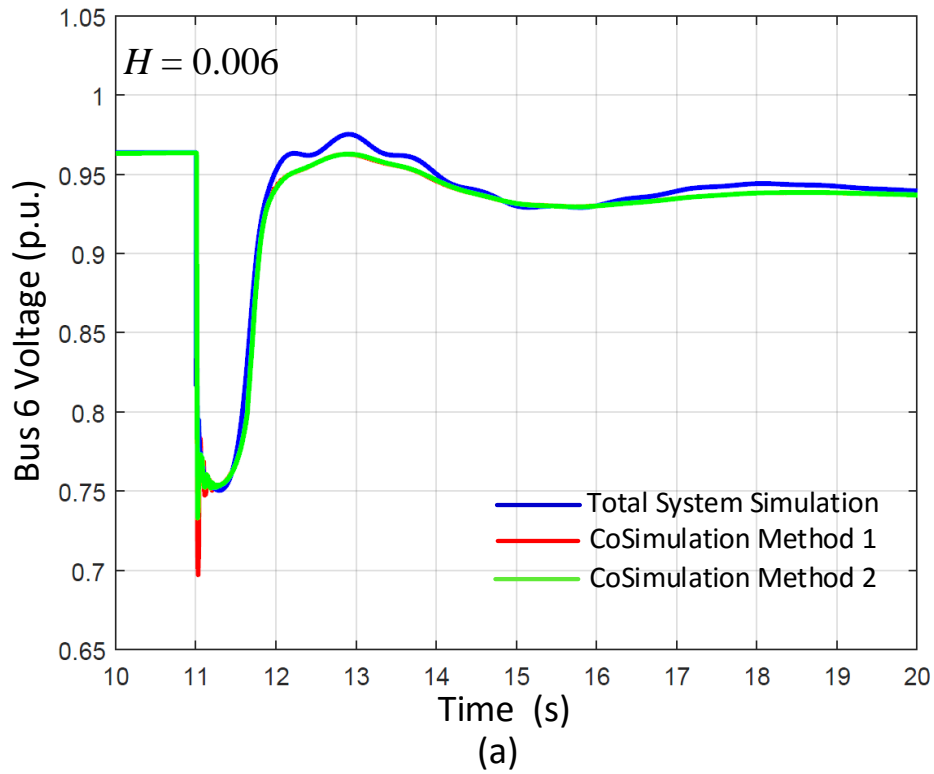
Figure 2.12   Bus Voltage evolution during induction motor startup with simulation time step, (a) $H = 0.006$s and (b) $H = 0.037$s.

2.3.2 Validation of co-simulation against Simscape EMTP simulation

In this section, the proposed CoTDS co-simulation using the method 2 is further validated against commercially available Simscape Power Systems software. The purpose of this validation is to prove the effectiveness of the co-simulation method by taking a three-phase distribution system and monitoring the behaviour of additional system details like active, reactive power dynamics which cannot be obtained using PSAT. Since Simscape is a complete EMTP three-phase sinusoidal simulation it provides an accurate performance reference for the validation.

The setup shown in Fig. 2.13 comprises of an equivalent generator in the transmission system including the automatic voltage regulating exciter dynamics, governor dynamics and the transmission line connecting to the load. The load is represented by a distribution system with two feeders each with 4 nodes. Each node contains a combination of 75% static and 25% induction motor loads. The nominal load at each node is evenly distributed amongst the nodes within the feeder. The synchronous generator and induction motor parameters are shown in Table 2.2.
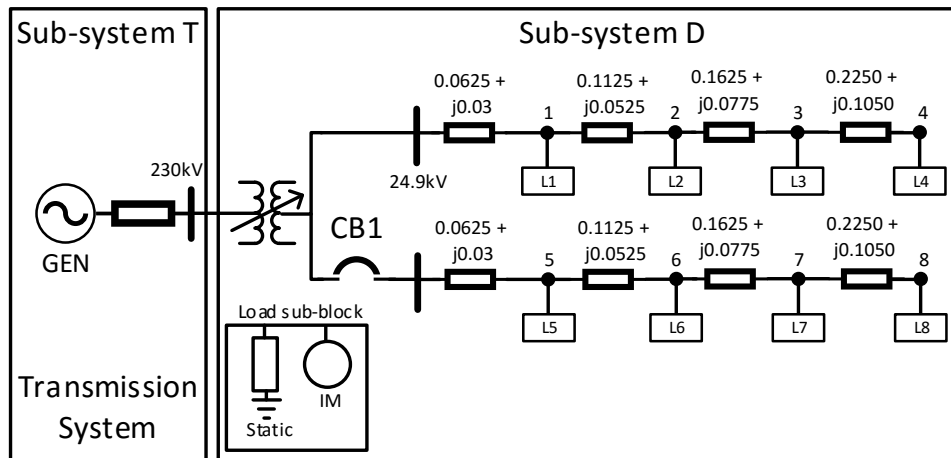
Figure 2.13 Test case 2 for validation of co-simulation against Simscape. All lines are 3-phase lines, but represented as single line.

Table 2.2   Generator and Induction Motor Parameters

Synchronous Generator (5th order)	p.u.
d-axis reactances x_d, x'_d, x''_d	0.14, 0.06, 0.06
q-axis reactances x_q, x'_q, x''_q	0.09, 0.09, 0.04
leakage reactance x_l	0.03
d-axis time constant t'_{do}	8.96 0.02
q-axis time constant t'_{qo}	0.31 0.02
Inertia Constant H_g	23.5 s
Induction Motor (5th order)	p.u.
Stator Resistance, r_s	0.03
Stator Reactance, x_s	0.06
Rotor Resistances, r'_{r1}, r'_{r2}	0.03, 0.20
Rotor Reactances, x'_{r1}, x'_{r2}	0.06, 0.15
Magnetizing Reactance, x_m	1.7
Motor Inertia, H_m	0.5s

The simulation is set up as follows: Initially one feeder representing 60% of the total load of 100MW, 33MVAR in the distribution system is connected to the load bus. The other feeder representing the remaining 40% of the load is connected at time $t = 1$s. The transient behaviour of the power up of the feeder is observed using EMTP method and the proposed co-simulation method 2.

Fig. 2.14 shows load bus voltage transient behavior during the connection of the feeder to the system. The EMTP simulation shows the complete transient in full detail with the actual instantaneous voltage plotted relative to the system base peak voltage. As the feeder is connected, the bus voltage at the interface bus dips and recovers due to the heavy reactive power demanded by the induction motor at start up. For both the methods, the active and the reactive power variation during the transient event is plotted in Fig. 2.15(a) and speed of the induction motor load is shown in Fig. 2.15(b).

The CoTDS simulation results using the proposed co-simulation method 2 displays excellent co-relation with the reference EMTP results. The voltage dip magnitude as well as the active and reactive power variation during the feeder connection shows similar behaviour.
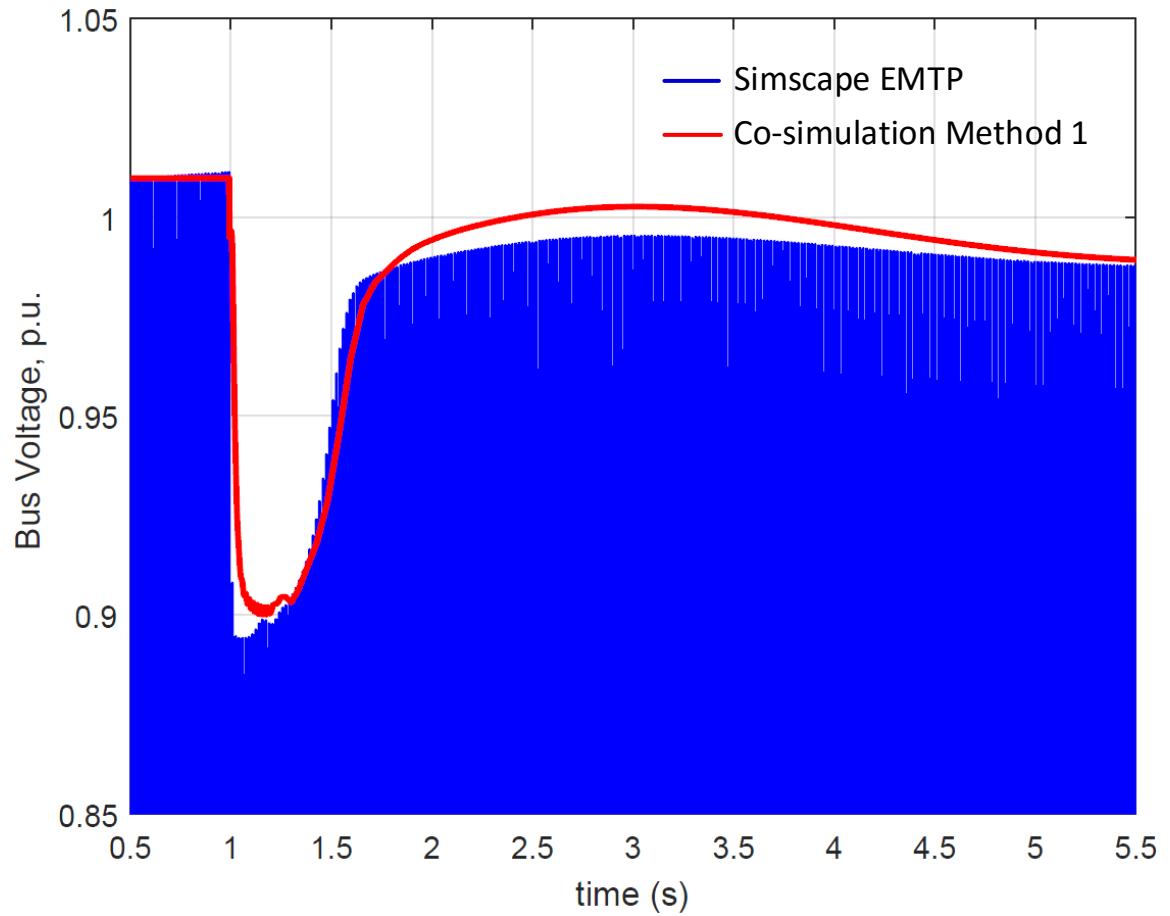
Figure 2.14   Interface Bus Voltage dynamic behaviour.
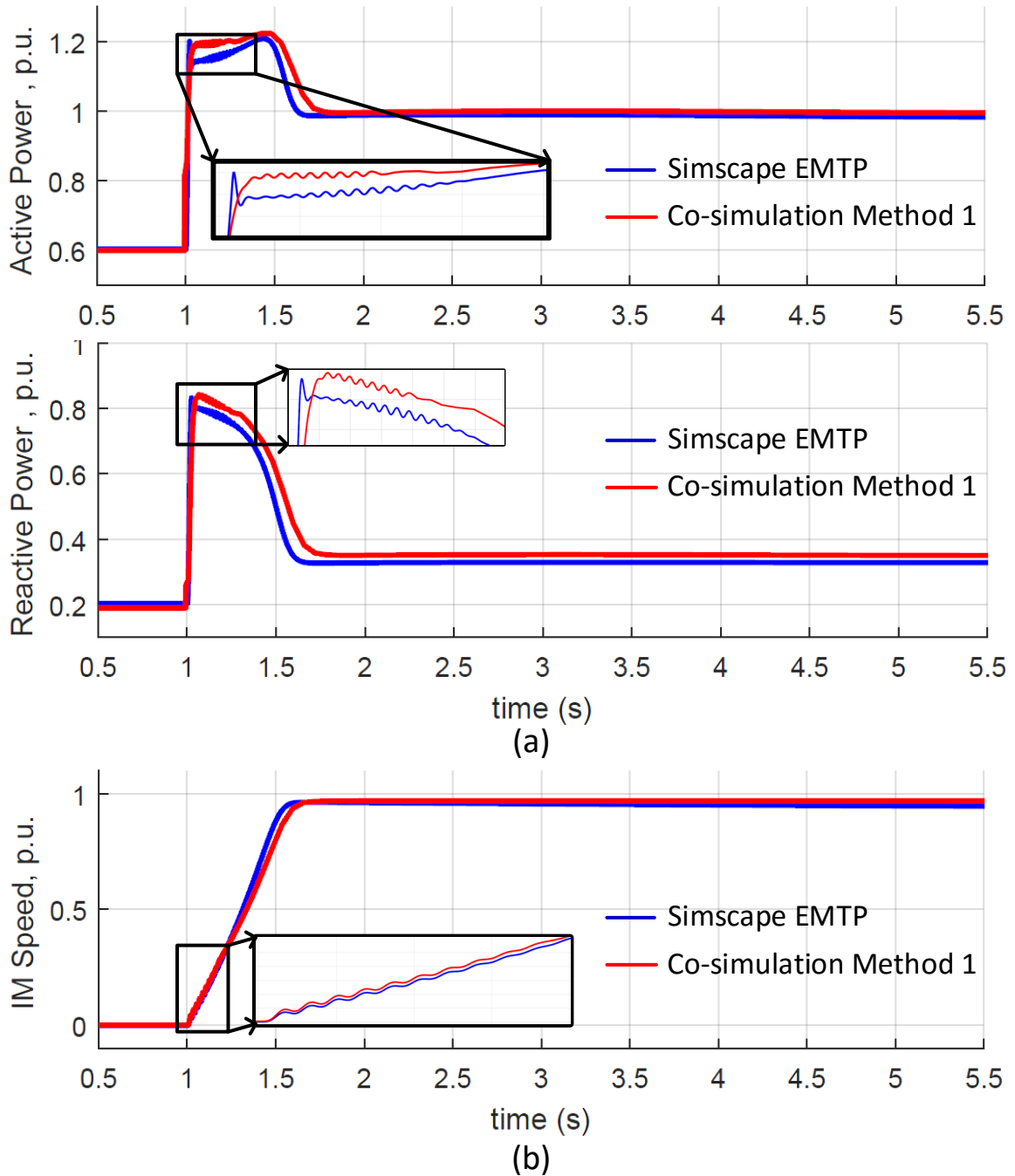
Figure 2.15 (a) Interface Bus Active and Reactive Power. (b) Induction Motor Speed at Node 1.

2.4 Conclusions

In this chapter, a rigorous mathematical analysis on convergence of numerical methods in co-simulation is presented. Both the series computation and parallel computation methods of co-simulation are shown to be stable and convergent for smaller integration step sizes and they closely match the true analytic solution. For larger step sizes, even if the individual sub-systems are convergent, the co-simulation may not be convergent. The actual step size for convergence has a dependency on the coupling and the system eigen values. The series computation method permits the use of a larger step size relative to that of parallel computation.

Two methods for co-simulation of CoTDS are proposed using parallel and series computation of the transmission system and distribution systems. The numerical performance of CoTDS co-simulation methods are validated against total system simulation in a single time-domain simulation environment revealing correspondence with the theoretical convergence analysis. Series computation method of transmission and distribution system dynamic models is shown to be numerically stable at larger time steps when the parallel computation method requires smaller time-steps to be stable. At larger time steps, the parallel computation method diverges whereas the series computation method converges. An important benefit of the series computation method is that it converges faster than the total system simulation method.

The parallel computation algorithm although requires smaller time step, it is favorable to parallel computing of transmission and distribution system. In the series computation algorithm, the computed bus voltages at the various interfacing buses can be used at the same time as the source voltage to the distribution systems and therefore renders itself for parallel computing of all the distribution systems. The series co-simulation of CoTDS is further validated against commercial EMTP software and the results show remarkable correspondence.

Another significant advantage of the proposed co-simulation approach for CoTDS dynamic simulation is that existing software for transmission dynamics and a power flow solver for three-phase distribution system can be used. The distribution system dynamics are handled using an intermediate software by solving the dynamic equations of the node-level dynamic components and exchanging interface variables at every simulation time-step.

CHAPTER 3.   DG INVERTER MODELING FOR COTDS CO-SIMULATION

3.1   DG Inverter Modeling Background

With the proliferation of renewable energy sources, DG modeling has become a significant topic of research. A DG unit operates from sources like Photo-Voltaic (PV) arrays, wind, fuel-cells, biomass and geothermal, steam or gas turbines and reciprocation internal combustion engines. An DG unit can operate in two modes, which is grid-connected (grid-tied) mode and islanded (emergency or autonomous) mode. In grid-connected mode, the DG unit is connected to the main power grid and either receives power or injects some power into the main system. In islanded mode, the DG unit is disconnected from the main grid, it operates autonomously like physical islands.

The DG units such as PV, fuel cells, etc., which have DC voltage sources need a DC-AC inverter. The DG inverters are broadly of two types. One is the Voltage-Control Mode , also referred to as the grid-forming inverter and the second is the Current Control Mode , also referred to as the grid-feeding inverter [20]. A grid-supporting inverter is a combination of both these types.

The Grid forming inverter control is conventionally referred as the V-F control (for Voltage, Frequency control). The grid forming inverters are controlled in closed loop to operate as ideal voltage sources with a given voltage amplitude and frequency presenting a very low output impedance. In case of failure of main grid one of the DGs can act as a grid forming inverter and form as the reference for other DGs thereby forming a Microgrid.
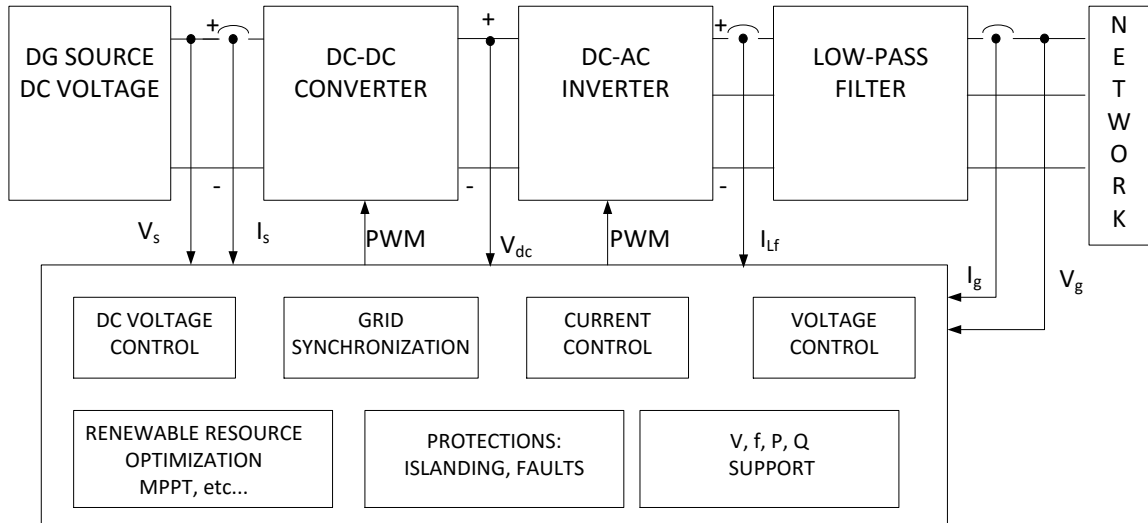
Figure 3.1   High-level block diagram of Grid connected DG Inverter and associated functions

The Grid feeding inverter control is conventionally referred as the P-Q control (for Active Power, P and Reactive Power, Q control). Grid feeding inverters are controlled as current sources presenting high parallel output impedance. Active Power, P and Reactive Power, Q are Inputs to these inverters and the output is a current synchronized with the existing grid. Grid feeding inverters need an existing grid voltage (either the main utility or from a grid-forming inverter) to operate.

The Grid supporting inverter control is conventionally referred as the Droop control. The primary objective of grid-supporting inverter acting as current source is to deliver active power, P and reactive power, Q. However, P and Q are adjusted by a factor associated with the droop equations to support the regulation of grid voltage and frequency.

In practice, the grid-connected inverters [20] are more popular and therefore, in this chapter the grid-feeding inverter modeling is considered. A high-level block diagram is shown in Fig. 3.1

3.2 Simscape 3-phase sine wave model

To generate reference results for calibration, the DG inverter performance simulation is conducted using Simscape-PowerSystems software using the full sine wave model. This is necessary as this shows the actual performance of the inverter.

3.2.1 Model Block Diagram

A 3-phase sine-wave model block diagram of a distribution generator inverter operating in grid feeding mode is shown in Fig. 3.2 [20]. The operation of these inverters is generally preceded by an maximum power point tracking (MPPT) controller or some higher level controller, which sets the reference values for P_{ref} and Q_{ref} for the inverter.
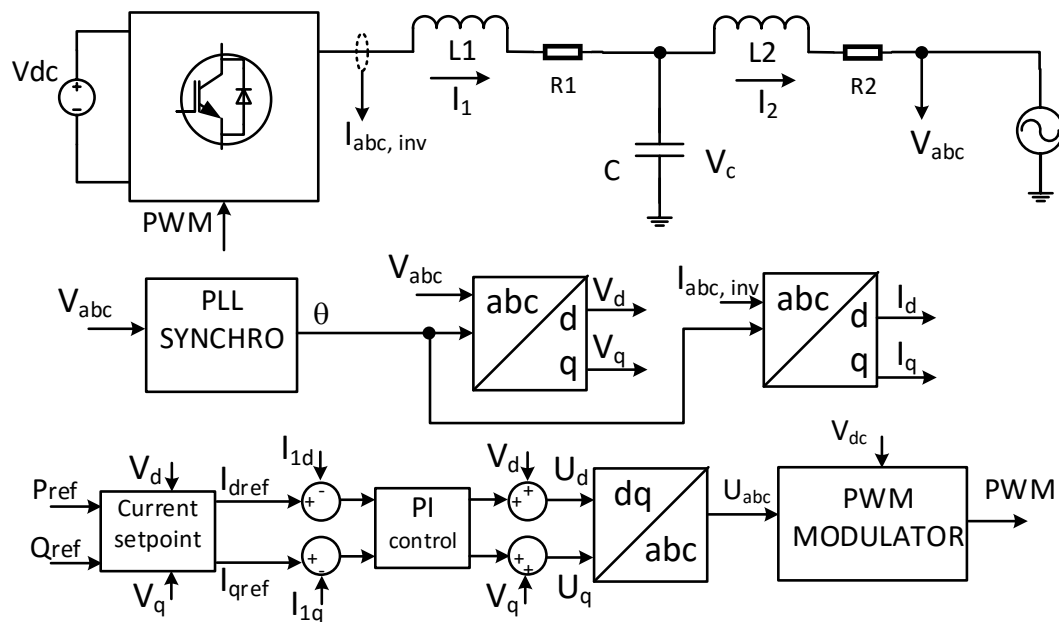
Figure 3.2   DG Inverter control block diagram

In this model, the DC voltage source (from the battery, solar panel, etc...) goes to the PWM inverter which then puts out a voltage that passes through a third order filter to get connected to the grid. The current output from the inverter is controlled by the PWM switching which is generated by the PWM modulator. The 3-phase sinusoidal voltage is

converted to its corresponding d-q components and along with the reference active and reactive power (P_{ref} and Q_{ref}) create the reference I_{dref} and I_{qref}. This goes through the PI controller to generate the required target inverter voltages in the d-q reference frame. Converting back to the *abc* reference frame provides the input to the PWM modulator block which then computes the required PWM for the inverter. This whole control system is now modeled in SimscapePowerSystems

3.2.2 Simulation Setup

The phasor domain model is validated against the actual full sine wave model using Simscape PowerSystems software. The detailed model and the simulation setup is shown in Fig. 3.3. Initially the DG inverter is allowed to come to steady state at a reference power input of $P_{ref} = 0$ and $Q_{ref} = 0$. Then, at $t = 1$s, the P_{ref} is changed from 0 to 100kW.

3.2.3 Model Parameters

The DG inverter model has the following parameter values for the DG components:

- Inductor $L1 = 1$mH

- $L1$ DC resistance, $R1 = 0.15$ Ω

- Inductor, $L2 = 1$mH

- $L2$ DC resistance, $R2 = 0.15$ Ω

- $C = 22$ μ F

- PI controller proportional constant, $k_p = 1$

- PI controller integral constant, $k_i = 10$

- Voltage rating 480 Vrms

- Power rating 100kW

3.2.4   Simulation Results

First the simulation is performed using the complete switching model including the high-frequency switching inverter. To perform this simulation, the time step needs to be extremely small because the simulation captures the fine details of the PWM switching. The results of this simulation is shown in Fig. 3.4. Then the switching inverter is by-passed and replacing the PWM portion of the inverter alone with an average model to still capture the sinusoidal detail without the PWM switching. The results of this are shown in Fig. 3.5. It can be seen that results are identical except for the switching ripple on the inductor current.

The d- and the q- component currents from the inverter into the grid is shown in Fig. 3.6 and the corresponding power changes of the full sine wave model is shown in Fig. 3.7. This is the transient power, both active power and reactive power as fed by the DG inverter into the grid. It can be seen that when there is a change in the reference active power, there is dynamic behavior of the reactive power also.

The results obtained from the SimscapePowersystems using the full- sine wave model, thereby provides the calibration data for comparing against simpler time-efficient phasor-domain model that will be needed for performing dynamic co-simulation with DG inverters in the distribution system. The phasor-domain model will be discussed now in the next section.
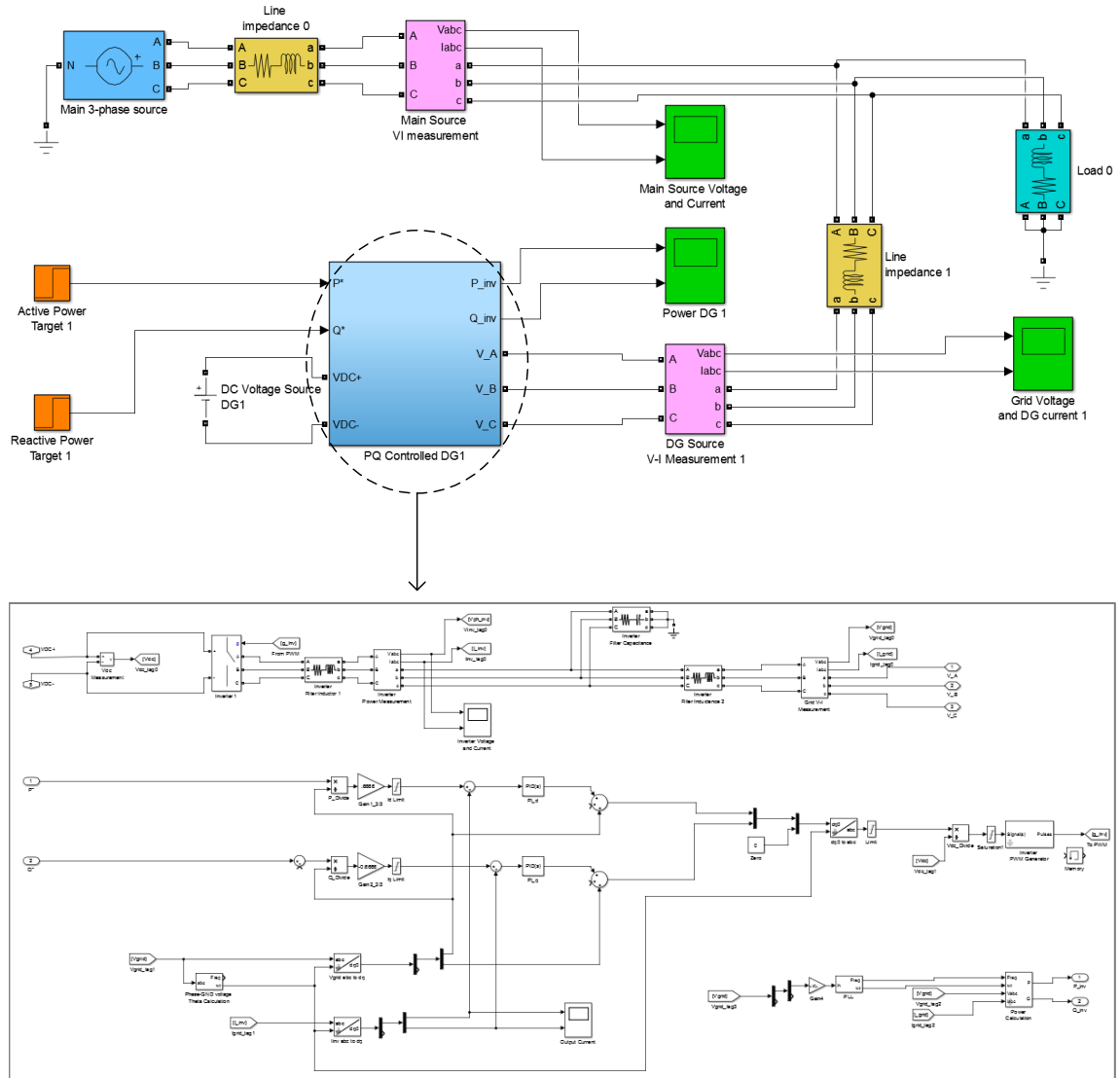
Figure 3.3   Simulation Setup of full sine wave DG model using the block diagram of Fig.3.2.
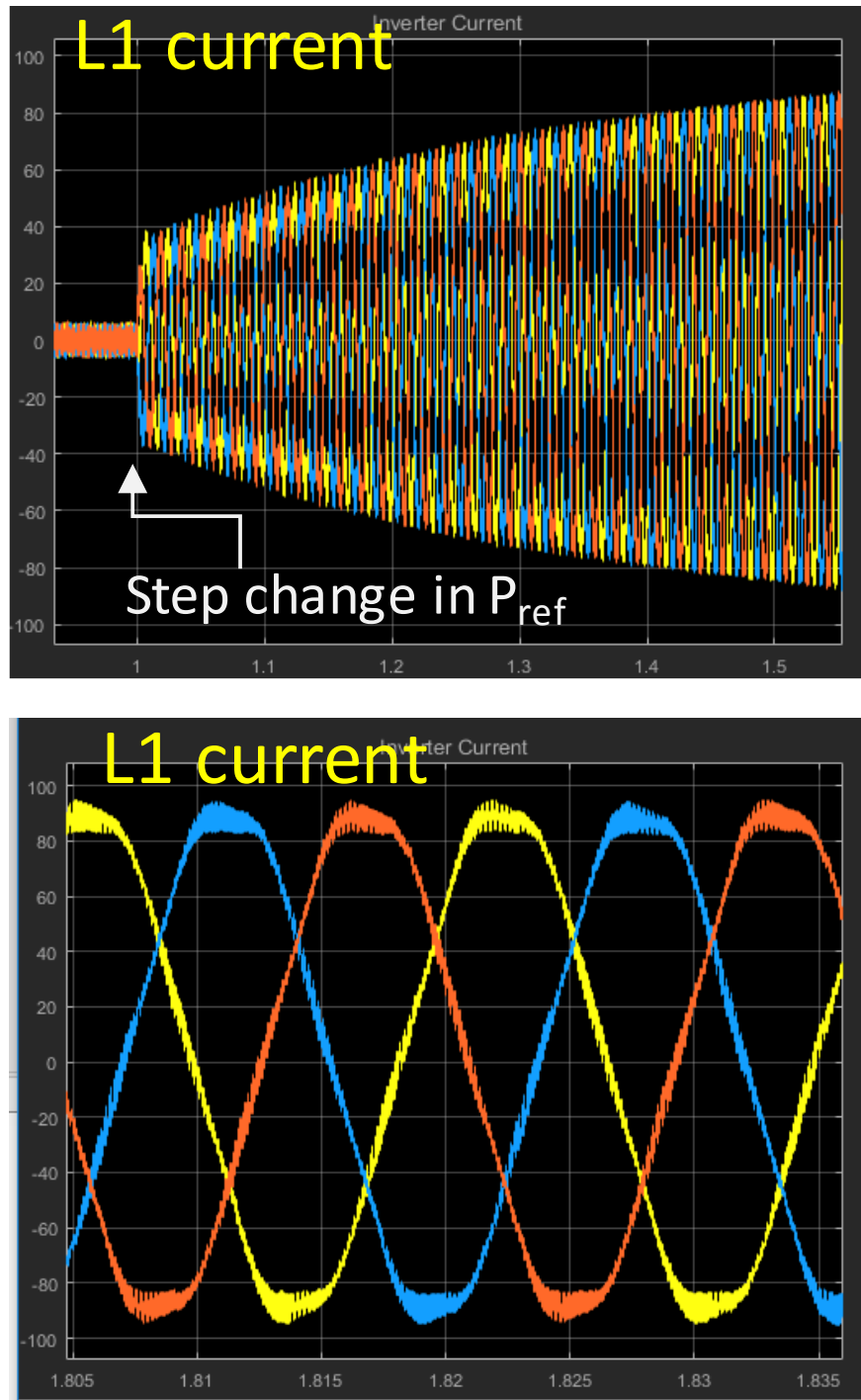
Figure 3.4   Inductor current of full sine wave DG model including high-frequency switching inverter using the block diagram of Fig.3.2.
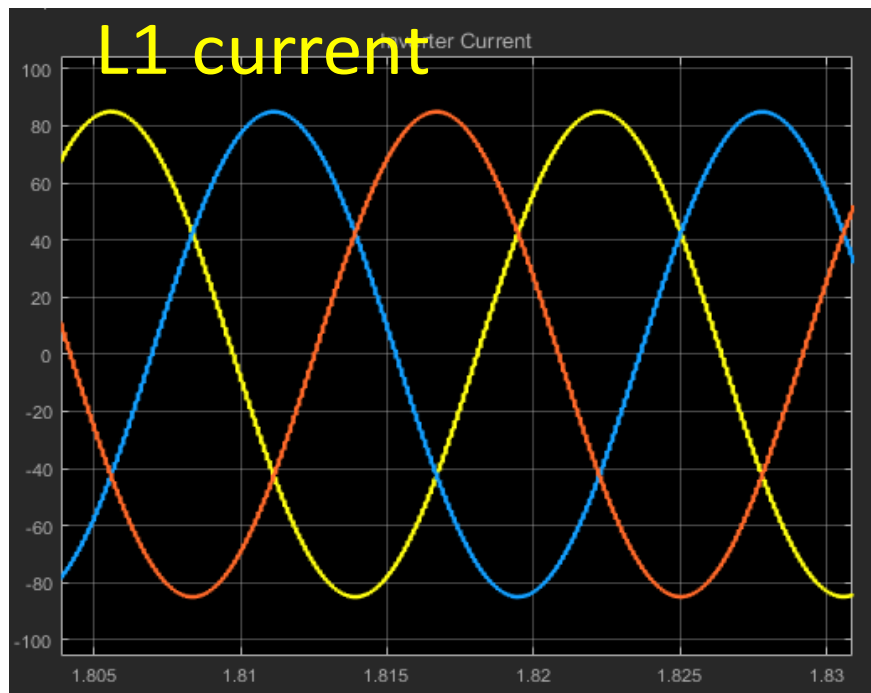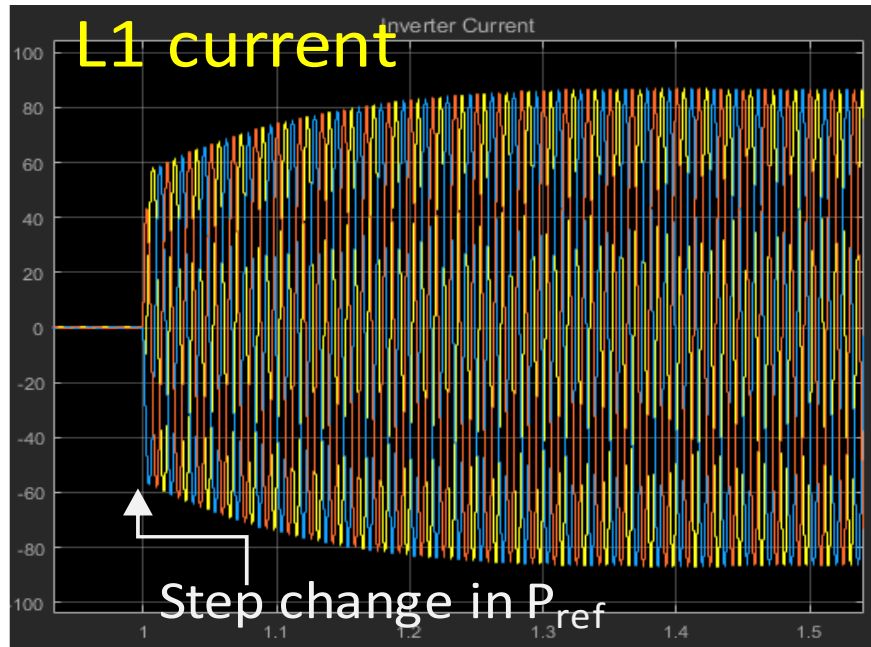
Figure 3.5   Inductor current of full sine wave DG model excluding high-frequency switching inverter.
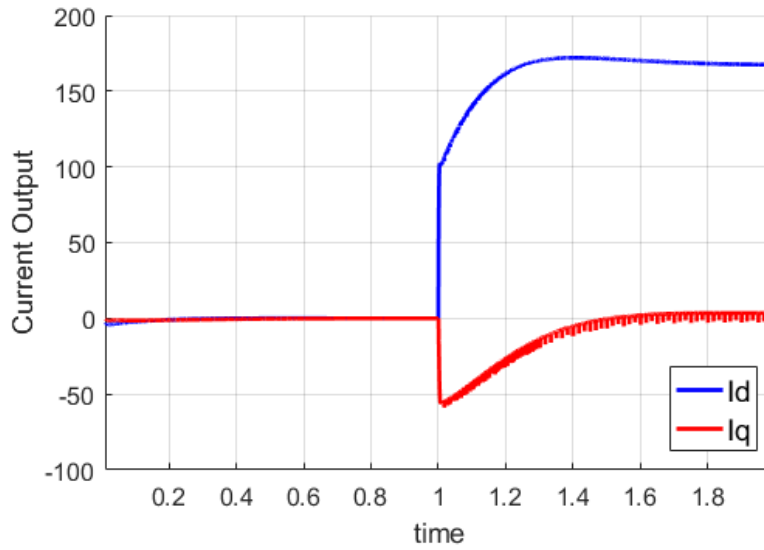
Figure 3.6   d- and q- component current output (current in L2) from the inverter into the grid with the full sine wave model using SimscapePowerSystems
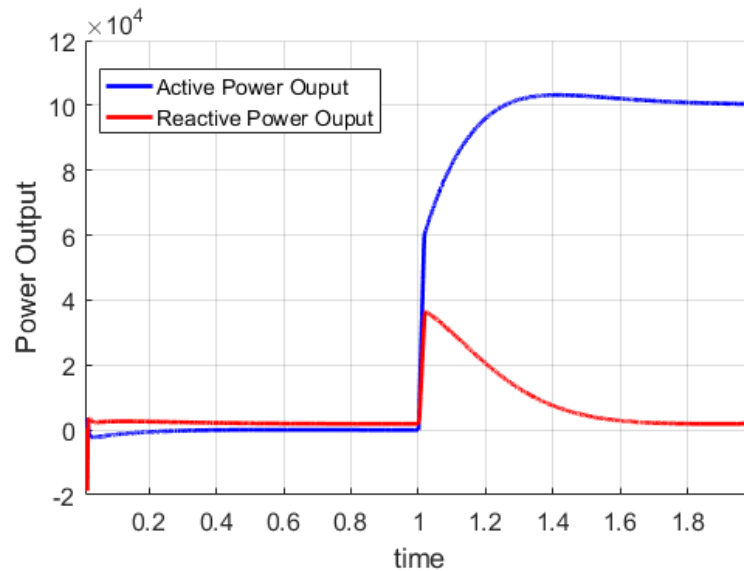
Figure 3.7   Power from DG into the grid from the inverter into the grid with the full sine wave model using SimscapePowerSystems

3.3 Conventional Phasor Domain Inverter Modeling in literature

As opposed to a full blown sinusodal model, phasor domain models have the benefit of faster simulation as the detailed sinusoidal waveform information is not modeled. However, for the purpose of co-simulation with transmission system, we are interested in seeing the dynamic variation of the power injection into the grid for any dynamic events. In literature, the DG models in general are either steady state models or simple behaviour model of the DG inverter control loop. In this section, we discuss the results using the conventional DG inverter modeling that is used in literature [GE model, 2013 journal paper].

3.3.1 Model Block Diagram

The Fig. 3.8 shows the model block diagram of the conventional DG inverter model. The P_{ref} and Q_{ref} along with the d- and the q- component of the grid voltage, create the current reference which are input to a first-order low-pass filter with time constants representing the overall time constant of the converter to give the resulting actual d- and the q- currents. This is to compute the dynamically varying output active power and reactive power into the grid.
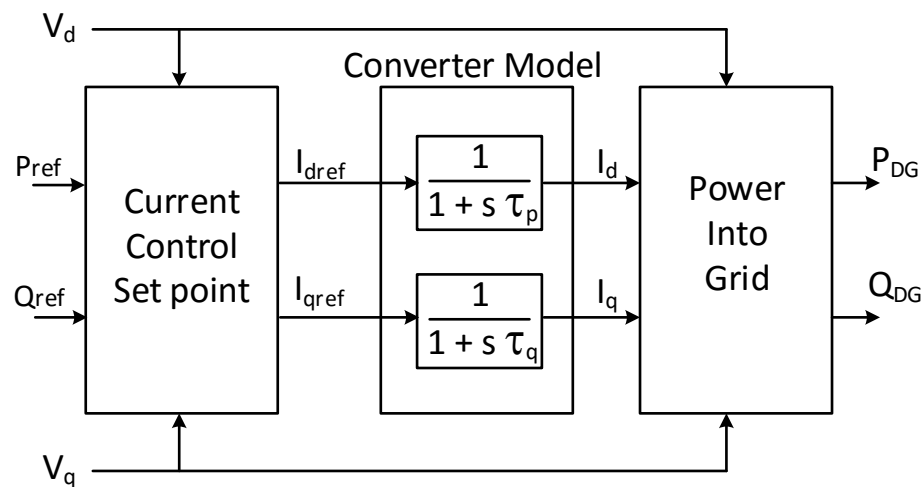
Figure 3.8   Power from DG into the grid from the inverter into the grid with the full sine wave model using SimscapePowerSystems

3.3.2 Model Equations

In the model shown in Fig. 3.8, the current set points are obtained based on the desired active power and reactive power and the measurements of terminal voltage in the dq reference frame as follows:

$$\begin{bmatrix} i_{d,ref} \\ i_{q,ref} \end{bmatrix} = \begin{bmatrix} v_d & v_q \\ v_q & -v_d \end{bmatrix} \begin{bmatrix} P_{ref} \\ Q_{ref} \end{bmatrix} \tag{3.1}$$

The low-pass filter model yields the following two first order differential equations.

$$\begin{aligned} \frac{di_d}{dt} &= \frac{1}{\tau}(i_{d,ref} - i_d) \\ \frac{di_q}{dt} &= \frac{1}{\tau}(i_{q,ref} - i_q) \end{aligned} \tag{3.2}$$

The output power from the DG inverter can be then computed from the two algebraic equations as follows:

$$\begin{aligned} P_{DG} &= v_d.i_d + v_q.i_q \\ Q_{DG} &= v_q.i_d - v_d.i_q \end{aligned} \tag{3.3}$$

3.3.3 Simulation Results

From Fig. 3.9 and Fig. 3.10, it can be seen that the conventional model does not capture the dynamics accurately as determined by the full sine-wave model simulation performed in SimscapePowersystems with the complete inverter control. Therefore, this may not be sufficient to conduct dynamic simulation in the presence of DG inverters.
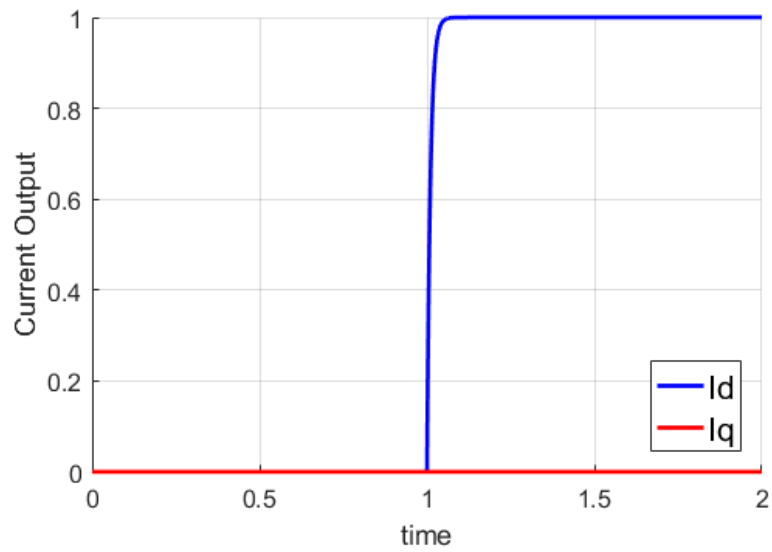
Figure 3.9   d- and q- component current output (current in L2) from the inverter into the grid with the conventional phasor domain DG model.
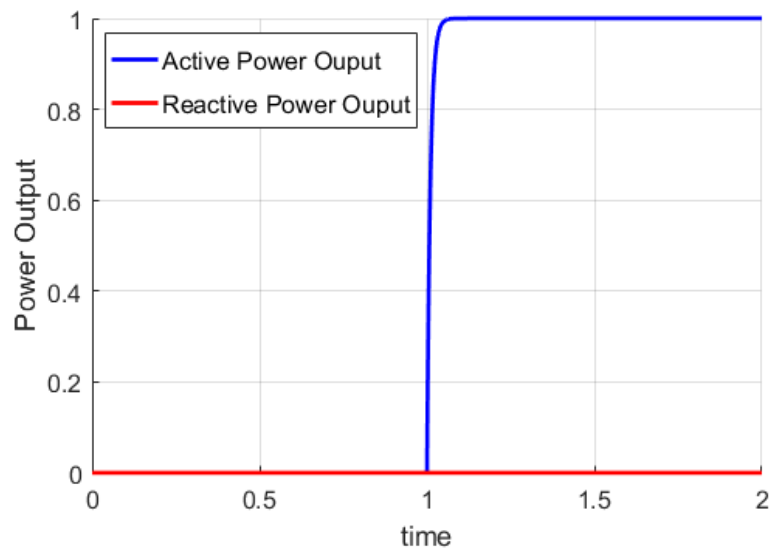
Figure 3.10   Power from DG into the grid from the inverter into the grid with the conventional phasor domain DG model.

3.4 Detailed Phasor-Domain Modeling

In this section, the full sine-wave block diagram of the DG inverter model shown in Fig. 3.2 is used to develop a phasor-domain model that will be effective for co-simulation and at the same time more accurate than the conventional phasor domain model that was presented in the previous section.

3.4.1 Modeling Formulation of Phasor Domain Equations

The current references $I_{d,ref}$ and $I_{q,ref}$ are first generated from the P_{ref} and Q_{ref}.

$$\begin{bmatrix} i_{d,ref} \\ i_{q,ref} \end{bmatrix} = \begin{bmatrix} v_d & v_q \\ v_q & -v_d \end{bmatrix} \begin{bmatrix} P_{ref} \\ Q_{ref} \end{bmatrix} \tag{3.4}$$

Next, we write the PI control loop equations for I_d and I_q to provide the ΔV_d and ΔV_q.

$$\Delta V_d = K_p.(I_{d,ref} - I_{1d}) + K_i. \int (I_{d,ref} - I_d).dt$$
$$\Delta V_q = K_p.(I_{q,ref} - I_{1q}) + K_i. \int (I_{q,ref} - I_d).dt \tag{3.5}$$

where, K_p and K_i are the proportional and integral constants of the PI controller. Defining λ with the dimension of charge as the integral of the difference between the reference and the actual current in $L1$ in d- and q- axis.

$$\lambda_d = \int (I_{d,ref} - I_d).dt$$
$$\lambda_q = \int (I_{q,ref} - I_q).dt \tag{3.6}$$

Now, equation (3.5)

$$\Delta V_d = K_p.\frac{d\lambda_d}{dt} + K_i. \int \lambda_d.dt$$
$$\Delta V_q = K_p.\frac{d\lambda_q}{dt} + K_i. \int \lambda_q.dt \tag{3.7}$$

The dq reference voltage to the inverter, U_d and U_q now becomes

$$U_d = V_d + \Delta V_d$$
$$U_q = V_q + \Delta V_q \tag{3.8}$$

The state equations for the filter circuit as given by $L1$, C and $L2$ is given by,

$$U_d - V_{cd} = L_1.\frac{dI_{1d}}{dt} - \omega_b.I_{1q} + R_1.I_{1d}$$

$$U_q - V_{cq} = L_1.\frac{dI_{1q}}{dt} + \omega_b.I_{1d} + R_1.I_{1q}$$

$$I_{1d} - I_{2d} = C.\frac{dV_{cd}}{dt} - \omega_b C.V_{cq}$$

$$I_{1q} - I_{2q} = C.\frac{dV_{cq}}{dt} + \omega_b C.V_{cq} \qquad (3.9)$$

$$V_{cd} - V_d = L_2.\frac{dI_{2d}}{dt} - \omega_b.I_{2q} + R_2.I_{2d}$$

$$V_{cq} - V_q = L_2.\frac{dI_{2q}}{dt} + \omega_b.I_{2d} + R_2.I_{2q}$$

where, I_1, I_2 and V_c are the inductor currents ($L1$ and $L2$) and capacitor (C) voltage respectively of the output filter as shown in Fig. 3.2. $R1$ and $R2$ are the resistances of the two inductors, $L1$ and $L2$ respectively.

The complete phasor domain differential equations, describing the inverter corresponding to Fig. 3.2, are written in standard from and shown in equation (3.10).

$$\frac{dI_{1d}}{dt} = -\frac{(R_1 + K_p).I_{1d}}{L_1} + \omega_b.I_{1q} - \frac{V_{cd}}{L_1} + \frac{K_i.\lambda_d}{L_1}$$

$$+ \frac{K_p}{L_1}.\frac{P_{ref}}{V_d} + \frac{V_d}{L_1}$$

$$\frac{dI_{1q}}{dt} = -\frac{(R_1 + K_p).I_{1q}}{L_1} - \omega_b.I_{1d} - \frac{V_{cq}}{L_1} + \frac{K_i.\lambda_q}{L_1}$$

$$+ \frac{K_p}{L_1}.\frac{Q_{ref}}{V_d} + \frac{V_q}{L_1}$$

$$\frac{dV_{cd}}{dt} = \frac{I_{1d}}{C} + \omega_b.V_{cq} - \frac{I_{2d}}{C}$$

$$\frac{dV_{cq}}{dt} = \frac{I_{1q}}{C} - \omega_b.V_{cd} - \frac{I_{2q}}{C} \qquad (3.10)$$

$$\frac{dI_{2d}}{dt} = \frac{V_{cd}}{L_2} - \frac{R_2.I_{2d}}{L_2} + \omega_b.I_{2q} - \frac{V_d}{L_2}$$

$$\frac{dI_{2q}}{dt} = \frac{V_{cq}}{L_2} - \frac{R_2.I_{2q}}{L_2} - \omega_b.I_{2d} - \frac{V_q}{L_2}$$

$$\frac{d\lambda_d}{dt} = -I_{1d} + \frac{P_{ref}}{V_d}$$

$$\frac{d\lambda_q}{dt} = -I_{1d} + \frac{Q_{ref}}{V_d}$$

The algebraic equation for the power from the inverter into the network is given by equation (3.11).

$$P_{DG} = V_d.I_{2d} + V_q.I_{2q}$$

$$Q_{DG} = V_q.I_{2d} - V_d.I_{2q}$$

(3.11)

3.4.2 Simulation Results

Fig. 3.11 shows the d- and q- axis current into the grid with the detailed phasor domain model and 3.12 shows the corresponding power changes for the same simulation setup as the full-sine wave model. The simulation is performed with all parameters converted to p.u. based on the inverter ratings.
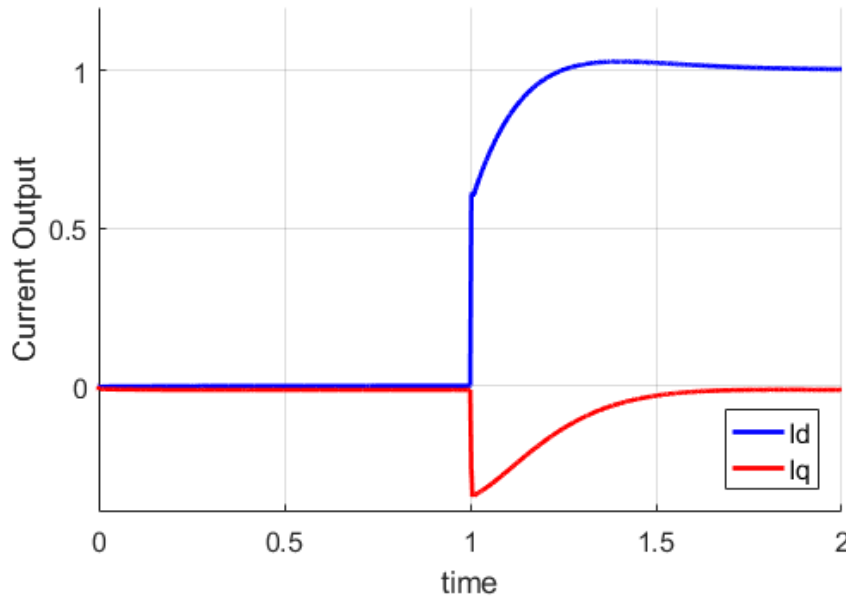
Figure 3.11   d- and q- component current output (current in L2) from the inverter into the grid with the detailed phasor domain DG model.
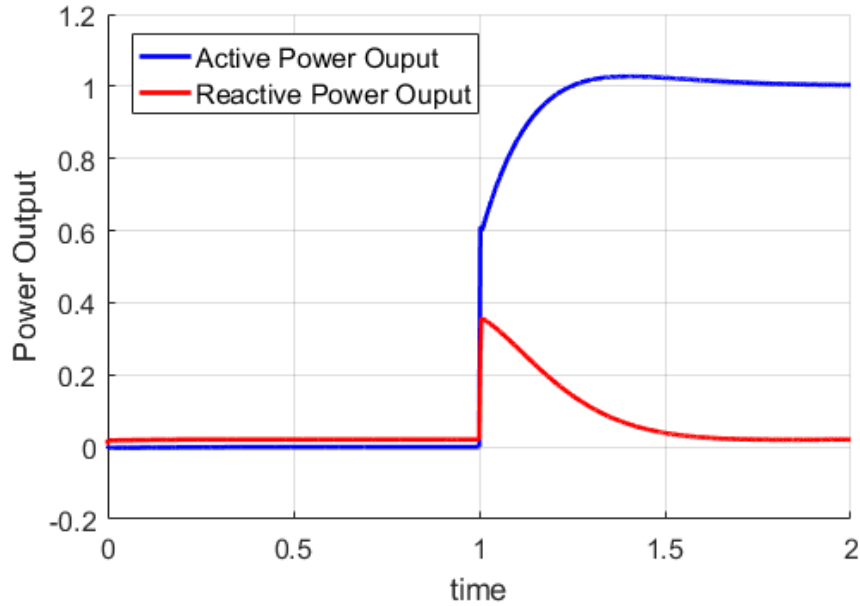
Figure 3.12   Power from DG into the grid from the inverter into the grid the detailed
phasor domain DG model.

From Fig. 3.11 and 3.12, it is quite evident that the dynamic results obtained from
the detailed phasor domain model corresponds very closely with that obtained from the
full-sine wave model using Simscape Powersystems. A comparison of the simulation speeds
is shown in the below table, Table 3.1. It is very clear that the developed detailed phasor
domain model can be used in co-simulation considering the DG dynamics.

Table 3.1   Comparison of Simulation Methods for DG Inverter modeling

Description	Simulation Time	Comments
Simscape Full-Sine-wave Model	Very Slow	Accurate model, includes all internal details.
Conventional Phasor Domain	Fast	Very basic model, misses some critical behaviour
Detailed Phasor Domain	Fast	Accurate and provides the necessary details for power system modeling

3.5   Power System Simulation using DG Inverter Phasor Domain Model

The detailed phasor domain DG model that has been developed is now tested in a power system environment. The objective is to employ the DG model in a power system simulation along with the dynamics of the synchronous generator, exciter and governor on the transmission side. Fig. 3.13 shows the system simulation block. In this system, the synchronous generator located at Bus 1 is connected through a transformer, a transmission line to a load located at Bus 2. A DG inverter located at Bus 3 is connected through a transmisson line to the load at Bus B. The inverter recieves input commands of active and reactive power which are P_{ref} and Q_{ref} respectively.
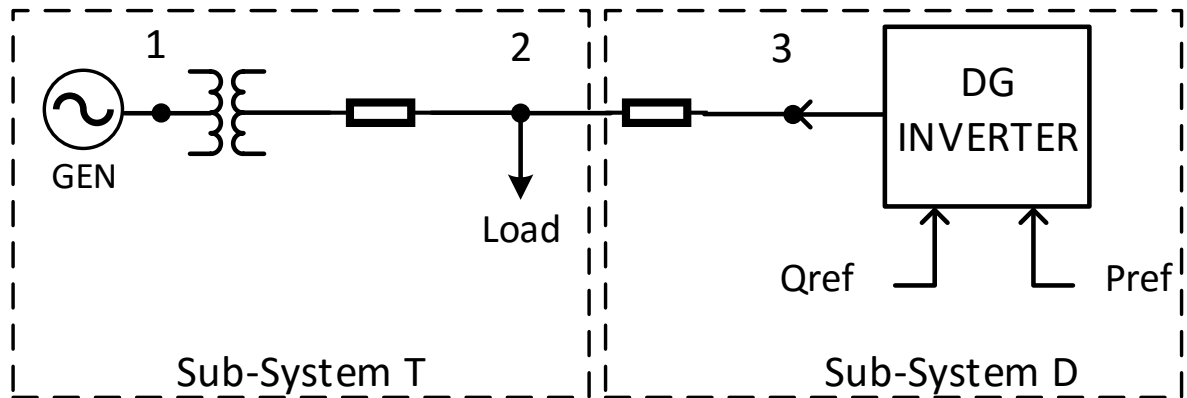
Figure 3.13   Power System simulation with DG inverter.

The system is also split into two sub-systems A and B for further validation of the CoTDS simulation. The eigen values of the two sub-systems are shown in Fig. 3.14 (a) and (b). This figure reveals that the eigen values of the sub-system T which contains the transmission system generator dynamics are relatively lower compared to the eigen values of the sub-system D which includes the DG inverter dynamics. As the DG Inverter contains fast dynamics which lead to the higher eigen values, we can expect that the simulation of the two sub-systems on a single simulation tool, may lead to numerical problems.
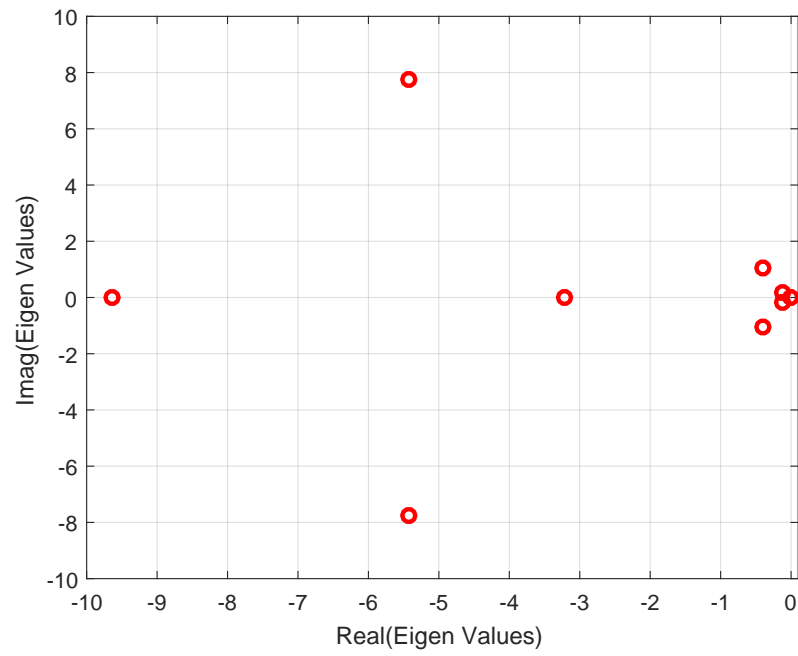
(a)
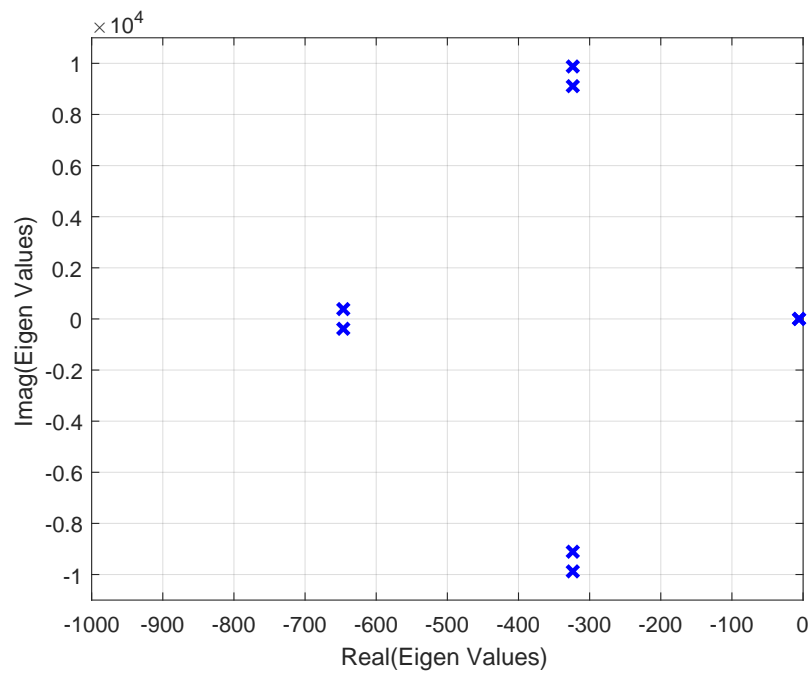
(b)

Figure 3.14   (a) Eigen Values of sub-system T (b) Eigen values of sub-system D

3.5.1 Total system simulation using PSAT

Now we use the detailed phasor-domain model to run the same simulation with the entire system simulated using a single time-domain simulator (PSAT). This is similar to the total system simulation approach described in Chapter 2. It can be observed from Fig. 3.15(a), that the presence of fast dynamics of the DG inverter along with the slow dynamics of the transmission system causes wide numerical fluctuations at a normal time step size of 0.062s although it seems converging towards the true solution. When the step size is reduced significantly to 0.00062s, the oscillations are reduced yielding a cleaner simulation result as shown in Fig. 3.15(b). This however is at the penalty of much higher simulation time.
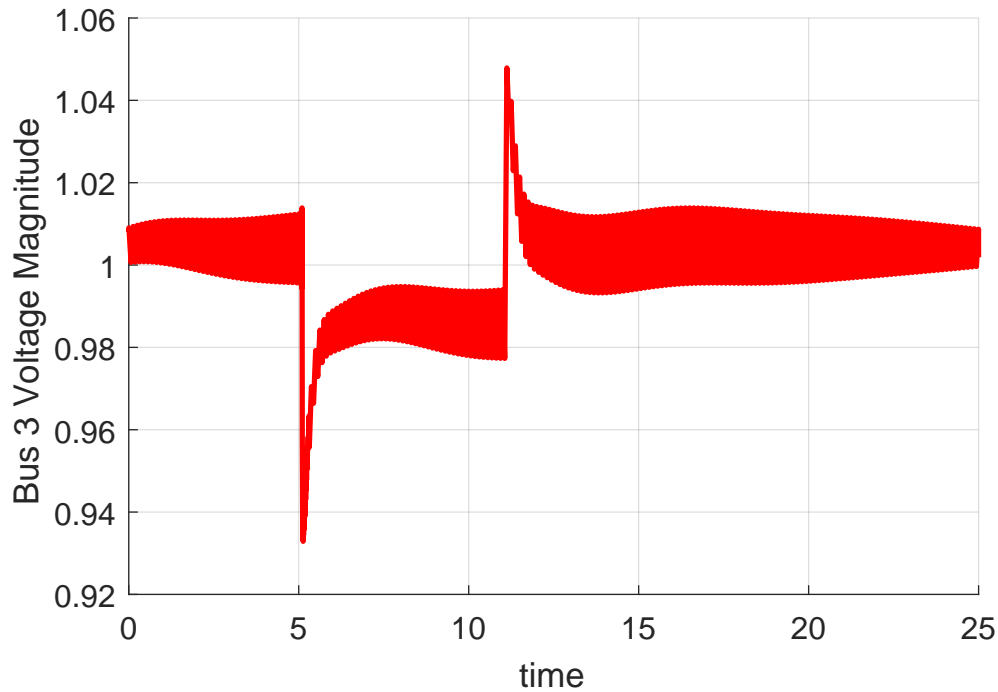
(a) Simulation time-step = 0.062s
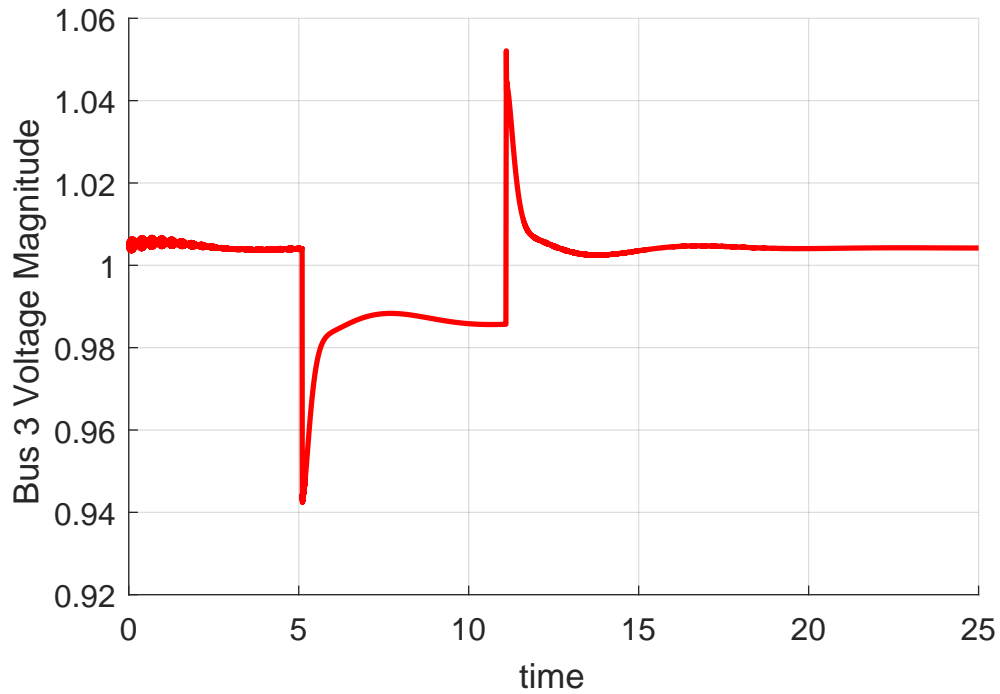
(b) Simulation time-step = 0.00062s

Figure 3.15   Dynamics observed on the Bus 2 voltage with total system simulation using PSAT for different simulation time steps

3.5.2   Simulation results using CoTDS simulation

On the other hand when the simulation is performed using the co-simulation approach described in Chapter 2 with the complete system split into two sub-systems shown in Fig.3.13, then even with larger step size (corresponding to exchange of data), the simulation results are clean without any noticeable wide numerical oscillations. Table 3.2 summarizes the simulation times and relative accuracy of these simulation approaches.
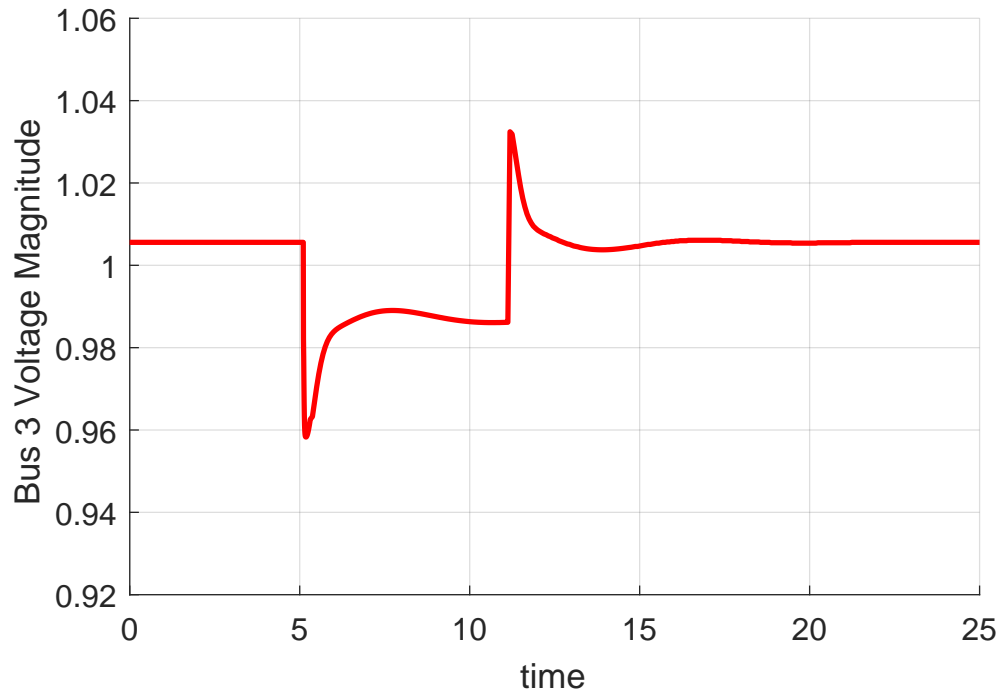
Figure 3.16   Dynamics observed on the Bus 2 voltage with dynamic co-simulation performed with large exchange step size.

Table 3.2   Simulation Comparison of Total System simulation with CoTDS simulation

Description	Simulation Time	Comments
Total System Simulation, Time-step = 0.06s	27s	Numerical problems observed
Total System Simulation, Time-step = 0.0006s	1782s	Numerical problems reduced
CoTDS simulation	22s	No Numerical problems

3.6   Conclusions

In this chapter a phasor domain model of the DG DC-AC inverter operating in the grid-connected mode was developed and validated against the full-sine wave switching model using Simscape Power systems software. The results show excellent correspondence and hence the model can be further used in CoTDS dynamic simulation to study the effect of DGs in the distribution system.

A significant advantage of this model is that the for the purpose of CoTDS simulation, what is essential is how the P_{DG} and Q_{DG} injections would vary with time for a dynamic event. And this is exactly captured in the phasor domain model. The advantage with this model is that the simulation time is dramatically reduced as we are no longer capturing the sine wave details, but still maintaining all the control details.

When the model is adopted in power system simulation along with transmission system dynamics, it is observed that the time-domain simulation experiences numerical issues at normal simulation time step. The simulation time step has to be significantly reduced to overcome these numerical problems.

However, with CoTDS simulation, the numerical problems are eliminated due to separately solving the DG dynamics in its own sub-system without subjecting the entire system to small time step size. This significantly improves the simulation time and at the same time maintaining the accuracy of the performance result as compared to reference sine-wave model simulation using SimscapePowersystems.

CHAPTER 4.   DISTRIBUTION SIDE VOLTAGE CONTROL STUDY WITH DG USING COTDS CO-SIMULATION

4.1   Voltage Control with DG

The distribution generator inverters can be used to regulate the voltage as they are capable of delivering both active power, as governed by the master controller such as a Mean Power Point Tracking (MPPT) controller, as well as reactive power. The control of active and reactive power in the DG inverter is typically modeled using the conventional phasor-domain model as described in Sec. 3.3. But as demonstrated, there is a significant difference in the dynamics when a detailed model is considered. The numerical problems associated with including the detailed model are brought to light. The CoTDS simulation method described in the Chapter 2 is then employed to eliminate these problems and thereby facilitate a more accurate study of voltage control dynamics.
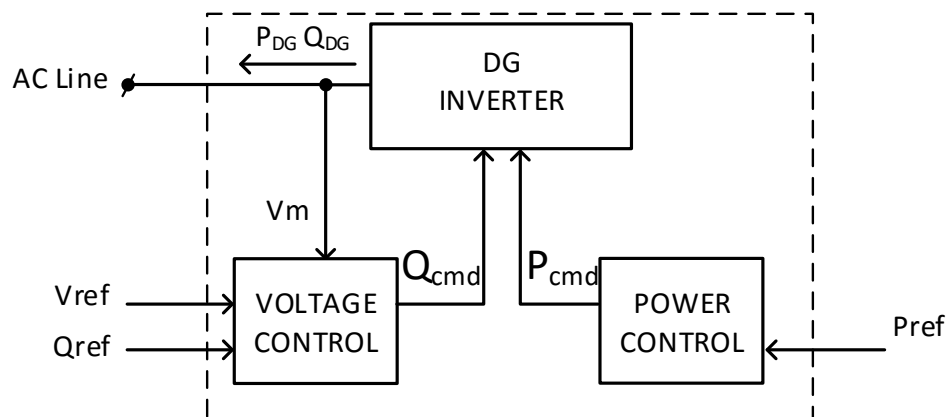
Figure 4.1   DG Inverter with associated Voltage Control and Power Control to generate the corresponding reactive power command and active power command.

Fig. 4.1 shows the block diagram of the voltage control with DG. The voltage reference, V_{ref}, the reactive power reference, Q_{ref} and the active power reference, P_{ref} which then are converted into the actual command that goes to the DG inverter block. The active power command is controlled by mechanisms such as Maximum Power Point Tracking (MPPT), and other other secondary controls which is not the focus of this work.

Here the objective is to study the voltage control which is governed by the functional block shown in Fig. 4.2(a)-(b). The error from the reference to the measured voltage goes to the proportional-integral controller and summed up with the reference reactive power setting to give the reactive power command. The DG inverter produces the output power in accordance to the command thereby actively regulating the voltage. The dynamics of the voltage control now comes into effect through the variation in AC line voltage which is influenced by the loads and other dynamics in the system.

The governing equations for the voltage control loop shown in Fig. 4.2(a) is given by

$$
\begin{aligned}
\frac{dQ_I}{dt} &= K_{iq}.(V_{ref} - V_m) \\
Q_{cmd} &= Q_{ref} + K_{pq}.(V_{ref} - V_m) + Q_I
\end{aligned}
\tag{4.1}
$$

And the governing equations for the voltage control loop with droop control shown in Fig. 4.2(a) is given by

$$
\begin{aligned}
\frac{dQ_I}{dt} &= K_{iq}.(V_{ref} - V_m - V_{DR}) \\
\frac{dV_{DR}}{dt} &= -\frac{1}{T_{DR}}.(K_{DR}.Q_{DG} - V_{DR}) \\
Q_{cmd} &= Q_{ref} + K_{pq}.(V_{ref} - V_m - V_{DR}) + Q_I
\end{aligned}
\tag{4.2}
$$
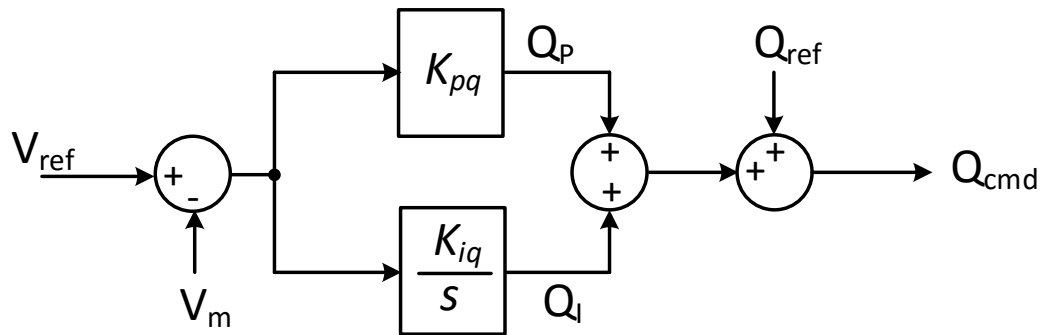
(a)
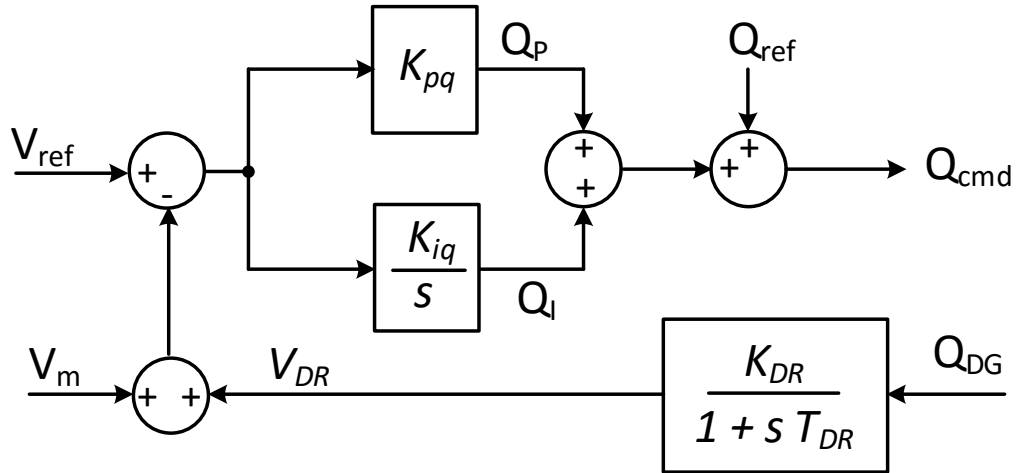
(b)

Figure 4.2   (a) Voltage Control loop to generate reactive power command to DG Inverter.
(b) Voltage Control loop along with droop control to generate reactive power
command to DG Inverter.

4.2 Voltage Control on 3-bus system

Fig. 4.3 shows a 3-bus system with a synchronous generator along with the associated exciter and governor dynamics on Bus 1. The DG inverter along with the voltage control dynamics is placed at Bus 3. There are loads on Bus 2 and Bus 3. The system is subjected to a transient by changing the reference active power P_{ref} which causes the voltages to change. This change in the voltage is compensated by corresponding change in reactive power command and thereby the reactive power output into the line from the DG. This behaviour is studied first by using a sine wave model and then by total system simulation. These results are then compared with the developed co-simulation approach by splitting the entire system into two sub-systems (Sub-System T and Sub-System D).
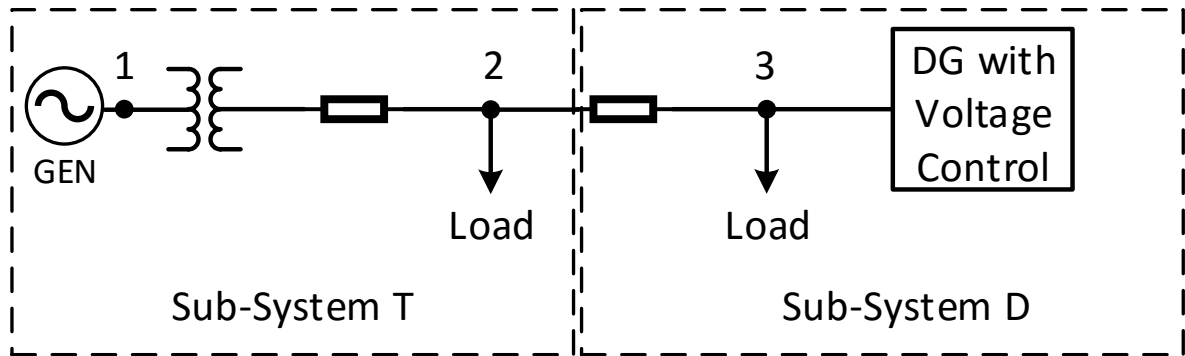
Figure 4.3   Power System simulation with DG inverter with voltage control.

4.2.1 Simulation using Simscape sine wave model

The test setup shown in Fig. 4.3 is first simulated using sine wave model on Simscape Simpowersystems EMTP software. The objective is to regulate the voltage on Bus 3 to 1.0 p.u. using reactive power from the DG inverter. The dynamics of the system is tested using a reference change on the DG active power, P_{ref}. This change is to simulate condition that can practically arise due to solar intermittency for example due to a passing cloud.

The reference input is reduced by 50% and then increased back to original value and both these dynamic events are studied. It can be see that when the reference is reduced, the voltage instantly drops but the reactive power compensation dynamically brings the voltage back to regulation with an increased reactive power. The dynamic waveforms also reveal that the reactive power drops before arriving at the final value. Similar behaviour is also noticed when the active power reference is increased. The voltage waveforms thus captured from this simulation gives us a reference to compare against for validation of the phasor domain models.

(a)
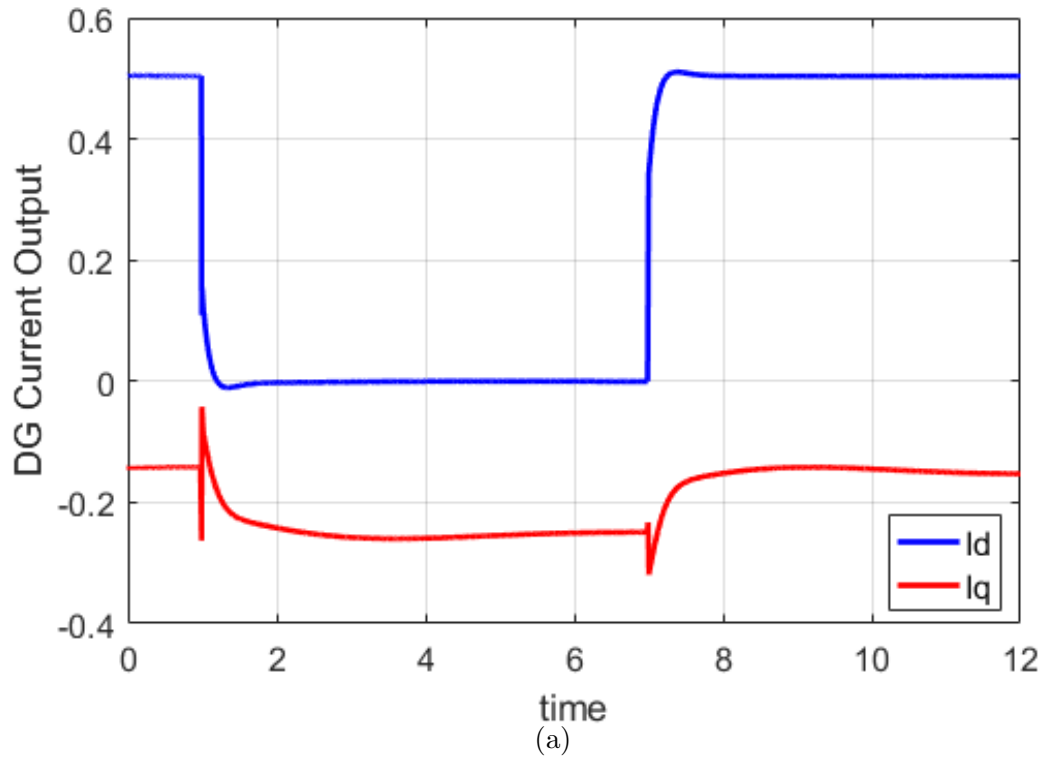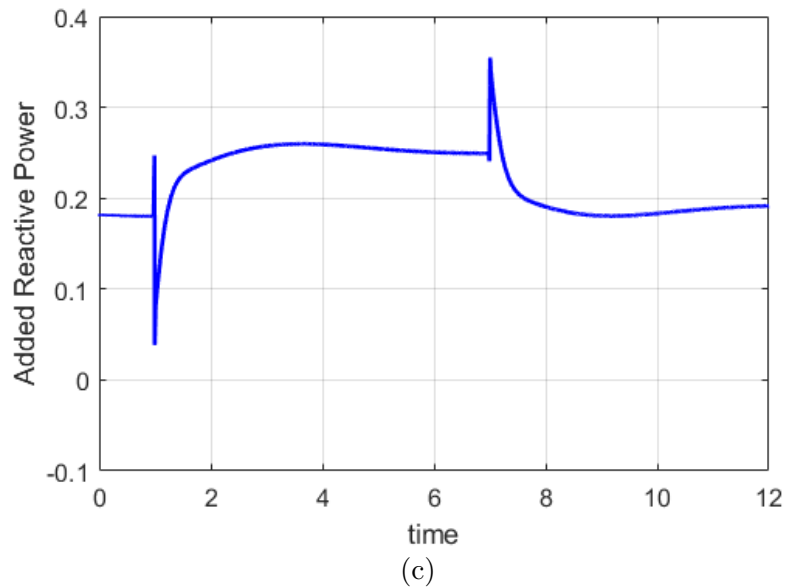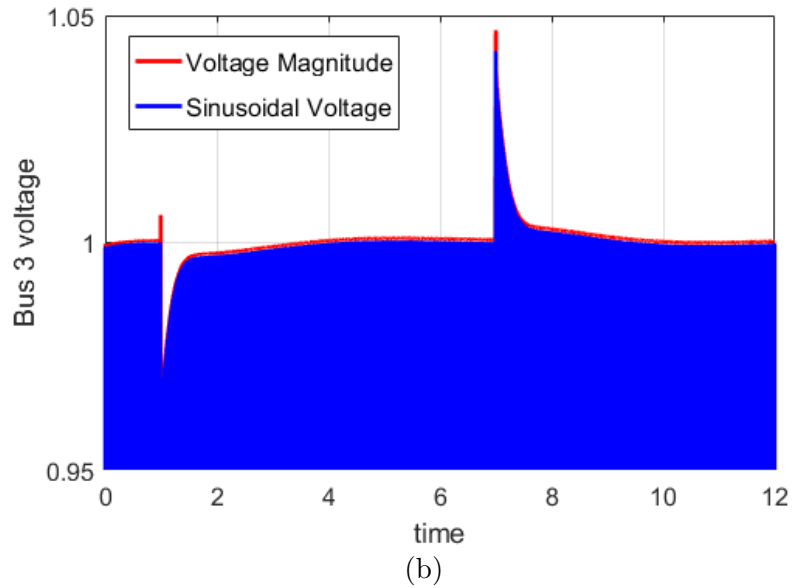
Figure 4.4   Transient results due to a dynamic changes in the DG reference active power, P_{ref} with sine wave SimscapePowersystems simulation. (a) The d- and q-component of the inverter output current (b) The Bus 3 voltage magnitude and the actual sinusoidal voltage (c) The reactive power output from the DG inverter to maintain output voltage at 1.0p.u.

4.2.2   Total system simulation using detailed DG inverter phasor domain model

Now the sub-system A and sub-system B are both together simulated in the same dynamic simulation environment. The DG model that is created in PSAT is modified to include the differential equation arising from the voltage control block used to solve the time domain arising from the voltage control block and the output is added to the original reference reactive power which then becomes the dynamic command to the DG inverter. The following Equation 4.1 is hence added to the DG inverter differential equations.

The simulation results are shown in Fig. 4.5(a)-(c).
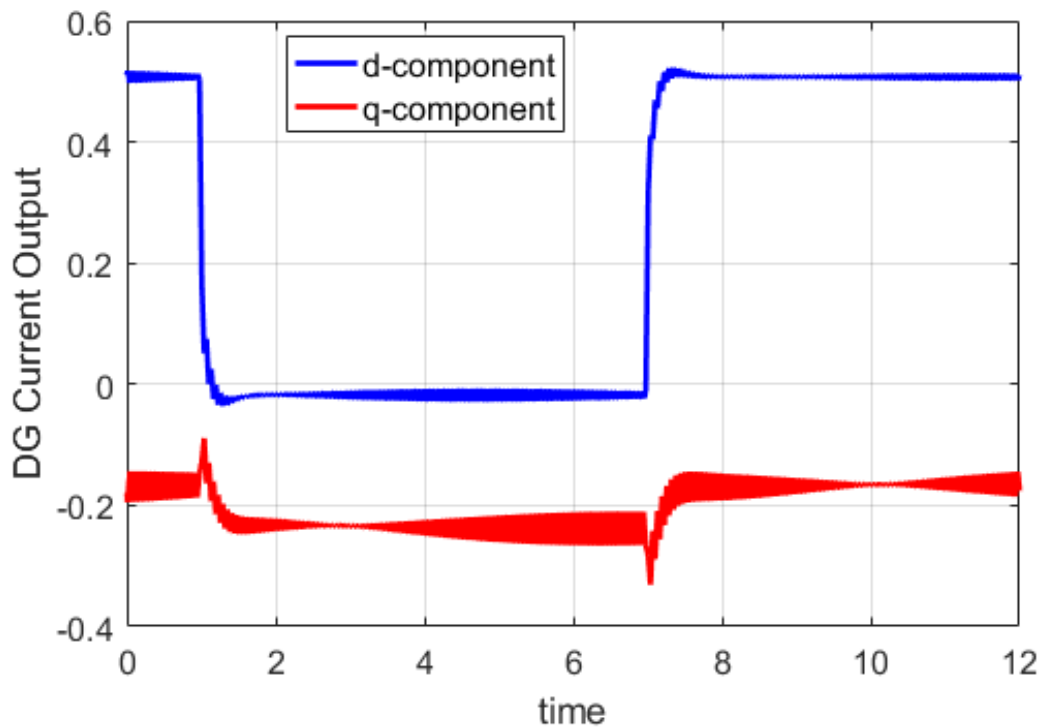
(a)
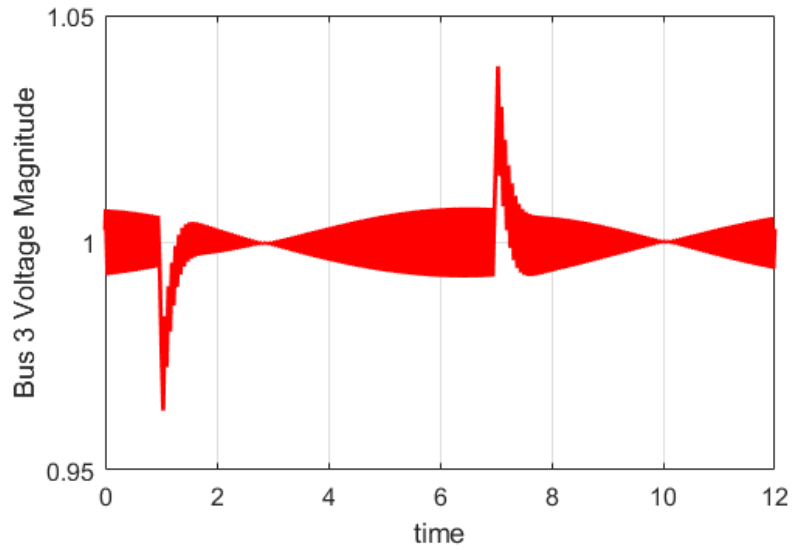
(b)
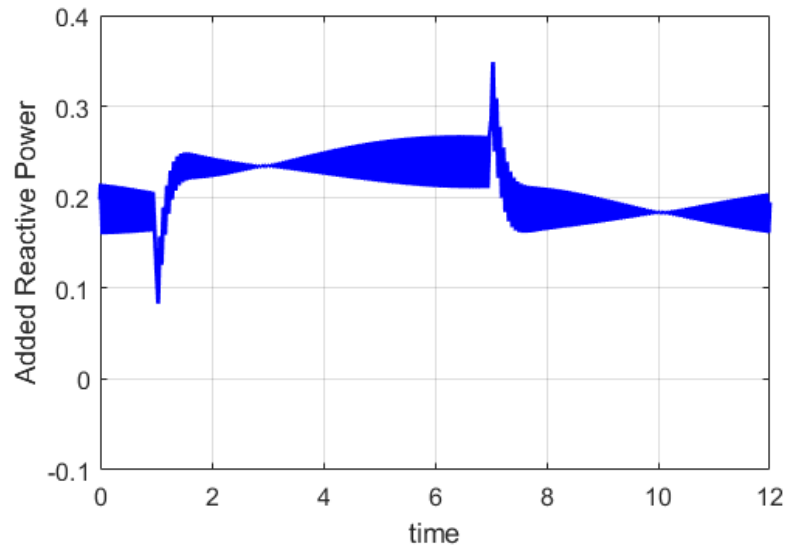
(c)

Figure 4.5   Transient results due to a dynamic changes in the DG reference active power, P_{ref} with the total system simulated with PSAT at a nominal time step of 0.0625s. (a) d- and q- component of DG inverter output current. (b) Bus 3 voltage and (c) Added reactive power from DG to maintain the Bus 3 voltage at 1.0p.u.

It can be observed from the simulation results of Fig. 4.5(b) that the control loop to maintain the voltage at 1.0pu is active. However, there is considerable distortion of the voltage waveform. This is observed also on the corresponding results of the DG current output and the added reactive power. This could either be a result of the voltage control loop instability or numerical instability of the dynamic simulation algorithm.

From Chapter 2, we can recognize that this highly oscillatory mode of numerical results are present when the eigen values are far apart in the system. Since the eigen values introduced from the DG inverter model are larger in magnitude due the presence of fast dynamics, it is possible, that there could be some numerical issues when using the DG model in a single simulation environment. To further evaluate this, we perform a simulation using smaller time steps. To study the performance, we reduce the time step from 0.0625s to 0.000625 sec. The results are shown in Fig. 4.6(a)-(c).
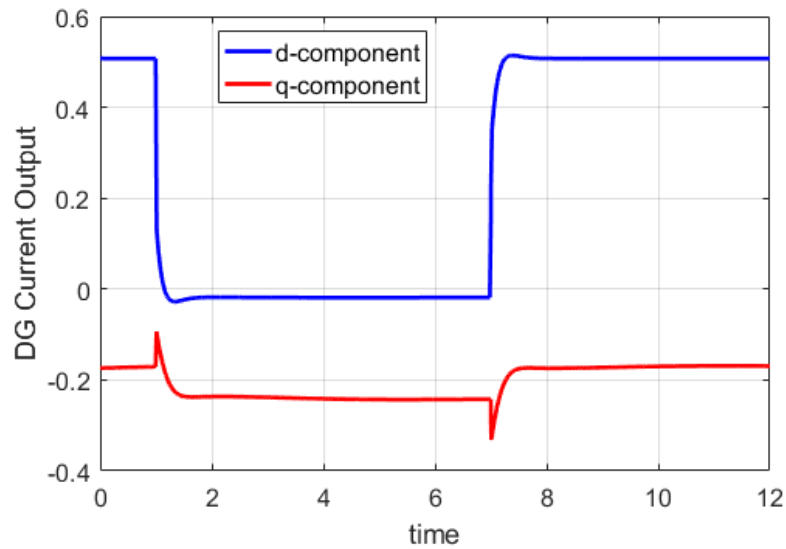
(a)
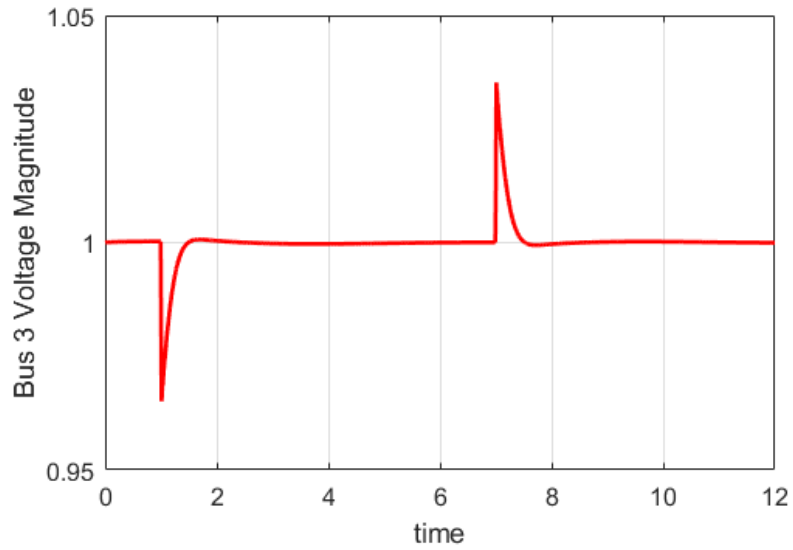
(b)
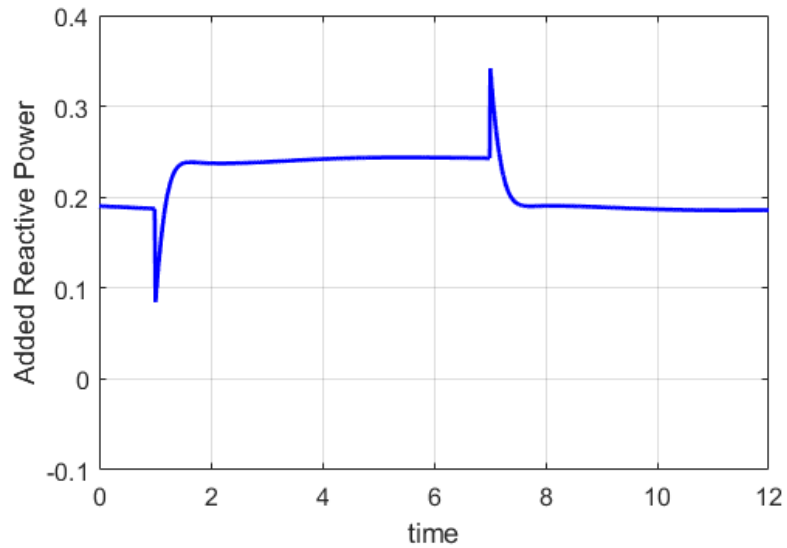
(c)

Figure 4.6 Transient results due to a dynamic changes in the DG reference active power, P_{ref} with the total system simulated with PSAT at a nominal time step of 0.000625s. (a) d- and q- component of DG inverter output current. (b) Bus 3 voltage and (c) Added reactive power from DG to maintain the Bus 3 voltage at 1.0p.u.

It can be clearly seen that the observed oscillations of Fig. 4.5 are not present when the simulations are performed at a smaller time-step in Fig. 4.6. From this we can conclude that to study the performance such as voltage with DG using the detailed DG inverter model, it is necessary to use small time step. This may not always be practical because small time step takes longer simulation time.

4.2.3   CoTDS co-simulation using detailed DG inverter phasor domain model

Now, we apply the CoTDS co-simulation methodology on sub-system T and sub-system D of Fig.4.3. The results are shown in Fig. 4.7 (a)-(b). Here, even at a nominal simulation time-step of 0.0625s, the results show clean behavior without any abnormal numerical oscillations.
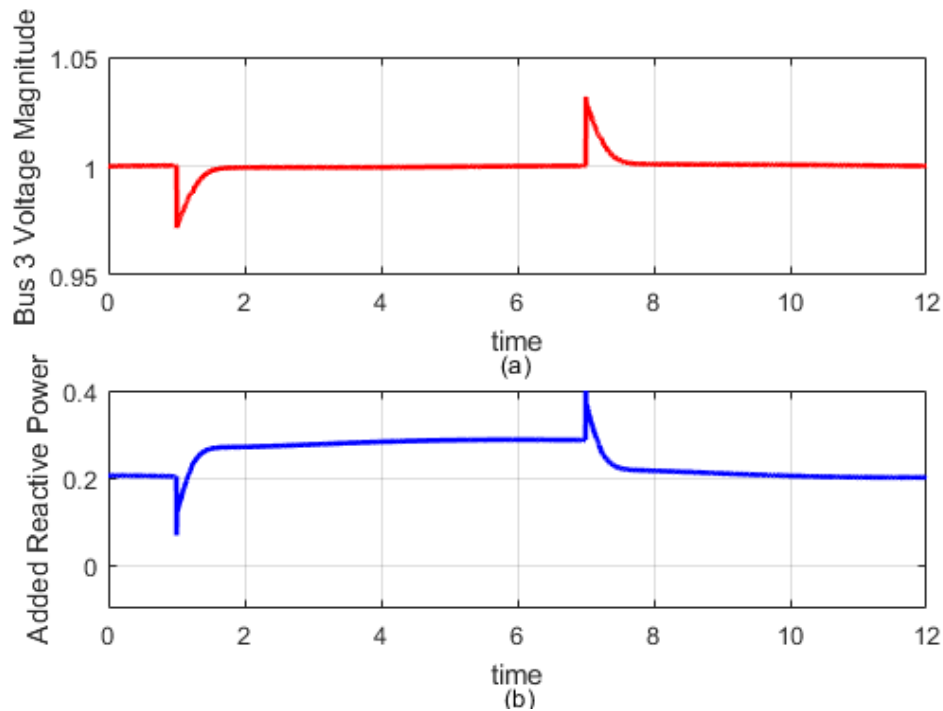
Figure 4.7   Transient results due to a dynamic changes in the DG reference active power, P_{ref} using CoTDS co-simulation methodology at a nominal time step of 0.0625s. (a) Bus 3 voltage and (b) Added reactive power from DG to maintain the Bus 3 voltage at 1.0p.u.

4.3 Voltage Control on a IEEE 9-bus transmission system and 4-node distribution system using CoTDS co-simulation

4.3.1 Simulation Setup

Now, a study of the voltage control loop along with droop control is considered for the setup shown in Fig. 4.8. Here, the system consists of an IEEE 9-bus system with the load Bus 6 expanded into a 4-node distribution system. In the distribution system, the load and DG with voltage control connected to each of the 4 nodes. The voltage control includes droop control.
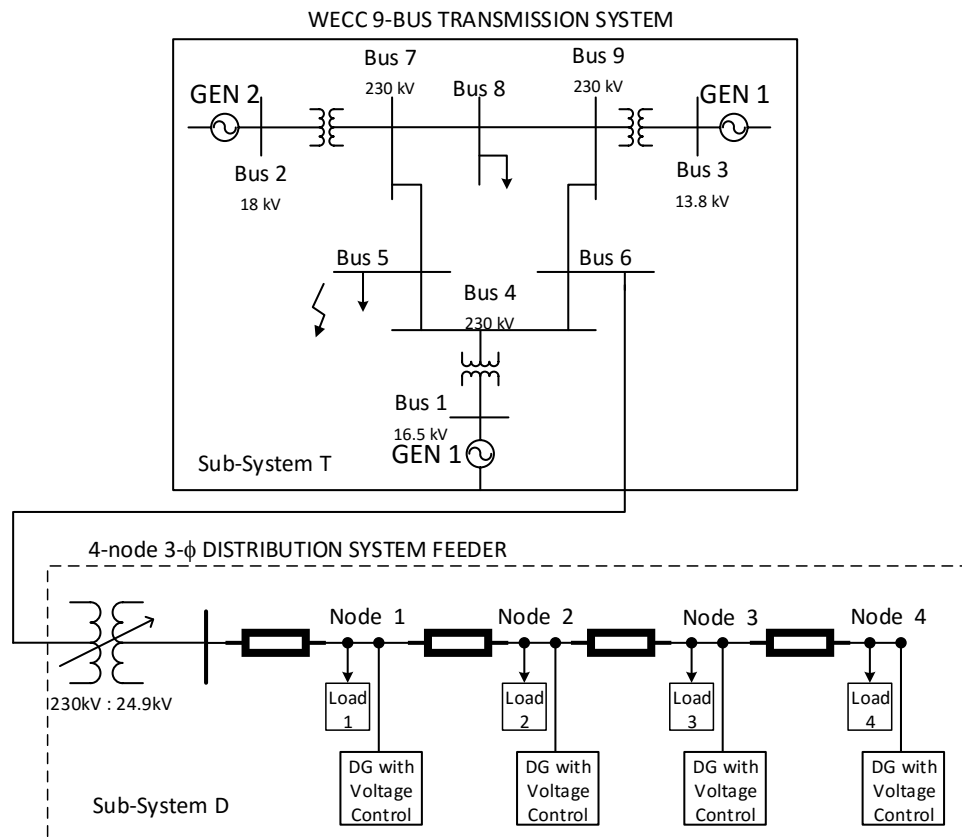
Figure 4.8 Voltage Control using DG on a 4-node distribution system connected to Bus 6 of WECC 9-bus Transmission System

4.3.2   Simulation Results

The above system is now simulated in the following ways. IN all cases the dynamic event is a reference change in the active power in DG inverters from 100 % to 50 %.

1. Setup 1: CoTDS simulation without distribution side voltage control by the DG inverter.

2. Setup 2: Only distribution system simulation with source voltage fixed to 1.0 p.u. and enabling voltage control by the DG inverters on the distribution side node voltages.

3. Setup 3: CoTDS simulation with source voltage fixed to 1.0 p.u. and enabling voltage control by the DG inverters on the distribution side node voltages, with $K_{iq} = 50$.

4. Setup 4: CoTDS simulation with source voltage fixed to 1.0 p.u. and enabling voltage control by the DG inverters on the distribution side node voltages, with $K_{iq} = 1000$.

The simulation results of Setup 1 are shown in Fig. 4.9. It can be observed that the distribution system node voltages are dropping from their steady state voltages to lower levels and since they are left uncontrolled, they remain low and do not recover.

In Fig. 4.10, the distribution system source voltage is kept fixed at 1.0 p.u. and therefore the observed dynamics in Setup 2 are only based on the distribution system dynamics without interaction with the transmission system dynamics. However, the voltage control is active and so the injected reactive power dynamically adjusts to regulate the voltage (with Q-V droop).

In Setup 3, when CoTDS simulation is performed to take into account the dynamics of the transmission system, distribution system and the voltage control dynamics, the response is quite different from that of the Setup 1 and Setup 2 as shown in Fig. 4.11 for $K_{iq} = 50$. This is the actual response and so it is quite useful in providing further insight into the system dynamic performance. Fig 4.12 shows the same simulation for $K_{iq} = 1000$ and shows that the response can become very oscillatory
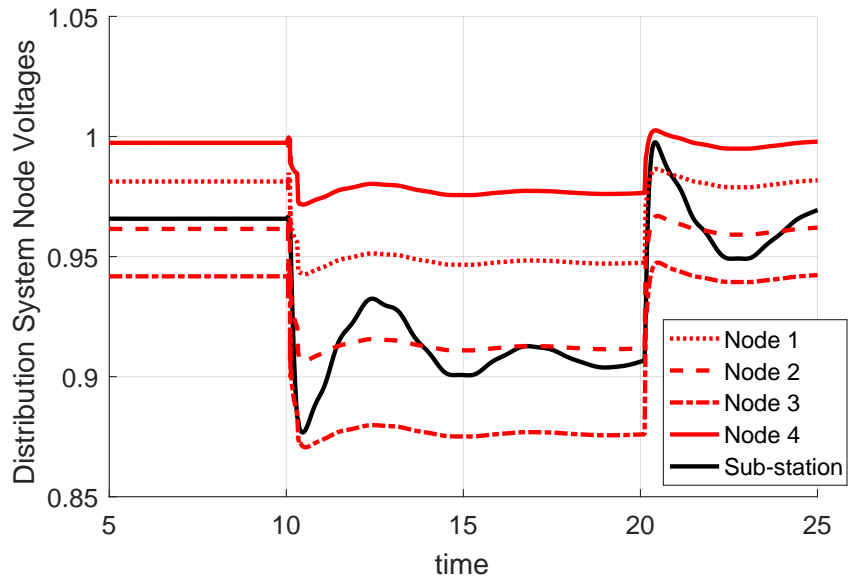
(a)
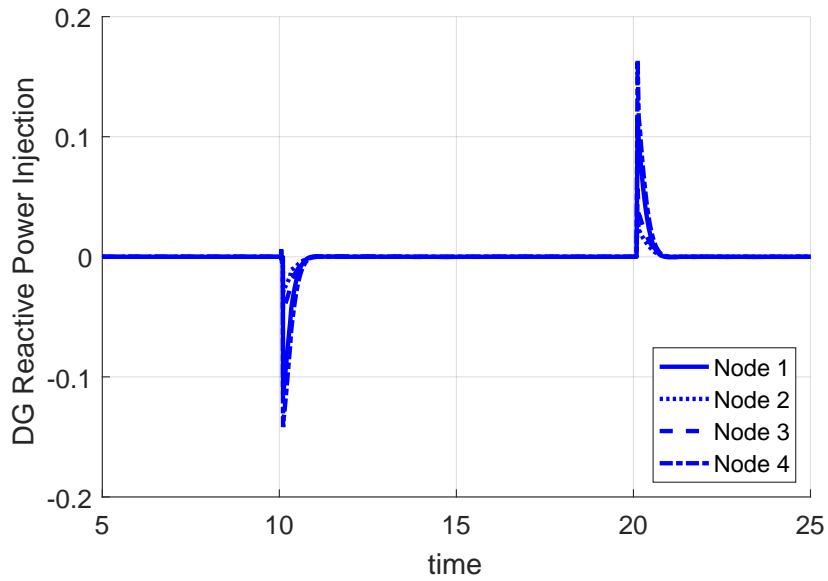
(b)

Figure 4.9   Dynamics of the node voltage for dynamic changes in reference active power without any voltage control (a) Sub-station voltage and the distribution system node voltages (b) Injected Reactive Power from DG inverters.
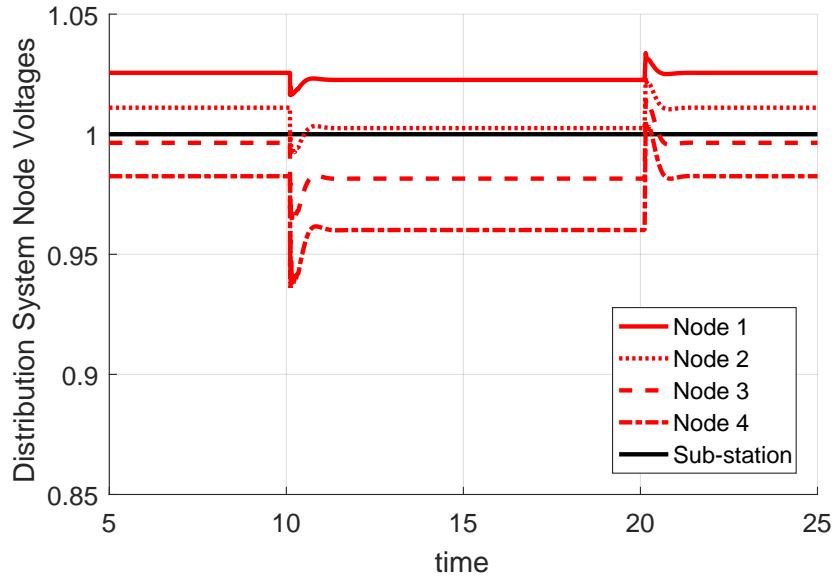
(a)
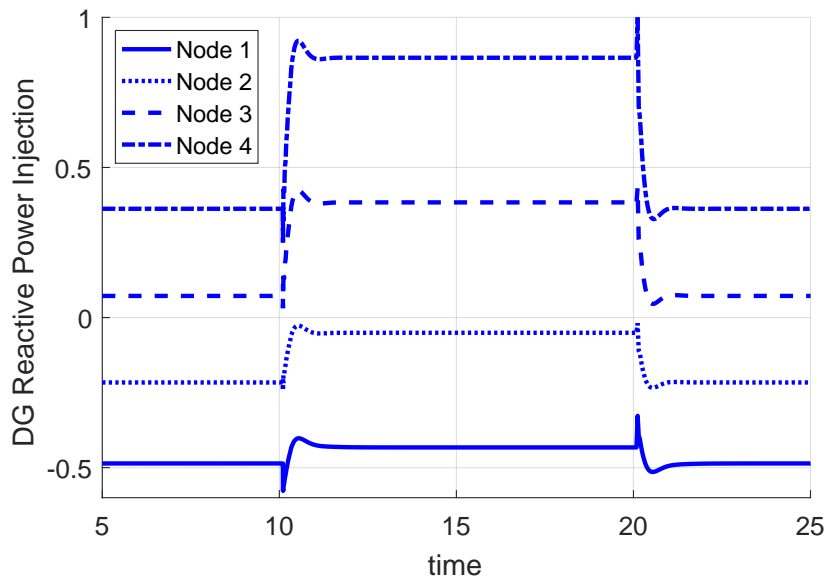
(b)

Figure 4.10   Dynamics of the node voltage for dynamic changes in reference active power
with voltage control keeping the distribution system source voltage at 1.0p.u.
(No CoTDS) (a) Sub-station voltage and the distribution system node voltages
(b) Injected Reactive Power from DG inverters.
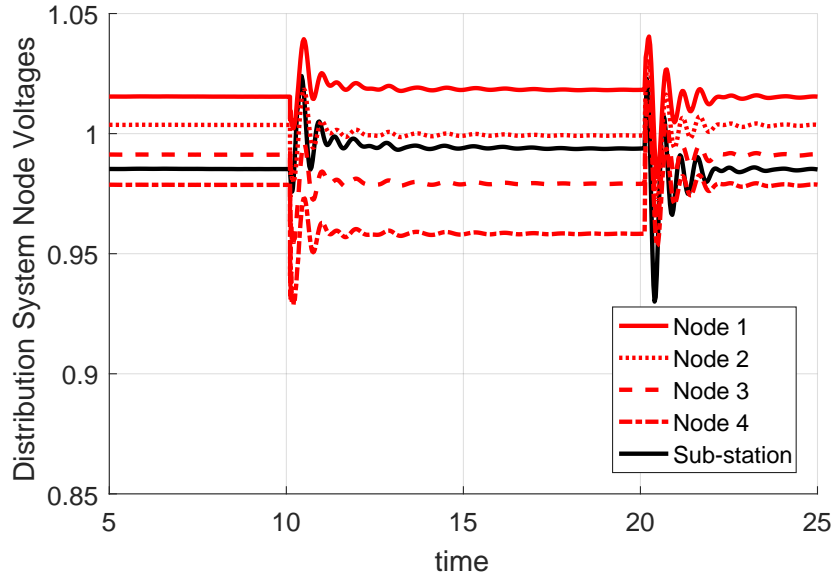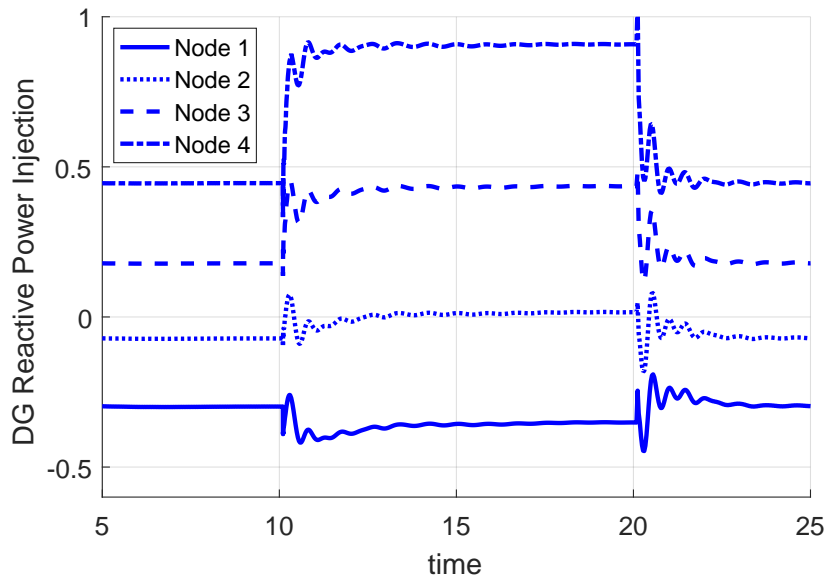
Figure 4.11 Dynamics of the node voltage for dynamic changes in reference active power with voltage control using CoTDS simulation (a) Sub-station voltage and the distribution system node voltages (b) Injected Reactive Power from DG inverters with $K_{iq} = 50$.
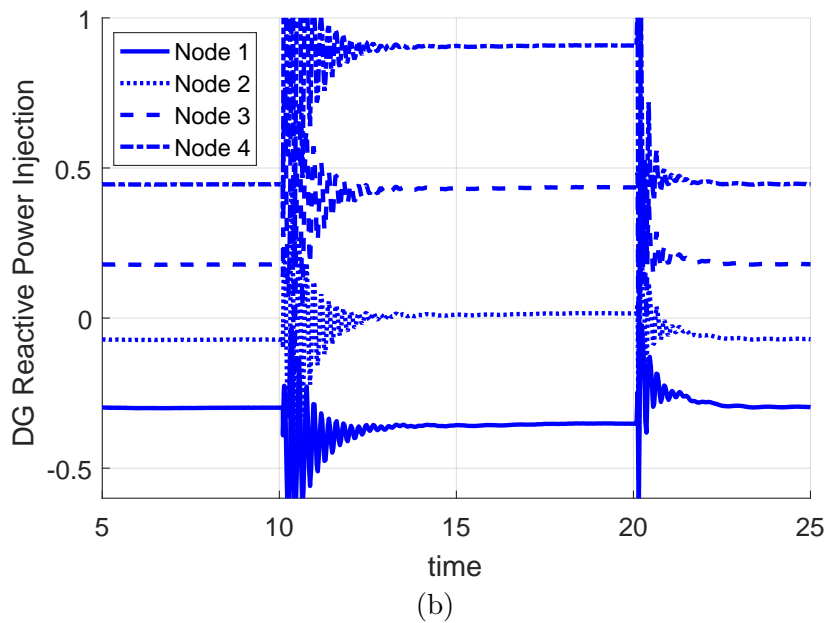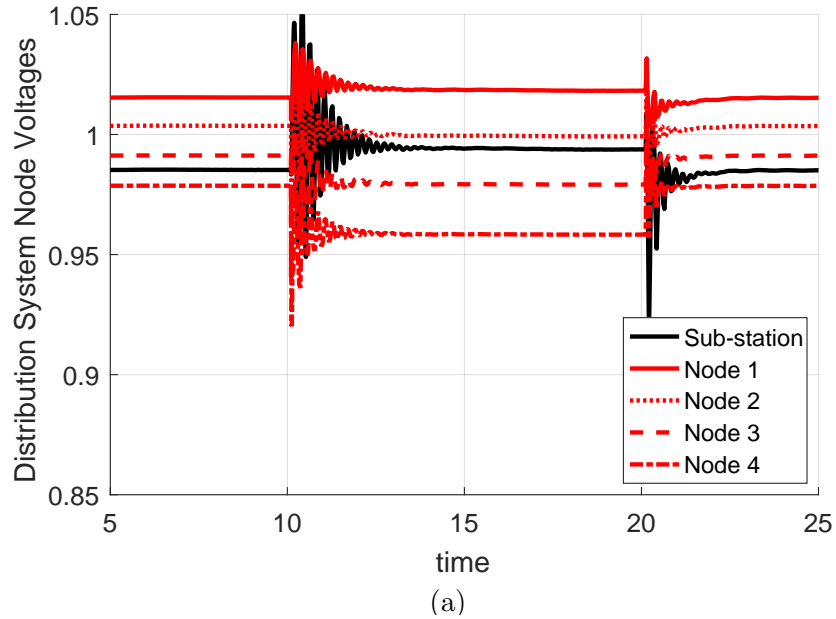
Figure 4.12   Dynamics of the node voltage for dynamic changes in reference active power with voltage control using CoTDS simulation (a) Sub-station voltage and the distribution system node voltages (b) Injected Reactive Power from DG inverters with $K_{iq} = 1000$.

4.4   Conclusions

In this chapter, the distribution side voltage control using DG inverter reactive power is modeled with the addition of voltage control loop to generate the commanded reactive power, Q_{cmd}. The dynamics of droop control are also modeled to include the $Q - V$ droop associated with the DG inverters.

The voltage control using the developed detailed DG inverter model is further validated against Simscape sine-wave simulation. It is shown that the same system simulation when simulated totally in one simulation tool, requires very small time step to avoid numerical problems. However, when CoTDS co-simulation is performed, even a nominal time step is sufficient to produce solutions without exhibiting any numerical problems. Thereby, the need and effectiveness of the CoTDS co-simulation is again demonstrated.

CHAPTER 5.   MODEL REDUCTION OF DISTRIBUTION SYSTEMS I: AGGREGATED WECC COMPOSITE LOAD MODEL

5.1   The WECC aggregated Composite Load Model (CLM)

Historically, dynamic load modeling in power systems has evoked very high attention from transient, long term, and small-signal stability studies. In [32], a variety of load models that can be used for performing transient studies is presented. Induction motors consume a significant portion of the total load power [33, 34] and hence their behavior has critical impacts on the power system dynamics. In combination with static ZIP load components it forms the substation load model that is both simple and commonly used. An aggregated induction motor model is summarized in [33]. Studies using such aggregated load modeling and parameter estimation using measurement data has been presented in [35, 36, 37, 38, 39]. In [40], a probabilistic model of the load with many induction motors is presented to study the cascading stall of a power system.

When an induction motor stalls following a severe disturbance, it can draw 5 to 8 times its normal reactive power requirement [41] which may delay the voltage recovery and may lead to tripping of loads and rapid collapse of an area power system [42]. This phenomenon is the cause of the Fault Induced Delayed Voltage Recovery (FIDVR) and therefore, it is very important to study the dynamics, using a model that includes not only a dynamic model based on the induction motor state variables, but also its stalling, tripping and reconnecting characteristics which can vary from the type and size of the motors.

Considering the significant impact of induction motor dynamics, Western Electricity Co-ordinating Council (WECC) load modeling task force included equivalent induction motors

along with the trip and reconnect characteristics to the existing ZIP load models. Single-phase air conditioner (A/C) model with stalling characteristics has also been added to this aggregated model and is known as the Composite Load Model (CLM).

The WECC CLM shown in Fig. 5.1 is discussed in detail in [43, 44]. The load types are classified under 3 main categories: static load, induction motor load and electronic load. static load is represented by load that is exponentially dependent on the load bus voltage. Typically, these exponents corresponds to the conventional ZIP model. Induction motors are further classified into 3 types of 3-phase induction motors (A, B, C) depending upon their application and one single-phase induction motor (D) which represents the motors used in A/C compressors. The lumped feeder impedance and the feeder shunt compensation are represented by R_f, X_f and B_f respectively.

A great challenge lies in tuning this CLM represented by 132 parameters. Since in reality, there are numerous individual loads of various types, it is a very complex task to determine the parameters of such a load model and ascertain the dynamic performance of the system under study [45]. In [46, 47], the challenges of the sensitivities in model parameter estimation is discussed. Due to the lack of a systematic approach to determine the parameter values, most often only generic values are used for the parameters.
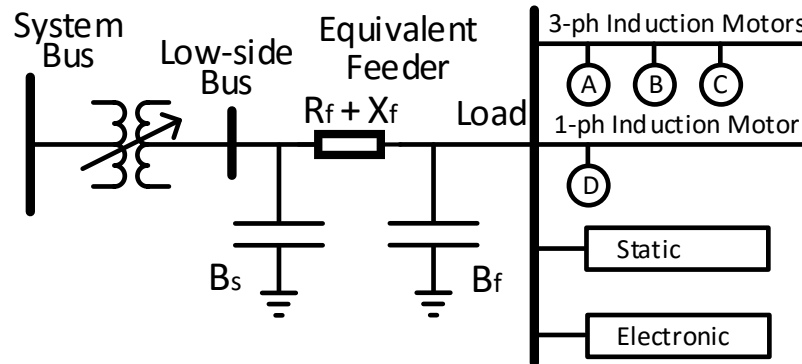
Figure 5.1   The WECC aggregated Composite Load Model (CLM)

5.2 CoTDS co-simulation based Distributed Load Model

In contrast to the aggregated CLM which consists of one big motor of each type, the distributed load model comprises of numerous actual real size motors. In the CLM, if there is an under-voltage trip or a thermal trip, either a fraction is considered as tripped (in case of three-phase induction motors) or the entire motor trips (in case of single-phase induction motors). If a fraction trips, then the CLM assumes a part of the motor load is dropped and so the motor operates at a different operating point on the Torque-Speed curve. And when a fraction reconnects, the load is correspondingly increased.

The CoTDS co-simulation based distributed load model shown in Fig. 5.2 on the other hand captures the behaviour of motors actually tripping and reconnecting to start from zero or very low speed.

Table 5.1   Key differences between aggregated CLM and the Distributed Load Model.

	Aggregated CLM	Distributed Load Model
Load	Aggregated at one node	Distributed across the feeder
No. of IMs	One of each type	Numerous
No. of fractions of 3-ϕ IM	Two of each type	Flexible
No. of fractions of 1-ϕ IM	One	Flexible
Under-voltage trip of 3-ϕ IM	Fraction of load drops and speed increases.	Fraction of motors disconnect and speed drops
Reconnection of 3-ϕ IM	Fraction of load increases and speed drops	Motors reconnect and their speed increases
Stalling of 1-ϕ IM	Entire motor stalls	Only fraction of motors stall
Behaviour capture	Average	Detailed
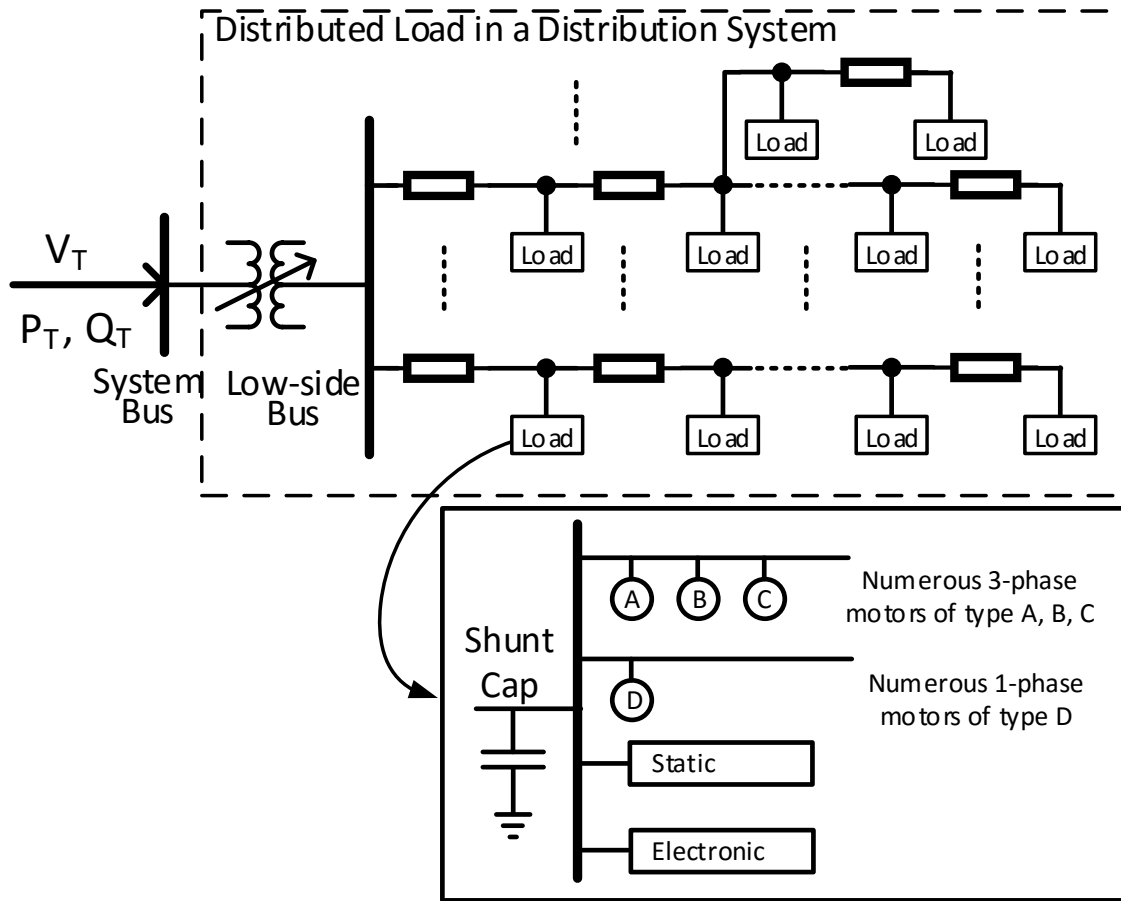
Figure 5.2   The Distributed Load Model

5.3 Determination of CLM Parameter values of a Distribution System

All the parameters of the CLM as provided by WECC load modeling are important for conducting transient studies. Many of the parameters need to be changed from their default value in accordance to the load system under study. The individual fraction of each of the load types determines the overall composition of the load and plays a vital role in the dynamic behavior. The equivalent feeder impedance significantly influences the voltage dip and duration of recovery. Fig. 5.3(a) shows the effect of different fractions (FmD) of the single-phase A/C motor load and Fig. 5.3(b) shows the effect of variation in the equivalent feeder impedance on the delayed voltage recovery.
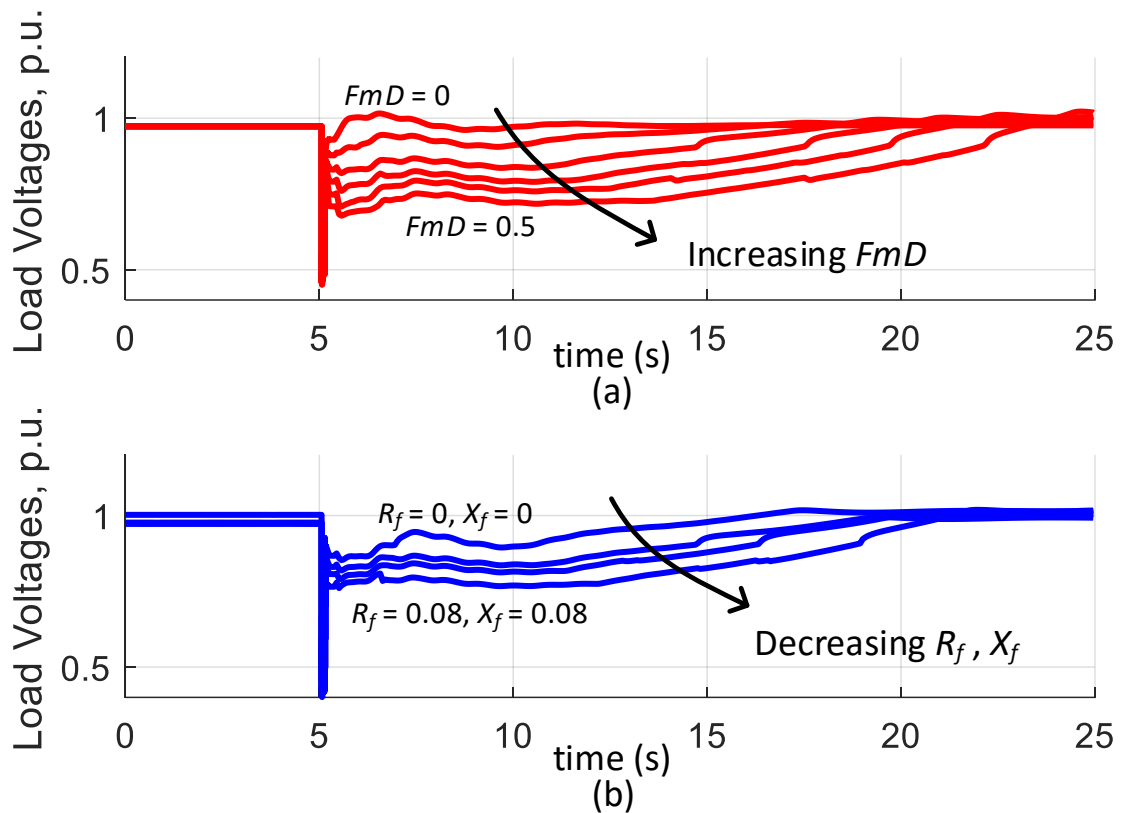
Figure 5.3 Effect of variation in (a) load fraction, FmD and   (b) feeder impedance parameters: R_f, X_f.

Therefore in this study, the parameters of load fractions, FmA, FmB, FmC, FmD, Fel and the equivalent feeder impedance, $R_f + jX_f$ are identified as those which needs to be calculated to equivalently represent the distribution system as shown in Fig. 5.4.
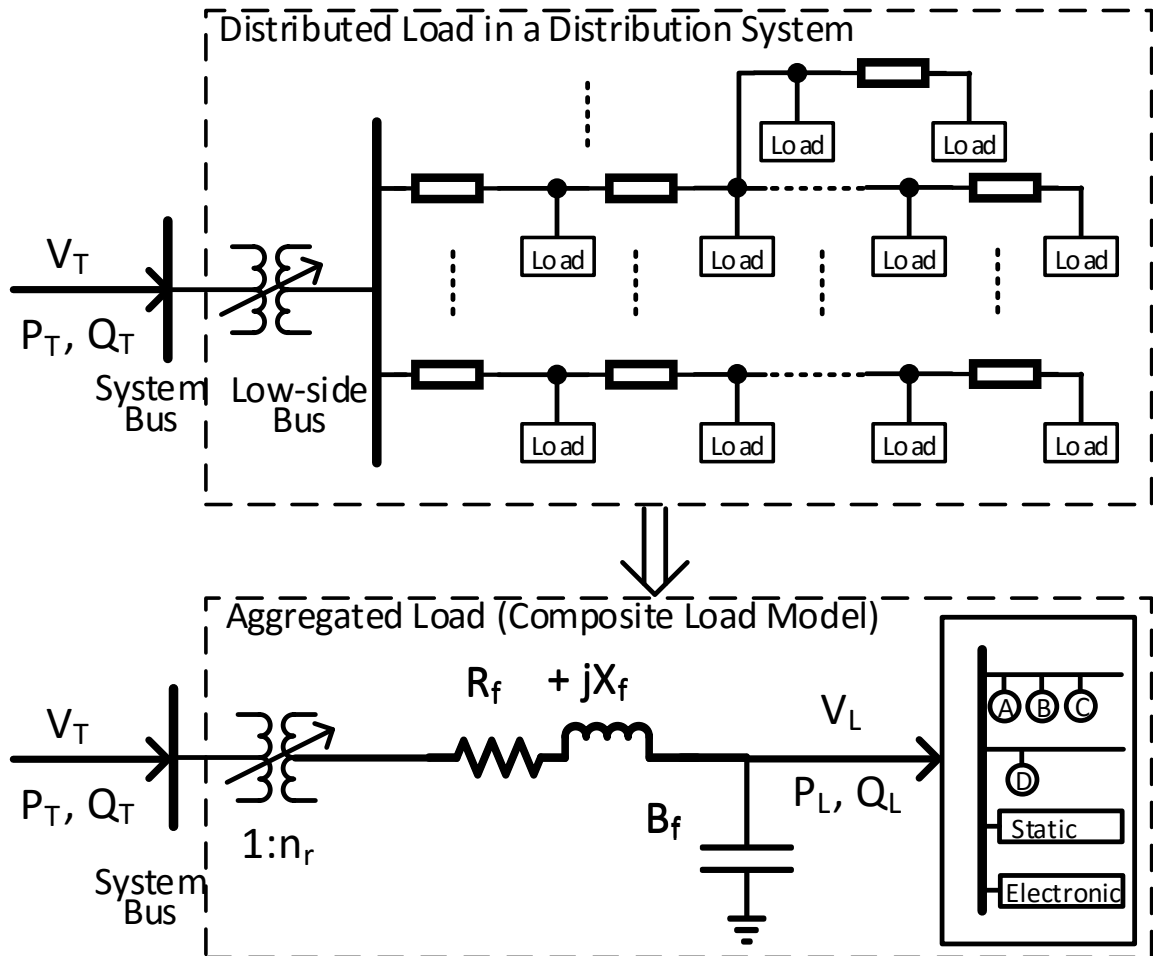
Figure 5.4   CLM representation of the distribution system.

The procedure for determining these identified parameters is now described. First, the CoTDS co-simulation is run until a steady state is reached. The interface variables provide the values for the transmission system bus voltage, V_T and the distribution system source power P_T, Q_T. The load at node, n is given by (p_n, q_n) for a total of N nodes in the

distribution system. The distribution system power flow gives the node voltages at all the load nodes V_n for $n = 1$ to N. The sum total of the entire load power given by the terms, P_L and Q_L, is determined by equation (5.1).

$$P_L = \sum_{n=1}^{N} p_n \quad Q_L = \sum_{n=1}^{N} q_n \tag{5.1}$$

The load on each of the distribution system nodes is classified into the load types similar to the CLM, i.e., static, electronic, 3-phase induction motors (Type A, B and C) and single phase A/C motor load (Type D). It is assumed that the fraction of load for each type given by f_n^S, f_n^E, f_n^A, f_n^B, f_n^C, f_n^D is known on each node and their sum totals to 1.

$$f_n^S + f_n^E + f_n^A + f_n^B + f_n^C + f_n^D = 1 \tag{5.2}$$

5.3.1   Calculation of Load Fractions of the CLM

The load fraction for each individual load type is determined as a ratio of the total load of a type divided by the total load of all types across all the nodes. This leads to the parameters for the induction motor load fractions, FmA, FmB, FmC, FmD and the electronic load fraction, Fel is given by

$$
\begin{aligned}
FmA &= \frac{\left(\sum_{n=1}^{N} f_n^A \cdot p_n\right)}{P_L} \\
FmB &= \frac{\left(\sum_{n=1}^{N} f_n^B \cdot p_n\right)}{P_L} \\
FmC &= \frac{\left(\sum_{n=1}^{N} f_n^C \cdot p_n\right)}{P_L} \\
FmD &= \frac{\left(\sum_{n=1}^{N} f_n^D \cdot p_n\right)}{P_L} \\
Fel &= \frac{\left(\sum_{n=1}^{N} f_n^E \cdot p_n\right)}{P_L}
\end{aligned}
\tag{5.3}
$$

5.3.2 Calculation of Equivalent Feeder Impedance

The relationship between the power, P_T, Q_T and P_L, Q_L is obtained by modifying the conventional DistFlow [48] equations (5.4) and setting $W_T = (P_T^2 + Q_T^2)/(n_r^2.V_T^2)$.

$$P_L = P_T - R_f.W_T$$
$$Q_L = Q_T - X_f.W_T + B_f.V_L^2 \tag{5.4}$$
$$V_L^2 = n_r^2.V_T^2 - 2(R_f.P_T + X_f.Q_T) + (R_f^2 + X_f^2).W_T$$

Here, P_T, Q_T, V_T, P_L, Q_L are known from CoTDS co-simulation. However, V_L is not known as we only know the each individual node voltages. In the CLM, V_L is a representative of the node voltages of the distribution system. In order to make an appropriate correspondence, the V_L is evaluated in equation (5.4) using a weighted averaging of node voltage over all the nodes based on the load power at each node.

$$V_L = (\sum_{n=1}^{N} p_n.V_n)/P_L \tag{5.5}$$

We are now left with 4 unknowns, namely, R_f, X_f, B_f and n_r and only 3 equations. But since we know the distribution network, the ratio of R_f to X_f can be set to a specific value for solving the equivalent feeder impedance parameters.

5.4 Simulation Case Studies

The CoTDS dynamic simulation is setup with a test case as shown in Fig.5.5 using a WECC 9-bus transmission system interfaced at Bus 6 with a distribution system feeder comprising of 40 sub-systems. The total load on each sub-system is 2.5MW, 0.75MVar.
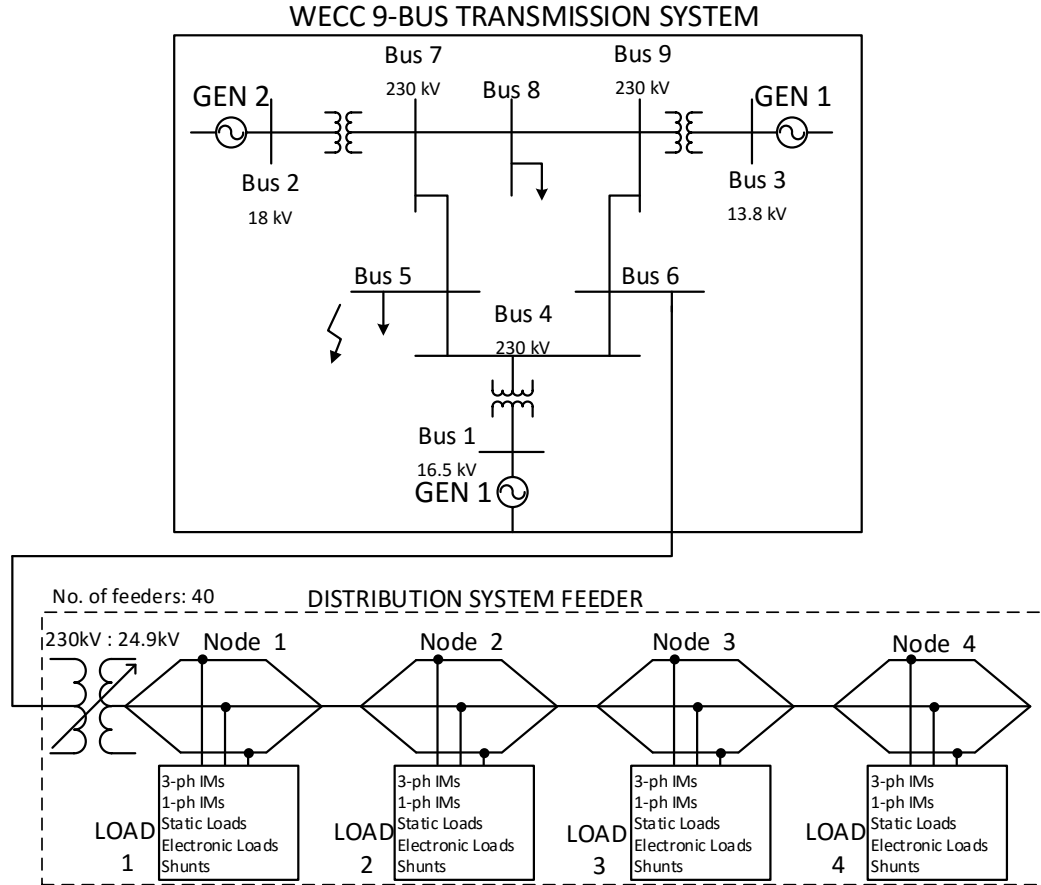
Figure 5.5   WECC 9-bus system and 40 sub-systems of a 4-node distribution system feeder.

5.4.1   FIDVR behavior using distributed load model and aggregated CLM.

The objective is to study the FIDVR behavior using the distributed load model and compare with the conventional aggregated CLM. In this study, the distribution system load in each of the nodes consist of load fractions, $f_n^S = 0.1$, $f_n^E = 0.1$, $f_n^A = 0.2$, $f_n^B = 0.1$, $f_n^C = 0.1$, $f_n^D = 0.4$. The system is subjected to a 3-phase to GND fault for $83ms$ (5 cycles) on

Bus 5 of the transmission system. This leads to an FIDVR phenomenon due to the stalling of the single-phase A/C motors.
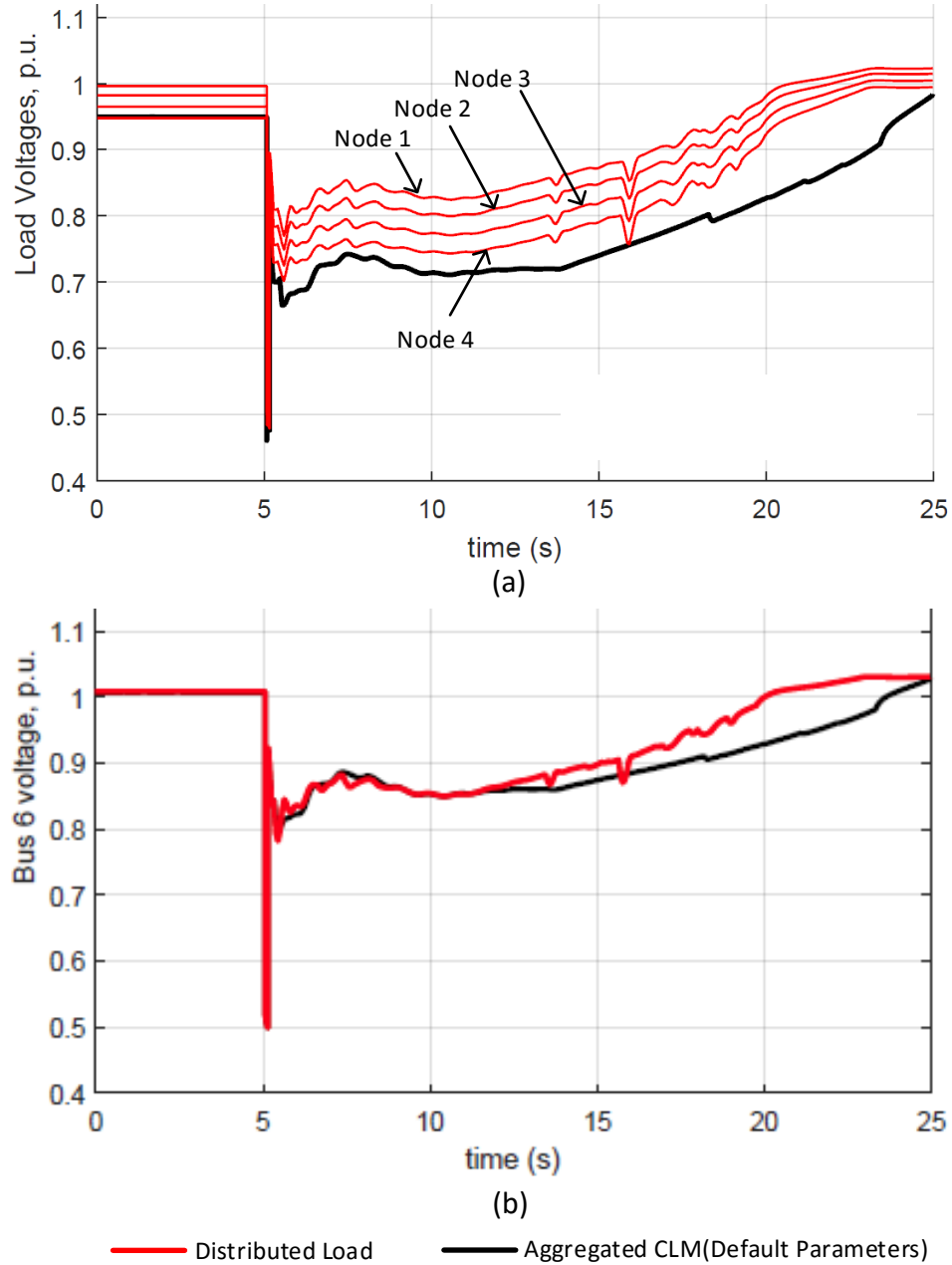
Figure 5.6 (a) Load bus voltage evolution of CLM at Bus 6 using CLM and node voltages of distribution system at Bus 6 using distributed load model. (b) Corresponding System bus voltages

Fig. 5.6(a) shows the evolution of the distribution system node voltages during the delayed voltage recovery using the distributed load model. These plots are compared to the load bus voltage obtained by setting nominal load fractions of $FmA = 0.2$, $FmB = 0.1$, $FmC = 0.1$, $FmD = 0.4$ and $Fel = 0.1$. The feeder impedance is kept at the default value of $Rf = 0.04$ and $Xf = 0.04$. The following inferences can be made by observing these voltage recovery plots.

The load bus plot using the default parameters is not representing the average plot of the distribution system node voltages and hence the recovery time is also not the same. This is due to the fact that the default equivalent feeder impedance is larger that of the distribution system and so the load voltage is lower to begin with. This causes the stall power in the single-phase A/C motor to be lower and therefore the thermal tripping is slower which in turn causes the longer recovery time.

The distribution system node voltages in Fig. 5.6(a) with the distributed load model show sharp dips whereas the equivalent load voltage with the CLM is smoothly recovering. This shows that the distributed load model is capturing particular behaviour that is not seen using the CLM. Upon further examination of the distributed load model results, the 3-ϕ induction motors that trip during the fault due to U/V, drop their speed. During the reconnection, when the voltages in each of node rise above the reconnection threshold, the motors are starting from zero (or very low) speed as these are modeled as individual motors. In the case of CLM, only a fraction of the load of each type of motor is tripped and reconnected, and the speed change is minimal. The speed change during tripping and reconnecting for the distributed load model and the CLM are shown in Fig. 5.7(a).

This behavior is also demonstrated by comparing the reactive power consumption during this transient event. Fig. 5.7(b) shows that, in the distributed load model, when the motors reconnect and the speed is increasing, the reactive power shows the expected transient peaks before settling down. This causes the voltage dips at the corresponding nodes in the distribution system. However, when using the CLM, the reactive power do not show these
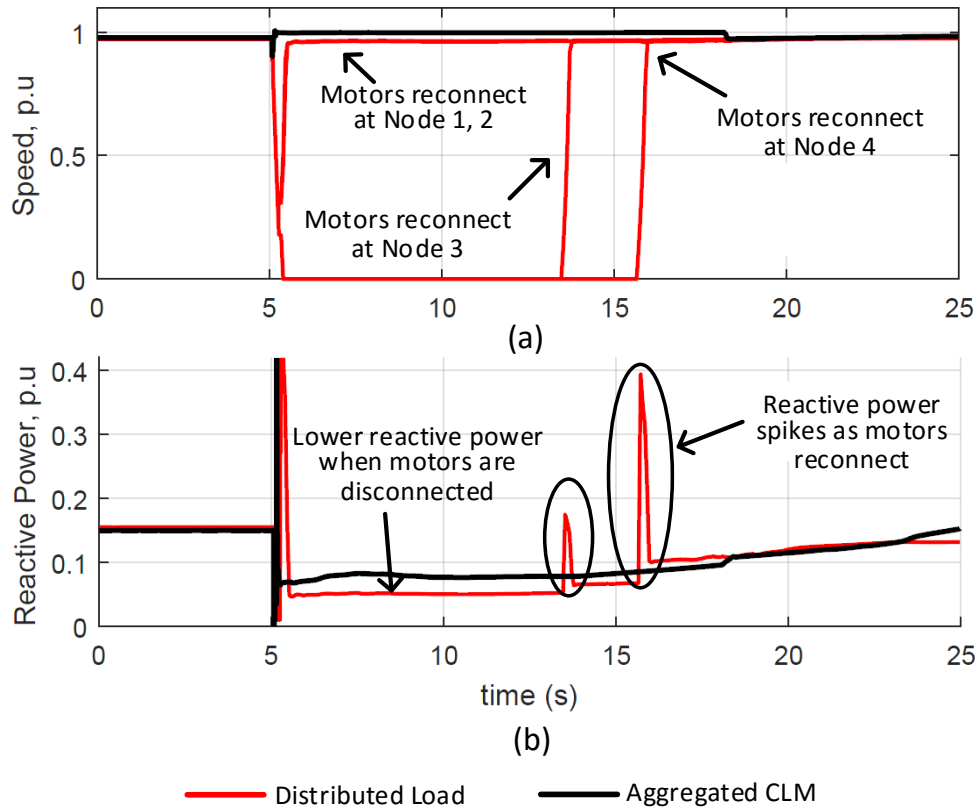
Figure 5.7   (a) Speed changes in induction motor, type A, in distributed load model compared to that of CLM. (b) Total reactive power of induction motor, type A in distributed load model and CLM.

peaks as there is no significant change in the induction motor speed. Consequently, the voltage dips are not captured in the CLM.

5.4.2   Effect of Distribution System Load Composition on CLM parameters

From the results in the previous section, it is evident that the equivalent feeder impedance has to be tuned for the aggregated CLM to properly represent the distribution system. As the load composition and configuration of the distribution system play a vital role in determining the equivalent feeder impedance parameters, in this section different load composition and configurations are considered for the comparative study.

The feeders are composed of a mix of residential, commercial and industrial type. The fraction of individual load types depends upon the feeder type and is shown in Table 5.2 [49]. The load fractions of the entire distribution system depends upon the feeder composition. In this study, 3 cases of different feeder compositions are chosen as shown in Table 5.3 along with the respective load fractions. These cases are combined with 4 load location configurations with load at each node given as a percentage of the total sub-system load as shown in Table 5.4 leading to a total of 12 test cases. The load composition and the configuration are used to determine the corresponding load fractions at each node.

Table 5.2   Load fraction in each type of feeder

Feeder Type	IM-A	IM-B	IM-C	IM-D	Elec.	Static
Residential (R)	0.01	0.04	0.02	0.40	0.13	0.40
Commercial (C)	0.17	0.14	0.12	0.00	0.14	0.43
Industrial (I)	0.21	0.32	0.25	0.00	0.15	0.07

Table 5.3   Load fraction in each composition

Composition (%)	IM-A	IM-B	IM-C	IM-D	Elec.	Static
R:30, C:40, I:30	0.13	0.16	0.13	0.12	0.14	0.32
R:50, C:30, I:20	0.10	0.13	0.10	0.20	0.13	0.34
R:70, C:20, I:10	0.06	0.10	0.06	0.28	0.13	0.37

Table 5.4   Load location configurations

Configuration	Load 1 %	Load 2 %	Load 3 %	Load 4 %
Config. 1	100	0	0	0
Config. 2	50	25	25	0
Config. 3	25	25	25	25
Config. 4	0	0	0	100

Similar to the Section 5.4.1, in each of the test cases, in each test case, the system is subjected to a 3-phase to GND fault for 83ms (5 cycles) on Bus 5 of the transmission system which leads to FIDVR behaviour. This behavior is then studied using (i) the distributed load model which includes the complete detailed behaviour of the loads in the distribution

system, (ii) the CLM using the default parameter values and (iii) the CLM using the calculated parameter values using the procedure described in Section 5.3.

The default feeder impedance in the WECC CLM is 4% resistance and 4% reactance. However, depending upon the load location and the distribution network impedances, the actual calculated equivalent feeder impedance can vary from about 25% to 200% of the default values and this can lead to significant differences in the recovery behaviour. Table 5.5 gives the calculated equivalent feeder impedance according to Section 5.3.2.

Table 5.5   Calculated Equivalent Feeder Impedance

Feeder Composition	Location Configuration	Calculated Equivalent Feeder Impedance (pu)
Composition (a) Residential 30% Commercial 40% Industrial 30%	Config. 1 Config. 2 Config. 3 Config. 4	0.010 + j0.005 0.016 + j0.008 0.029 + j0.015 0.090 + j0.045
Composition (b) Residential 50% Commercial 30% Industrial 20%	Config. 1 Config. 2 Config. 3 Config. 4	0.010 + j0.005 0.016 + j0.008 0.029 + j0.015 0.090 + j0.045
Composition (c) Residential 70% Commercial 20% Industrial 10%	Config. 1 Config. 2 Config. 3 Config. 4	0.010 + j0.005 0.016 + j0.008 0.029 + j0.015 0.090 + j0.045

Feeder Composition (a)

Feeder Composition (b)
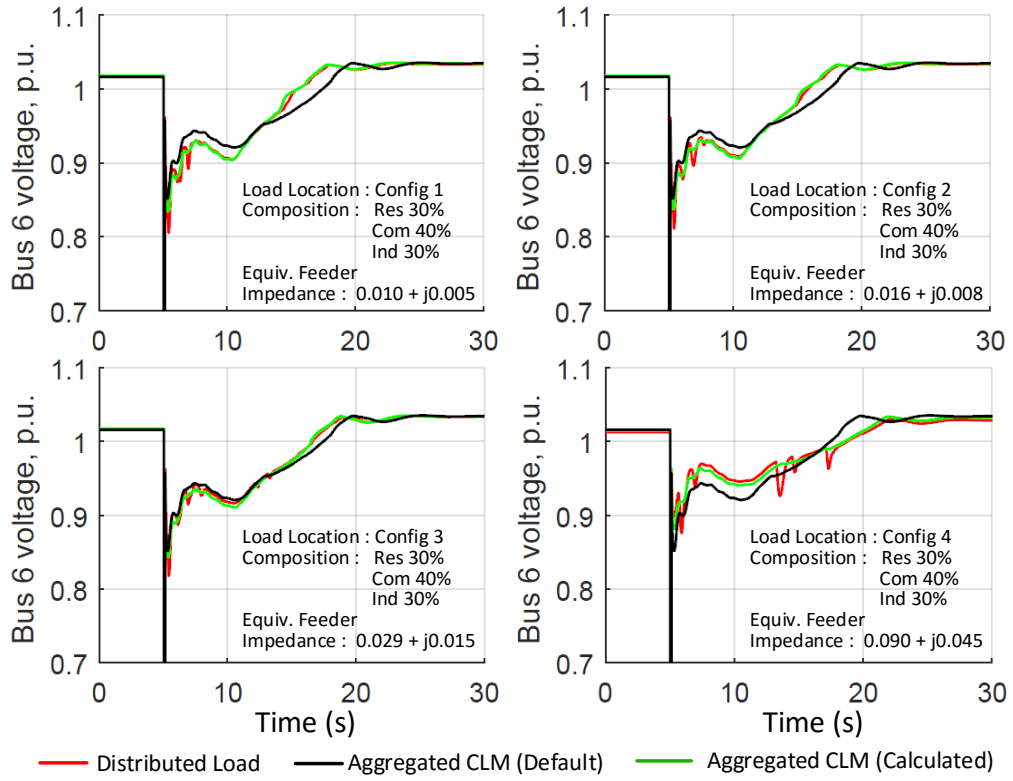
Feeder Composition (c)
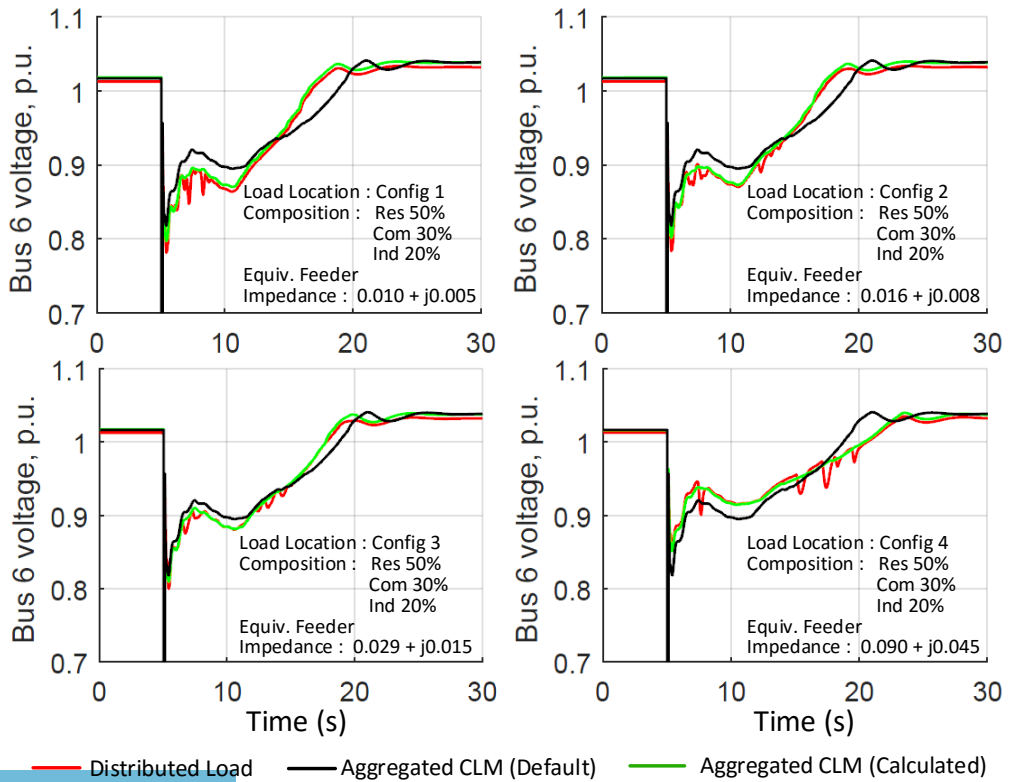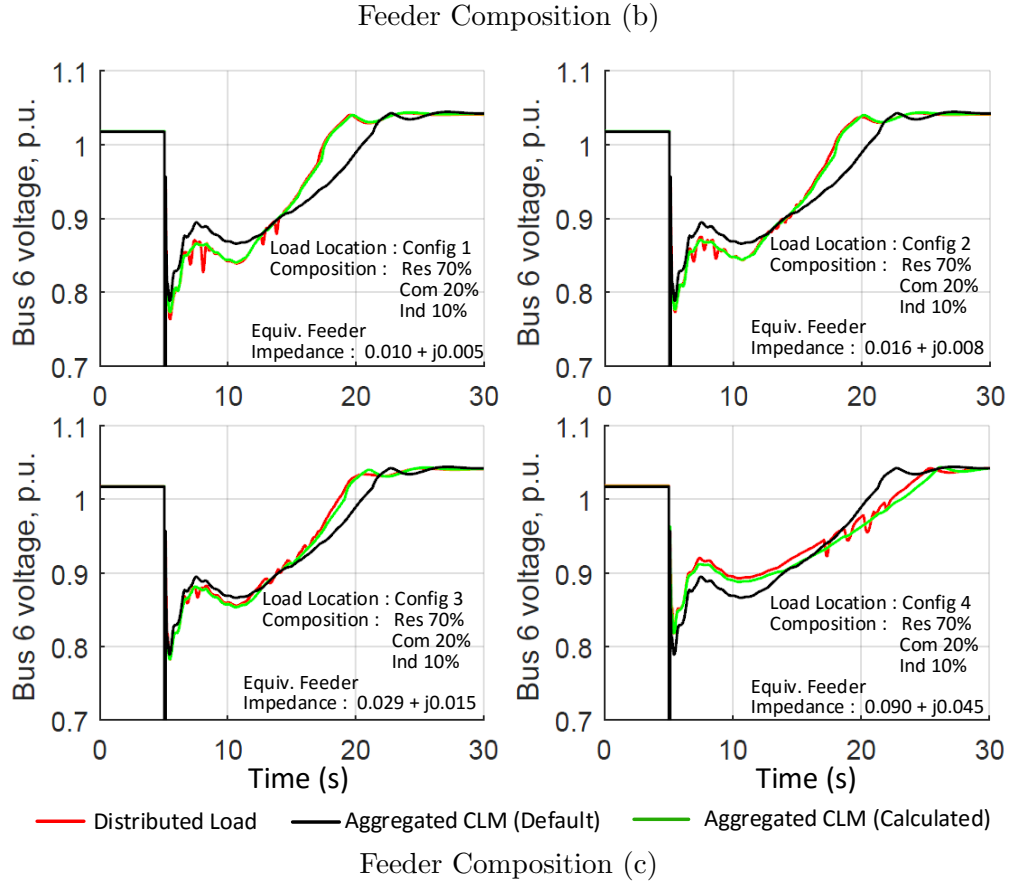
Figure 5.8 FIDVR results using (i) distributed load model, (ii) aggregated CLM with default equivalent feeder impedance, $0.04 + j0.04$ and (iii) aggregated CLM with calculated equivalent feeder impedance for the three different feeder compositions (a), (b) and (c).

5.4.3 Note on T_{stall} parameter sensitivity in the aggregated CLM.

The entire FIDVR phenomenon heavily depends upon the stalling characteristics of the single phase induction motor. In the CLM, these motors stall if the voltage goes below the specified stall voltage, V_{stall} for a time greater than stall time, T_{stall}. We consider a case where the fault duration is varied between 50ms to 70ms with the aggregated CLM parameter $T_{stall} = 60$ms. The corresponding parameter in the distributed load model is uniformly distributed amongst the motors between 50ms to 70ms.

The FIDVR phenomenon is now studied for the distributed load model and the corresponding aggregated CLM. Fig. 5.9 shows that in the case of the aggregated CLM, only extreme behavior is observed. If the fault duration is just less than the T_{stall} of the CLM, then the single phase induction motor does not go into stall mode and so the recovery is very quick after the fault is cleared. The critical FIDVR behaviour is completely missed. However if the fault duration is just more than the T_{stall} of the CLM, then the FIDVR phenomenon is observed very prominently. The behavior in the distributed load model shows that the recovery, besides being insensitive to the fault duration, is also truly representing the real case of a fraction of the motors stalling.

NOTE: This will be further addressed in the Reduced Distribution System Model (RDSM) of Chapter 6.
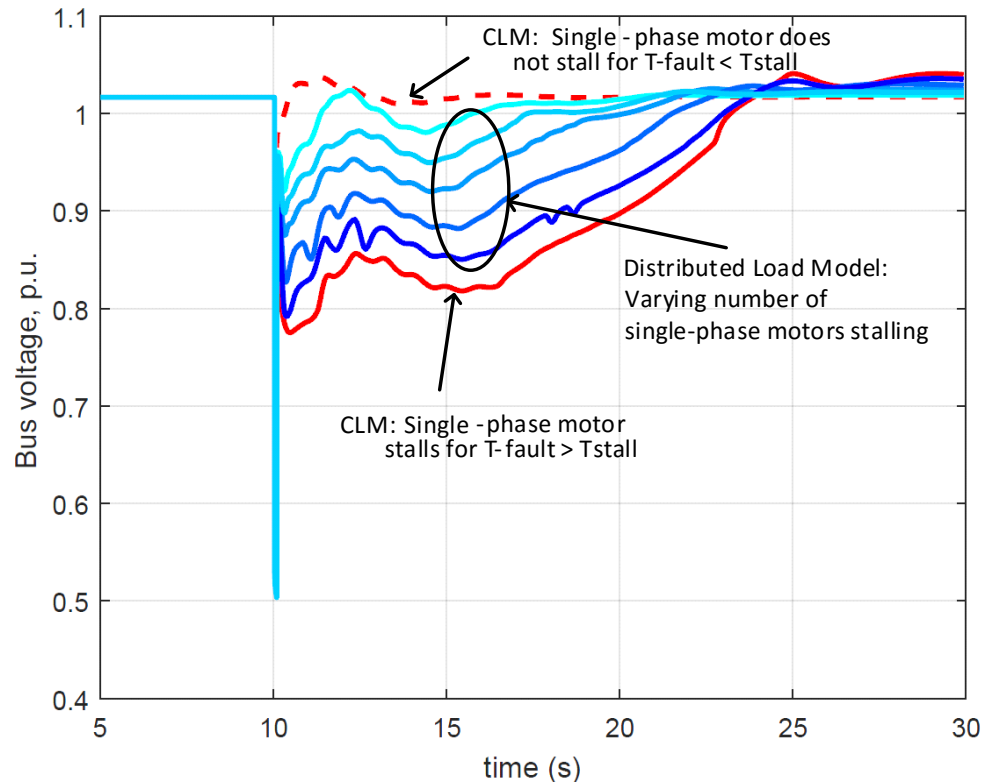
Figure 5.9   Effect of variation in fault time on FIDVR behavior in the distributed load model and corresponding aggregated CLM.

5.5   Conclusion

It can be clearly seen from Fig. 5.8 that in all the test cases, there is a considerable deviation of the recovery voltage using the aggregated CLM with the default parameters when compared to that of the distributed load model. However, when the calculated values for the CLM parameters are used, there is a close match between the results obtained from the aggregated CLM and that of the distributed model.

In this chapter, the CoTDS co-simulation methodology is applied to a distributed load model to represent the load dynamics of the entire distribution system. A procedure to determine the load fractions and the equivalent feeder impedance of the aggregated WECC CLM is detailed. The delayed voltage recovery behavior due to a fault on a transmission bus is compared between the distributed load model and the aggregated CLM with default parameter values. The comparison reveals that the distributed load model displays the actual detailed behavior and therefore serves as a guiding tool to tune the aggregated CLM parameters.

Several test cases with varying load compositions and configurations were considered to demonstrate the effectiveness of the proposed method to properly represent the distribution system in the CLM. In all the test cases, when calculated values of the CLM parameters are used, the dynamic behavior of the delayed voltage recovery is closer to the actual detailed behavior of the distributed load model. Therefore this method can is very useful for planning and reliability assessment.

CHAPTER 6.   MODEL REDUCTION OF DISTRIBUTION SYSTEMS II: REDUCED DISTRIBUTION SYSTEM MODEL

6.1   Background

Until recently, distribution systems have lacked high-quality real-time measurement data. There has been a compelling motivation for using advanced measurement data from accurate, high resolution devices in distribution networks [50]. High-precision micro phasor measurement units (μPMUs), when tailored to the particular requirements of power distribution, can support a range of monitoring, diagnostic and control applications [50]. They can also enable a new approach for managing distribution systems, particularly in the presence of significant renewable penetration [51] and can revel phenomenon that were not usually thought to occur in distribution systems. In fact, it was recently shown from PMU measurements that FIDVR occurred more frequently in distribution systems than transmission systems [52].

To control and mitigate FIDVR in distribution systems, (μPMUs) measurements can be used to provide sufficient visibility to identify and localize motor stalling in distribution systems. As FIDVR phenomenon is driven by the load dynamics, targeted load control in regions with large motor stalling will lead to a faster recovery. One of the challenges is that μPMU measurements at all the nodes in the system are used to estimate the matrix values of the optimization formulation in [53]. This is not practical and so a model that requires lesser number of measurements is necessary. The proposed Reduced Distribution System Model (RDSM) addresses this need with the added advantage of solving the optimization problem faster as the number of nodes are reduced from the original system.

6.2   Reduced Distribution System Modeling

6.2.1   Identification of Load Areas

Consider a radial distribution system shown in Fig. 6.1 with several nodes with each node comprising of static, electronic, motor loads (3-ϕ and 1-ϕAC motors) and DG inverters. Measurement devices such as μPMUs measure load voltage and power in the distribution lines/loads at sub-second intervals. The objective is to reduce the number of nodes and represent the load at each measurement node using an aggregated dynamic model that captures the overall dynamic behavior of the full model. The placement of μPMUs is a problem that is beyond the scope of this work. Here it is assumed that they are placed at nodes where secondary feeders and large loads are connected to the primary feeder.
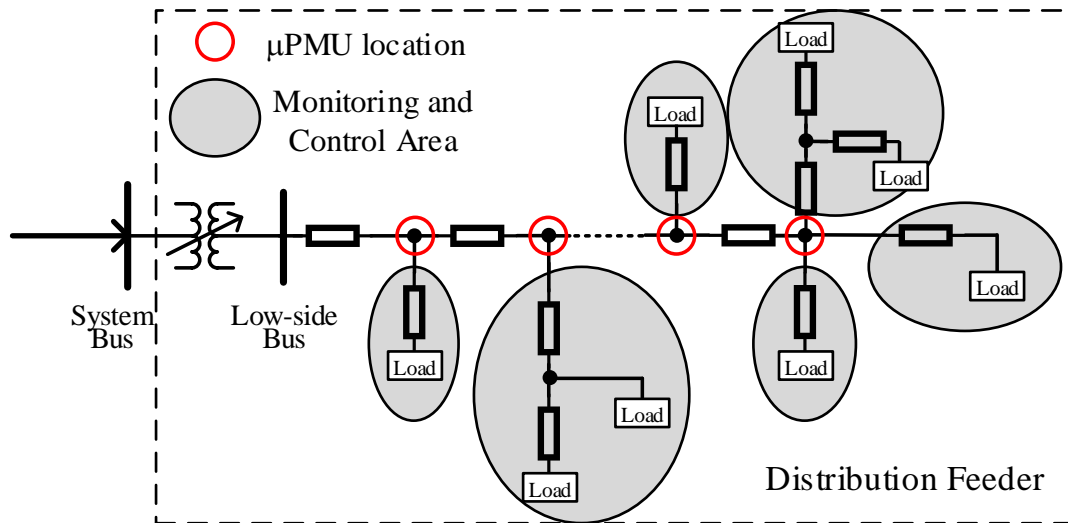
Figure 6.1   Radial distribution system with μPMUS installed in some nodes.

6.2.2   Sub-Models based on Load Areas

The proposed RDSM is made up of several sub-models connected in a structure similar to the original topology as shown in Fig. 6.2 (a). The sub-model is analogous to the CLM described previously with selected parameters to represent relevant portions of the DS with

an equivalent feeder impedance, a load tap changing transformer and a load block as shown in Fig. 6.2 (b). The load block includes static load, IM loads, and PV inverter. The static load parameters correspond to the conventional ZIP model. The electronic loads are absorbed into the constant power parameters of the ZIP load. The 3-ϕ IM (A, B, C type motors of the CLM) are lumped into one motor and the 1-ϕ IM (Type D of the CLM) represents the motors used in residential A/C compressors.

Table 6.1 shows the relevant parameters of the sub-model that would represent the portion of the DS network. Here, F_s, F_{m1}, F_{m3} are the fractions of the corresponding loads and F_{dg} is the fraction of the equivalent DG in that portion of the network. R_f, X_f, B_f and n_r are the parameters of the equivalent feeder impedance. The static load, the 3-ϕ IM and the 1-ϕ IM and DG inverter are represented by the parameters in the respective columns in Table 6.1 and these parameters are defined in the WECC CLM specifications [43].
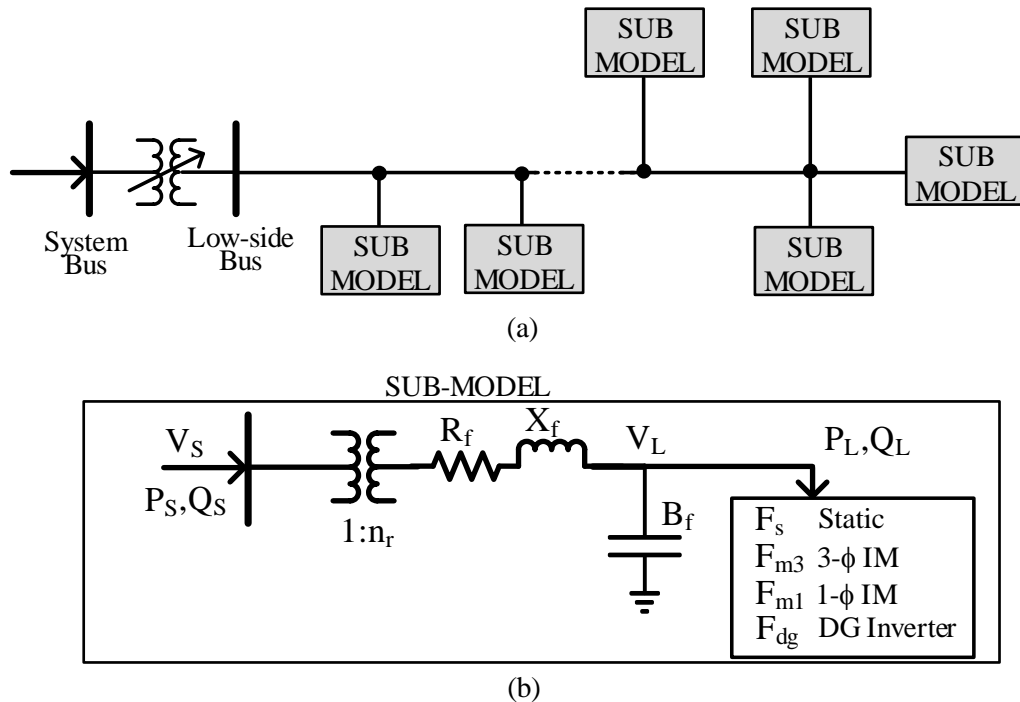
Figure 6.2 (a) Generic Reduced Distribution System Model (RDSM). (b) Sub-model.

Table 6.1   Parameters of the sub-model of Reduced Distribution System Model (RDSM)

Load Fraction	Equiv. Feeder	Static Load	3-ϕ Ind. Motor	1-ϕ Ind. Motor	DG
F_s	R_f	P_{z0}	R_s	V_{stall0}	F_{dg}
F_{m1}	X_f	Q_{z0}	X_{ls}	V_{stall}	
F_{m3}	B_f	P_{i0}	X_m	T_{stall0}	
	n_r	Q_{i0}	R_{r1}	T_{stall}	
		P_{p0}	X_{lr1}	R_{stall}	
		Q_{p0}	R_{r2}	X_{stall}	
		Q_{sh0}	X_{lr2}	T_{th}	
		H		θ_1	
				θ_2	

6.2.3   Modeling the stalling behavior of 1-ϕ (A/C) Induction Motor

As noted in Section 5.4.3, the entire FIDVR phenomenon heavily depends upon the stalling characteristics of the single phase induction motor. The limitation of the WECC CLM with respect to the T_{stall} parameter was shown in Fig. 5.9.

In the RDSM, this limitation is overcome by modeling the stalling behavior to accommodate the scenarios where only a fraction of the 1-ϕ motors have stalled and still yield a result where the results from the model can correspond to that of the data obtained using CoTDS co-simulation with the distribution system having a distributed values of the stall parameters.

In order to achieve this, the model must have a means to produce a voltage recovery behavior that can have any profile between 100% of 1-ϕ motors stalled and none of the motors stalled. This is done by defining a reference area, A_{ref} as defined by the original set of parameters V_{stall} and T_{stall} below a reference value given by a newly introduced parameters, V_{stall0} and T_{stall0}.

If the voltage, v_L falls below V_{stall0}, and stays below V_{stall0} for longer than T_{stall0}, then the following equation determines the fraction of motors stalling, $f_{stalling,i}$ in the ith time instant of simulation.

$$f_{stalling,i} = \frac{V_{stall0} - v_L}{V_{stall0} - V_{stall}} * \frac{t_i - t_{i-1}}{T_{stall} - T_{stall0}}$$

$$F_{stalled,i} = F_{stalled,i-1} + f_{stalling,i}$$

(6.1)

where, $F_{stalled,i}$ is the corresponding fraction of induction motors that is stalled at the ith time instant.
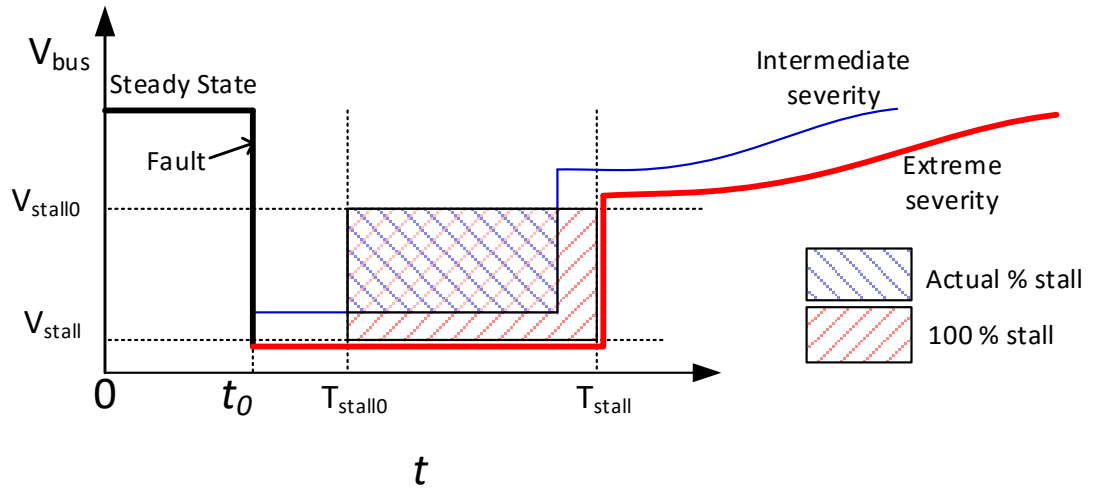
Figure 6.3   Stall behavior modeling of the FIDVR phenomenon

6.3   RDSM Parameter Estimation Using CoTDS

The CoTDS simulation model described in Chapter 2 provides a means to generate surrogate data in the absence of a wide variety of data under various scenarios for the purpose of determining the parameters the DS. In Chapter 5, the CoTDS modeling methodology was used to calculate and validate the equivalent feeder impedance of the reduced order model of the of the entire distribution system using steady state data. This methodology is now extended in this chapter to determine the RDSM parameters by also including the dynamics.

The dynamic data that is required is obtained by performing CoTDS simulation on a system comprising of a single-generator connected to the distribution system under study. The transmission system can either be a test system or an equivalent of a large transmission system under study. Since the purpose here is to generate large amount of surrogate data from the distribution system, it is not necessary to consider the entire transmission system. The entire system becomes necessary at a later stage when studying or validating the FIDVR control and mitigation scheme.
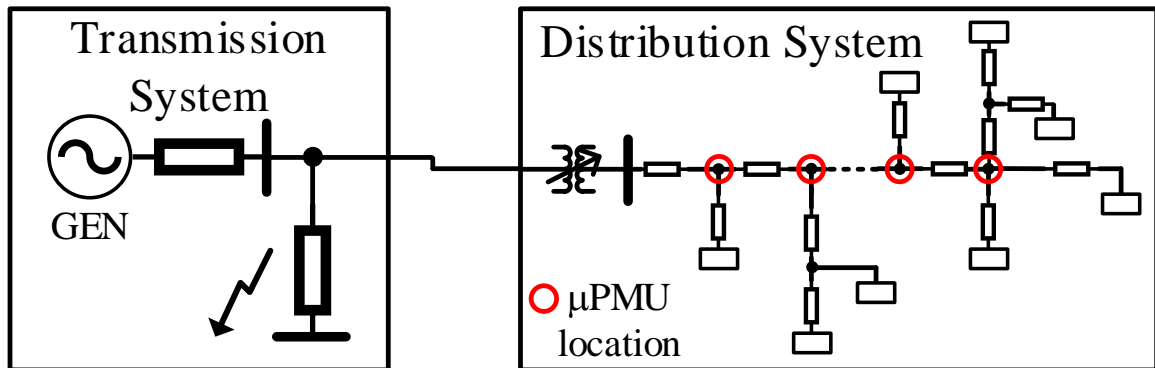
Figure 6.4   CoTDS simulation set up to generate various dynamic measurement data

Fig. 6.4 shows the CoTDS Simulation set up for generating the measured data from the distribution system. The dynamic data is generated by applying a fault on the transmission-

side. The fault is applied at different impedances and different fault times. This leads to various scenarios of transmission system fault which gives a variety of fault voltage and time for which the fault voltage is present. During the CoTDS simulation, the dynamics of each motor in the distribution system is uniquely calculated and their stalling condition is evaluated. As the fault scenario is varied, the number of motors stalling and their recovery is different and this leads to several data sets. The time series data for voltages, active power and reactive power is recorded at the nodes where the μPMUs are placed. The data thus generated is used for determining the parameters of the sub-models of the distribution system.

The sub-model parameters are classified into steady-state network parameters and dynamic load parameters. The steady-state network parameters correspond to the equivalent feeder impedance and the dynamic parameters correspond to the load component parameters as given in Table 6.1. The fraction of each of the load types and DGs is estimated based on the load composition and available data. T

In the absence of real measured data, surrogate data obtained from a CoTDS simulation is used. The steps to determine these parameters are:

1. The CoTDS simulation is run using a single generator and a single line transmission system and the distribution system that needs to be reduced.

2. The steady state data of the sub-station voltage, the active power, reactive power and the voltage data at all the nodes of the distribution feeder are used to determine the equivalent feeder parameters using the method described in Chapter 5.

3. The dynamic data of the voltage, the active power and the reactive power at the transmission side is recorded. This represents the actual data from the actual load.

4. The values of the parameter set λ of the sub-model are determined using an optimization routine to minimize the error between the time series of the measured data, D, and the calculated values, C(λ). Fig. 6.5 shows the processing of the data in an optimization routine to estimate the parameters of the sub-model.

The objective function of the optimization that needs to be minimized, $\eta(\lambda)$, is the sum of squares of the difference between the two time series and is given by Eq. (6.2):

$$\eta(\lambda) = [D - C(\lambda)]^T . [D - C(\lambda)] \tag{6.2}$$

where $C(\lambda)$ is the corresponding calculated values of the data set, D, for a given λ. The calculated values $C(\lambda)$ are obtained by solving the dynamic equations of the sub-model including the effects of the stalling and thermal tripping of the 1-ϕ induction motor.
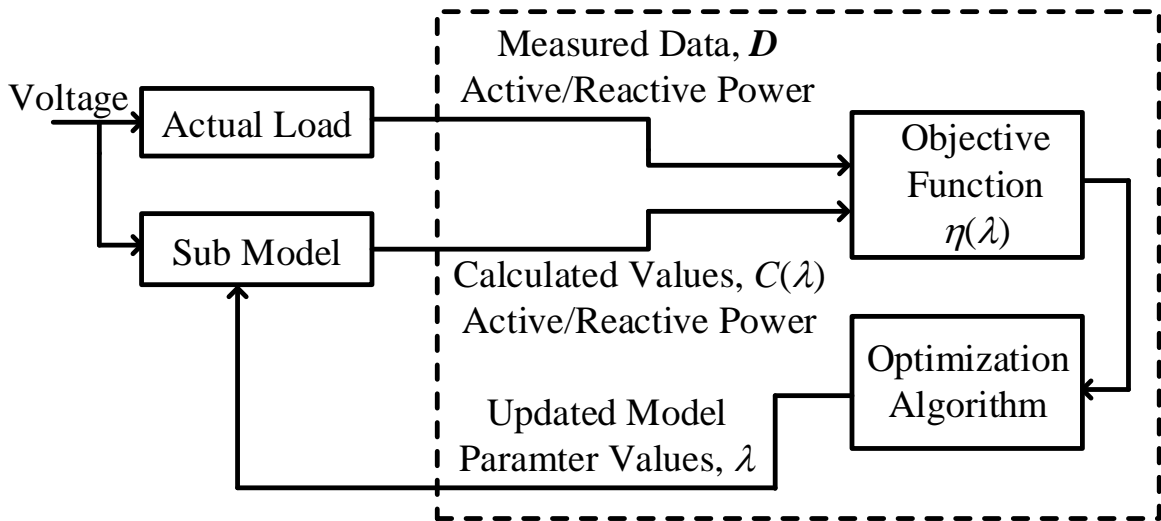
Figure 6.5   Block diagram of methodology for RDSM parameters determination

6.4 Parameter Estimation of IEEE 37-node distribution system

Fig. 6.6 shows the IEEE 37-node system [54]. This feeder is an actual feeder located in California. The figure shows the node locations where the μPMUs are installed for measuring the voltages and power entering each load area. The load areas, represented by the shaded regions are required to be reduced to the sub-models. All the sub-models together with the interconnecting network impedances will form the RDSM representation of the IEEE 37-node distribution system.
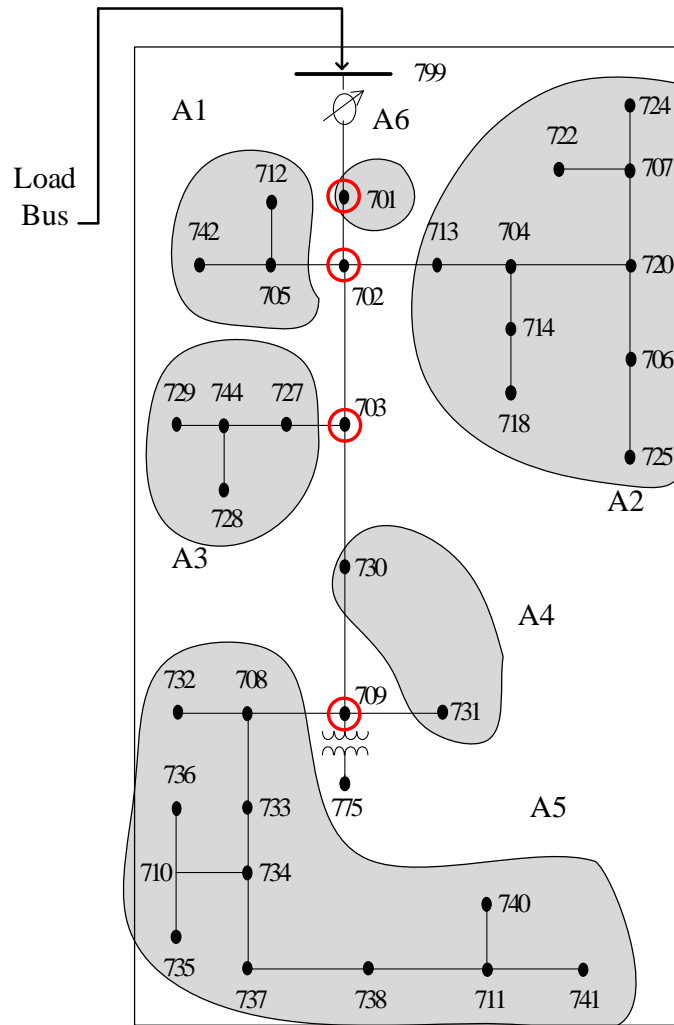
Figure 6.6   IEEE 37-node system for RDSM parameter estimation. The node locations with μPMUs installed are shown by red circles. The shaded regions are the different load areas.

6.4.1   RDSM parameters of IEEE 37-node system

Each of the distribution system loads in the IEEE 37-node feeder is separated into the composite load model components including static, electronic, 3-ϕ IM and 1-ϕ A/C IM. In order to simulate a realistic scenario, the fraction of loads of each type (Fs, Fm3 and Fm1) is assigned according a normal distribution around a mean value which is estimated based on the type of loads present in each location [55]. In addition, each of the motor load types which have their own set of parameters to characterize them and have variability included by connecting several motors with a normal distribution of parameters. This procedure leads to a comprehensive and detailed model of the distribution system.

As stated earlier, the FIDVR behavior is dominated by the stalling and thermal tripping of the 1-ϕ AC induction motors. Therefore, the focus in this work is limited to the optimization of the parameters that are relevant to this behavior and keeping nominal values for the 3-ϕ induction motors. In this example, the F_{dg} is considered to be 0. If there is DG in the system, this can be included as a negative load in the RDSM.

The procedure described in section 6.3 for estimating RDSM parameters is applied to the IEEE 37-node distribution system. From the different sets of data obtained from CoTDS, the sub-model parameters for each of the 6 areas are determined according to the optimization procedure described in the section 6.3. A few parameters for each of the control area are listed in Table 6.2.

Table 6.2   Sub-model parameters of the load areas

Parameter	A1	A2	A3	A4	A5	A6
Root Node	702	702	703	709	709	701
Load kW	178	538	245	160	684	420
F_s	0.61	0.46	0.49	0.49	0.47	0.2
F_{m3}	0.00	0.00	0.225	0.00	0.00	0.7
F_{m1}	0.39	0.54	0.29	0.51	0.53	0.1
V_{stall}	0.384	0.361	0.443	0.404	0.429	0.443
T_{stall}	0.096	0.094	0.095	0.097	0.095	0.095
R_{stall}	0.081	0.088	0.079	0.083	0.099	0.078
X_{stall}	0.099	0.108	0.105	0.101	0.121	0.105
T_{th}	13.63	13.77	12.31	13.83	15.83	12.31
θ_1	0.450	0.650	0.450	0.479	0.663	0.450
θ_2	2.157	2.058	2.196	1.939	1.798	2.196

6.4.2   Validation of sub-model parameters with CoTDS simulation data

To demonstrate the accuracy of the sub-model parameters determined from the optimization, the dynamic behavior of each of the sub-model for the different load areas is compared to the data that we obtain from the CoTDS simulation. The the active and reactive powers of the different areas are plotted in Fig. 6.7(a) and Fig. 6.7(b) for a fault scenario using both the CoTDS simulation and that obtained from the corresponding sub-model. It can be seen that the active and reactive power profiles of the sub-model closely matches the data from CoTDS simulation at all the load areas for almost the entire recovery period after the fault and captures the FIDVR behavior. The active and reactive powers also matched well for various other fault scenarios. These plots and observations verify that each of the sub-models can indeed capture the overall behavior of the full model CoTDS simulation with a reasonable degree of accuracy and thus validates the parameters obtained from the developed optimization procedure.

113
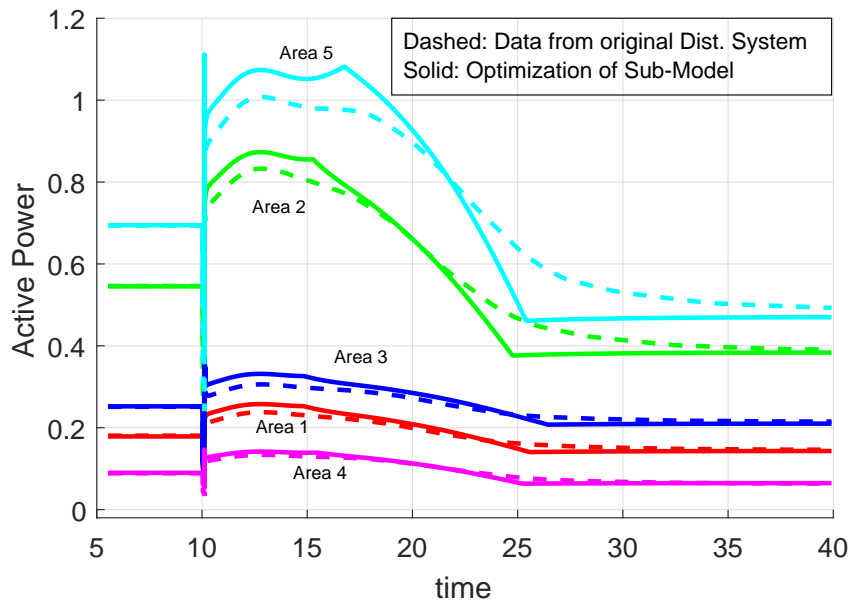
(a)
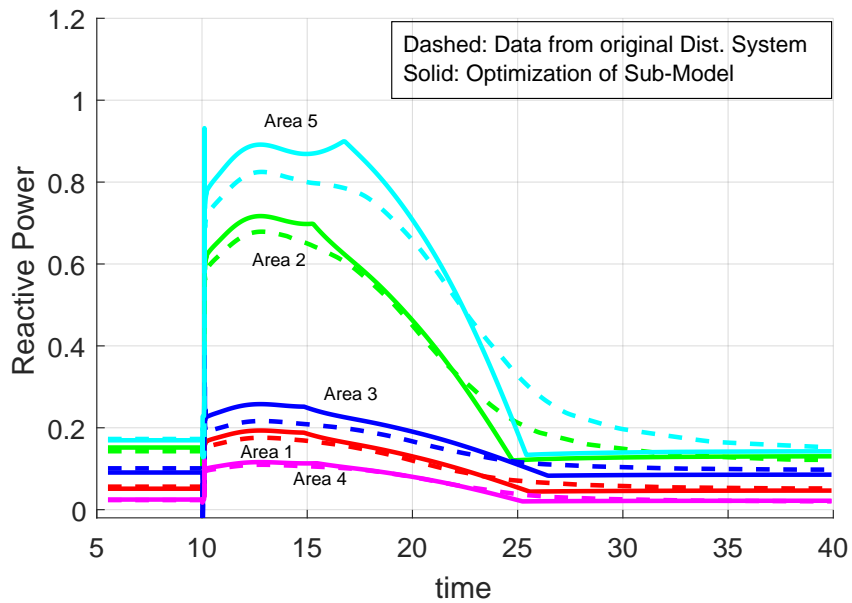
(b)

Figure 6.7 (a) Active power and (b) Reactive power, of the areas using CoTDS simulation of the original distribution system and the sub-model parameters of each load area.

6.4.3 Validation of RDSM replacing the Distribution system in CoTDS simulation

In the previous section, each of the sub-models was validated against the data obtained from CoTDS simulation. Now, the sub-models are put together to form the RDSM as described in Section 6.2. It is expected that the RDSM will produce data that is similar to that obtained from using the complete distribution system model with all the various loads connected at all the nodes.

Fig. 6.8(a) shows the dynamic voltage recovery for different faults. The fault applied is same as that for which the original CoTDS simulation was performed with the complete distribution system. It can be observed that the resulting voltage profile matches very well with the original data for all the faults. The correspondence can also be seen on the input active and reactive power to the distribution system in Fig. 6.8(b) and 6.8(c). This therefore validates the RDSM to replace the distribution system for performing dynamic simulation.

(a)
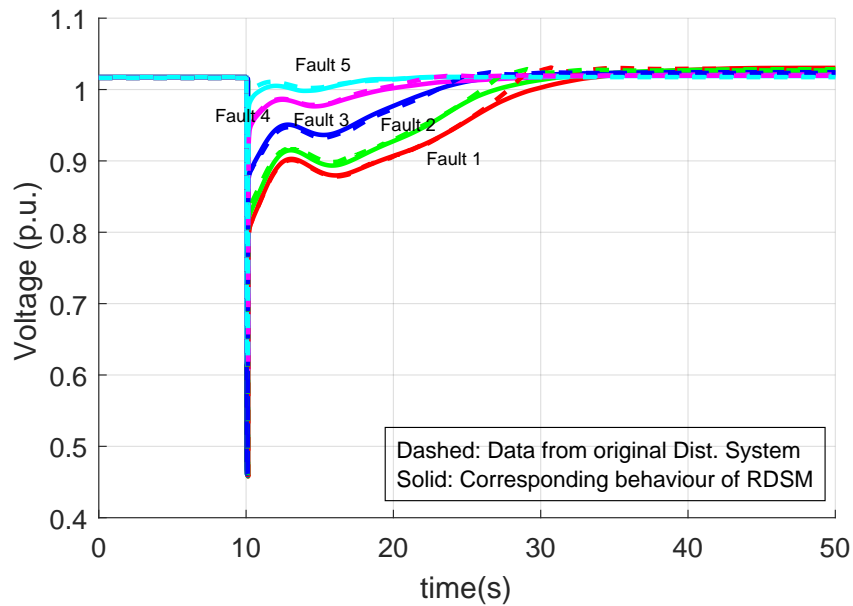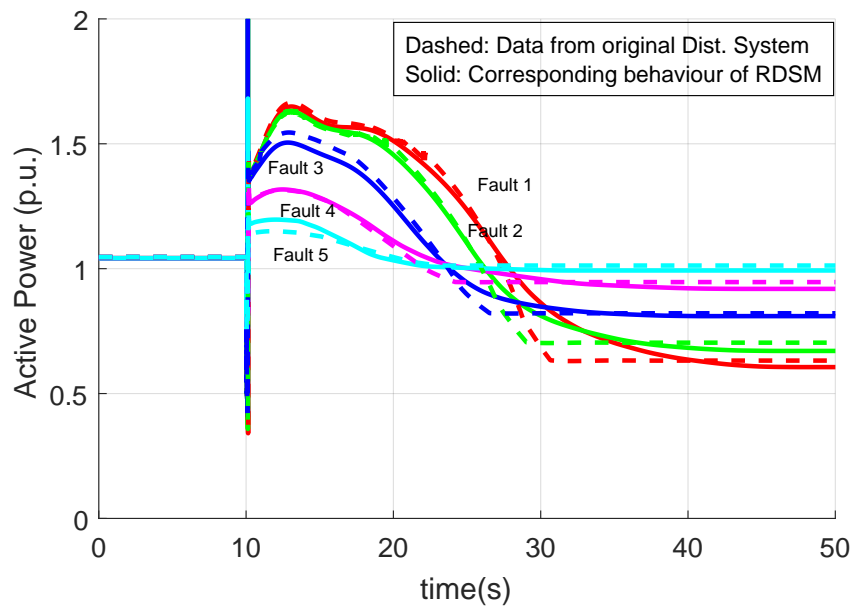
(b)
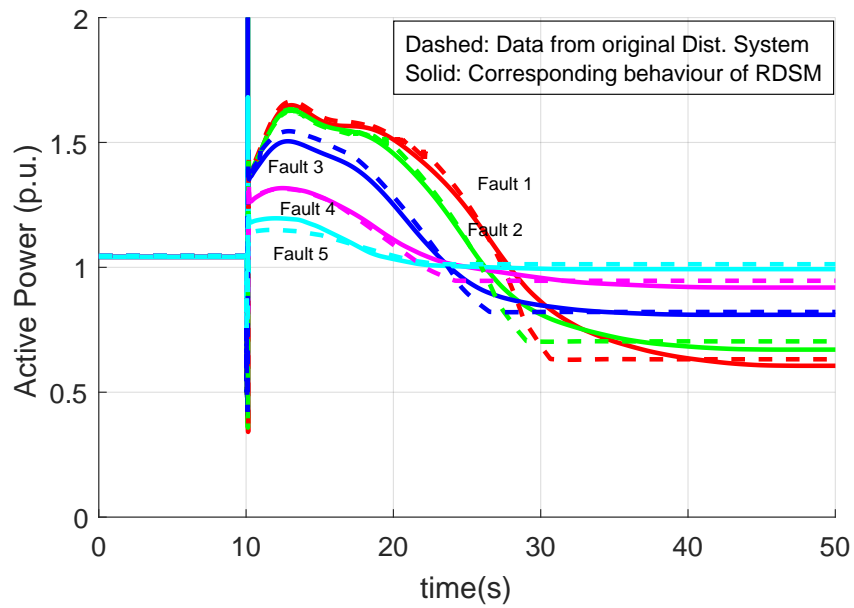
(c)

Figure 6.8   Comparison of (a) Sub-station bus voltage (b) Active power and (c) Reactive
power, of the RDSM using CoTDS simulation with that obtained from CoTDS
simulation of original distribution system.

6.5   Conclusion

In this chapter, the detailed distribution system is reduced in size and is represented by RDSM. The proposed RDSM is composed of sub-models that are analogous to the WECC CLM and aggregates the distribution system into load areas while ensuring the overall dynamics are retained. The modeling approach uses CoTDS simulation that was demonstrated in the Chapter 2 to generate measurement data using the network topology and load data. This measurement data is employed to estimate the parameters of the RDSM by matching the dynamics of the model to that obtained form the data.

The sub-model of the RDSM distinguishes itself from the WECC CLM in the modeling of the 1-ϕ induction motor load with respect to the stalling and thermal recovery. While in the WECC CLM, the stalling and thermal recovery is limited to extreme behaviour, the proposed model can capture intermediate behaviour as well which is necessary for mimicing real practical data.

To test the proposed scheme, a dynamic co-simulation is performed with several fault scenarios on the IEEE 37 node distribution system connected to IEEE 9 bus transmission system. This RDSM is shown to correspond well with the dynamic behavior of the full distribution system under various fault scenarios. Therefore, the RDSM can replace the entire distribution system and can used for performing accurate system dynamic studies. This model can further be used for conducting dynamic studies and also enables the development of mitigation and control of undesirable events like FIDVR.

CHAPTER 7.   IMPACT OF DG PENETRATION ON TRANSMISSION SYSTEM DYNAMICS

7.1   Background on Standards

The significant increase in DG is leading to development of new performance and reliability standards. The Federal Energy Regulatory Commission (FERC) has recently announced [56] that such generators must ride through abnormal frequency and voltage events. It states that the specific ride through settings must be consistent with Good Utility Practice and any standards and guidelines applied by the transmission provider to other generating facilities on a comparable basis. It is also stated that they should have appropriate ride-through requirements comparable to large generating facilities.

The strong motivation behind these requirements is to ensure a high reliability of the interconnected power system, and so, the DGs must continue to remain connected during disturbances and at the same time they cannot be connected forever in the event of a fault or power system malfunction. The IEEE standard 1547 provides the technical specifications for, and testing of, the interconnection and interoperability between utility electric power systems (EPSs) and DG sources. It provides requirements relevant to the performance, operation, testing, safety considerations, and maintenance of the interconnection.

In this chapter, the focus is on the Voltage Ride Through (VRT) requirements pertaining to the IEEE standard 1547 as shown in Fig. 7.1. For low-voltage ride-through and undervoltage trip, the relevant voltage at any given time shall be the least magnitude of the individual applicable voltages relative to the corresponding nominal voltage. For high-voltage ride-through and overvoltage trip, the relevant voltage at any given time shall

be the greatest magnitude of the applicable voltages relative to the corresponding nominal voltage.
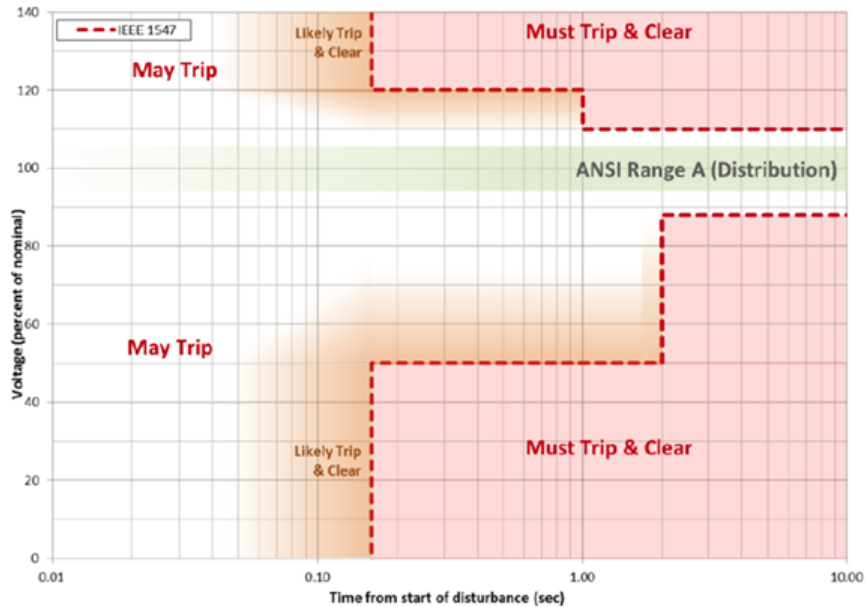
Figure 7.1   IEEE standard 1547 Voltage Ride Through Requirement

The NERC report [57] on Distributed Energy Resource: Connection Modeling and Reliability Considerations contains the recommendations by the Integration of Variable Generation Task Force (IVGTF) on the voltage and frequency ride-through requirements to the IEEE standard 1547 which are currently being revised [58]. For the purpose of the study contained in this paper, the IVGTF recommendations for Voltage Ride Through (VRT) shown in Table 7.1 are applied.

Table 7.1   IVGTF Recommendations for IEEE standard 1547 VRT settings

Voltage Range (% nominal)	Max clearing time (s)	Voltage Range (% nominal)	Max clearing time (s)
<50%	0.16	<110% to 120%	1.0
50% to 88%	2.0	>120%	0.16

The FIDVR phenomenon has been explained in Chapter 5. It has been shown in liter-ature [59] that there is beneficial impact on the grid with increased PV generation on the system response following a fault. But on the contrary, when subject to the IEEE standard 1547 ride-through requirements, the results can be quite different. [60] demonstrates that the voltage recovery with higher PV is worse than the base case without PV. However, ride-through requirements are not considered as a part of the study. In addition the effect of stalling of the single-phase induction motor and the thermal tripping were not included.

To plan and address incidents caused by this phenomenon, the Section R5 of the NERC standard TPL-001-4 [1], states that each transmission system planner shall have criteria for acceptable system voltage limits including voltage transients. Considering that the DGs can affect the transient voltages depending upon the ride-through capabilities, it is therefore imperative that we must examine the effect of the DG penetration on the power system dynamics and evaluate the result with respect to the criteria set forth by the transmission system planning co-ordinator. An example of such a criteria [61] for normal voltage recovery from Western Electric Co-ordinating Council (WECC) is shown in Fig. 7.2.
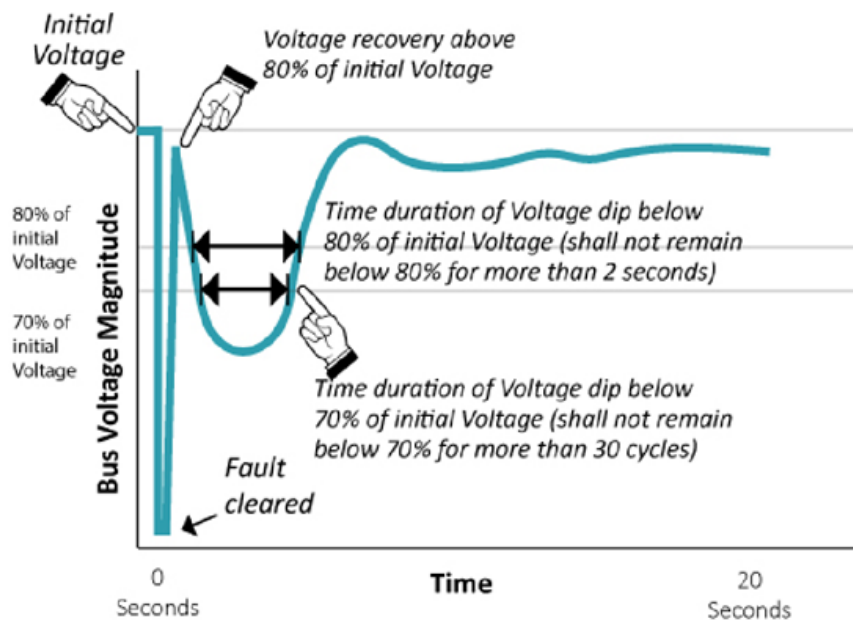
Figure 7.2   WECC Criterion for Normal Recovery

7.2   Fault Analysis using CLM with added DG

The CLM [43] with DG is shown in Fig. 7.3. The load types are classified under 3 main categories: static load, induction motor load and electronic load. Static load is represented by load that is exponentially dependent on the load bus voltage. Typically, these exponents corresponds to the conventional ZIP model. Induction motors are further classified into 3 types of 3-phase induction motors (A, B, C) depending upon their application and one single-phase air conditioner (A/C) motor (D) which represents the motors used in A/C compressors. The lumped feeder impedance and the feeder shunt compensation are represented by R_f, X_f and B_f respectively. The sub-station transformer model converts the system voltage to the low-side feeder voltage along with regulation. This comprehensive model also includes all the under-voltage protection features of all the induction motor types and the stalling and thermal tripping of the single-phase induction motor to describe the aggregated load. A DG model developed in Chapter 3 is added to the CLM to include the effect of distributed DG at the load end. These represent predominantly deployment of solar inverter installations.

7.2.1   Steady State pre-fault

The actual load P_{L0} and Q_{L0} at pre-fault condition are determined by the individual fractions of the three phase induction motors (FmA, FmB, FmC), the single-phase A/C motor (FmD), the electronic loads (Fel) and the static loads (remaining fraction). The value of the total feeder reactive compensation (B_f) is computed during initialization of the model to balance the reactive consumption of the load components, the transformer and the network impedances with the load Q value specified in the power flow data [43]. The effective load at pre-fault (P_{eff0}, Q_{eff0}) at the load bus as seen by the system bus is the difference between the actual load and the power sourced by the DG (P_{DG}, Q_{DG}) and is
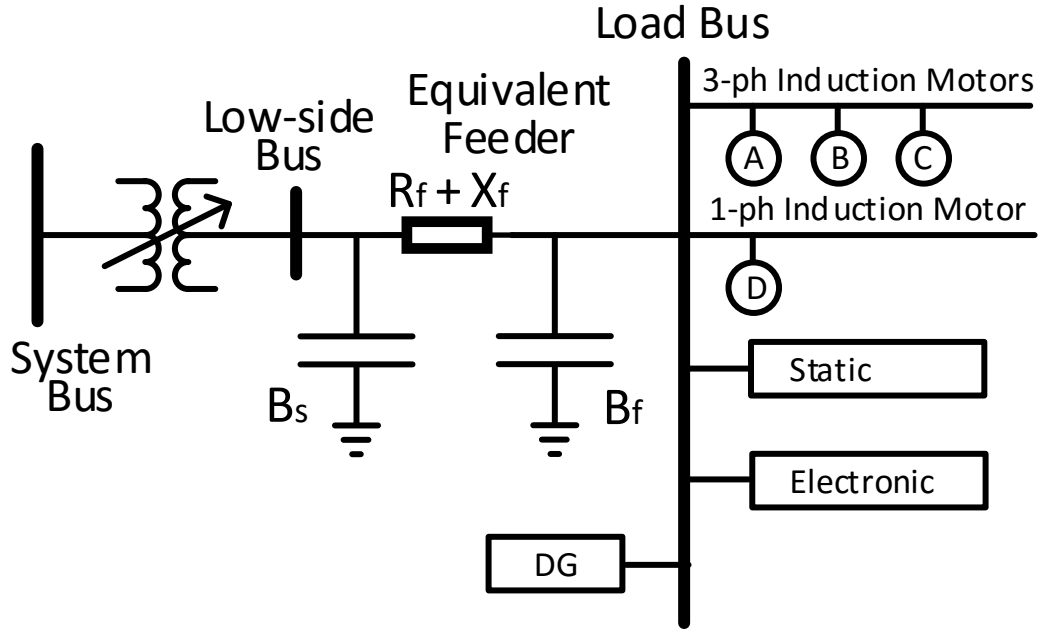
Figure 7.3 The WECC Composite Load Model (CLM) with added DG.

given by equation (7.1).

$$P_{eff0} = (P_{L0} - P_{DG})$$
$$Q_{eff0} = (Q_{L0} - Q_{DG})$$
(7.1)

Here, P_{L0} and Q_{L0} are

$$(P_{L0}, Q_{L0}) = f_{pre}(P_0, Q_0, \lambda_{CLM})$$
(7.2)

where, f_{pre} is a function to determine the load based on the CLM parameters, λ_{CLM}, described in [43].

We define the DG penetration as Fdg which corresponds to the fraction of DG active power with respect to the total load and $PFdg$ as the DG operating power factor. Therefore,

$$P_{DG} = Fdg.P_{L0}$$
$$Q_{DG} = \frac{\sqrt{1 - PFdg^2}}{PFdg}.P_{DG}$$
(7.3)

7.2.2 Post-fault dynamics

Consider a three-phase to ground fault on one of the transmission system buses. This will cause the system bus voltages to drop instantly and if this goes below the stall voltage (V_{stall}) specification for a time greater than the stall time (T_{stall}) of the single-phase A/C motor, then the motor stalls. Under such conditions, the reactive power at the load significantly increases. This causes the voltage at the system bus to oscillate due to the combined dynamics of the generators, motors and the transmission lines and does not quickly recover back to the pre-fault voltage levels.

Now, let us consider the effect of the DGs in the post-fault dynamics. There are two scenarios. The first is that the voltage at the DG input meets the criteria for "no-trip" and so rides through the fault without tripping. And the second is that the DG rides through the fault and after a certain time when the voltage fails the criteria for "no-trip" zone, it can trip and when it does the power into the grid reduces.

The effective load at post fault condition can therefore be expressed as

$$
\begin{aligned}
p_{eff1}(t) &= (p_{L1}(t) - K.p_{DG}(t)) \\
q_{eff1}(t) &= (q_{L1}(t) - K.q_{DG}(t))
\end{aligned}
\tag{7.4}
$$

where, $(p_{L1}(t),\ q_{L1}(t))$ are dynamically varying load that are determined not only by the fractions of each load, but also by the fraction of load that has tripped and/or stalled due to the fault.

$$
(p_{L1}(t), q_{L1}(t)) = f_{post}(P_0, Q_0, \lambda_{CLM}, t)
\tag{7.5}
$$

The factor K in equation (7.4) is set as 1 if the DG has not tripped and 0 if the DG has tripped. Similar to f_{pre}, the function f_{post} determines the load after the fault based on the CLM parameters, λ_{CLM}. The active and reactive power, $p_{DG}(t)$ and $q_{DG}(t)$ of the DG at the corresponding load bus is computed according to the dynamic model described in Chapter 3.

7.2.3 Solution to System Dynamics after fault

The expected delayed voltage recovery of the bus voltage is shown in. Fig. 7.4. In this figure, time $t = 0$ to $t0$ represents the steady-state operation. At time $t0$, a fault is applied resulting stalling of single-phase A/C motors. This leads to a delayed voltage recovery from $t1$ to $t2$ due to increased reactive power consumption of the stalled motors. As the temperature of the stalled motors increases, gradually the voltage recovers due to increasing fraction of the motor load dropping with the rate dictated by the thermal time constant of the single-phase A/C motor model.

The actual recovery depends on the transmission system dynamics represented by its differential algebraic equations and the effective load dynamics given by equation (7.5). The system is solved using the co-simulation approach ... In the transmission system time domain simulation, the load at the load buses modeled by the aggregated CLM with DG are resolved at every time-step using Equation (7.4).
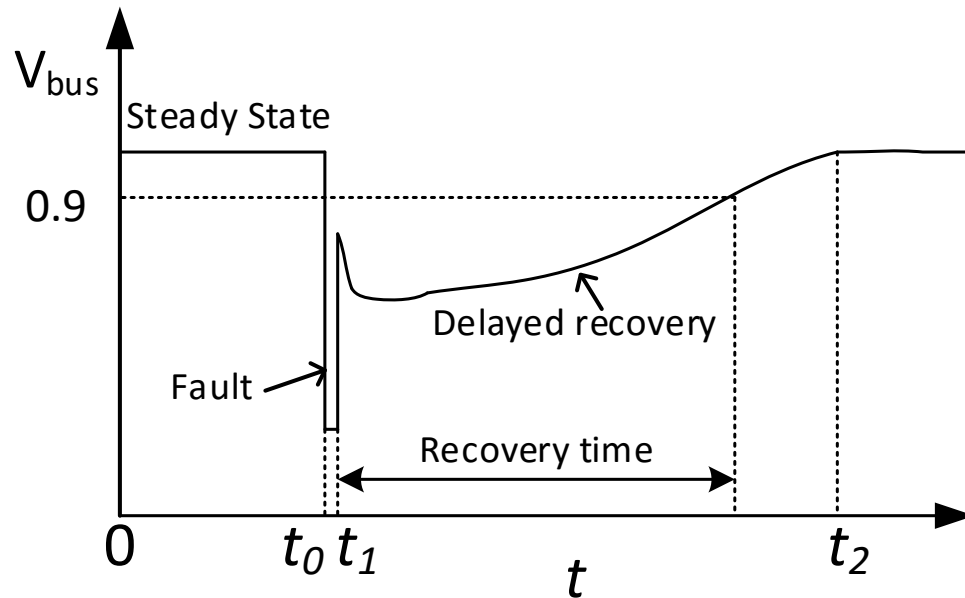
Figure 7.4   Expected delayed recovery behavior of bus voltage due to fault

7.3   Case Study with New England 39-bus system

A New England 39-bus system [62] as shown in Fig. 7.5 is considered for this study. This system has 29 load buses and 10 generator buses. The objective of this case study is to determine the effect of DGs on the delayed voltage recovery behavior. As this behavior is dependent on the voltage level at fault which determines the stalling characteristics of the induction motors located on that bus, we can selectively choose buses to replace the constant PQ load with dynamic load representation. Based on the voltage dip threshold criteria derived in in [10], we identify those buses where the voltage goes below 0.75 pu due to a three-phase to GND fault applied at bus 15, and replace the constant PQ load on these buses with distribution system models. The identified buses are 3, 4, 7, 8, 12, 14, 16 and 18. Buses 20 and 21 are also included due to their proximity to the fault.

The simulation study is done using the developed CoTDS co-simulation. The transmission system of 7.5 is the sub-system T in the CoTDS co-simulation. The sub-systems D1-D10, the equivalent distribution system loads shown in Fig. 7.6 are the aggregated CLM [43] with DG and are represented by a combination of static load model, electronic load model, 3 types (A, B and C type motor) of 3-phase induction motor models, and a single-phase air conditioner motor model (D type motor). The load fractions are listed in Table 7.2. It is to be noted that the static load is calculated as the remainder of the sum of all the other loads. In addition, the fraction of DGs added to the CLM are designated by fraction, Fdg. In this case study, the Fdg is varied between 0 and 0.4.

Table 7.2   Load Fractions

Description	Designation	Value
3-ϕ Induction Motor, type A	FmA	0.12
3-ϕ Induction Motor, type B	FmB	0.12
3-ϕ Induction Motor, type C	FmC	0.12
1-ϕ Induction Motor, type D	FmD	0.1 to 0.4
Electronic Load	Fel	0.14
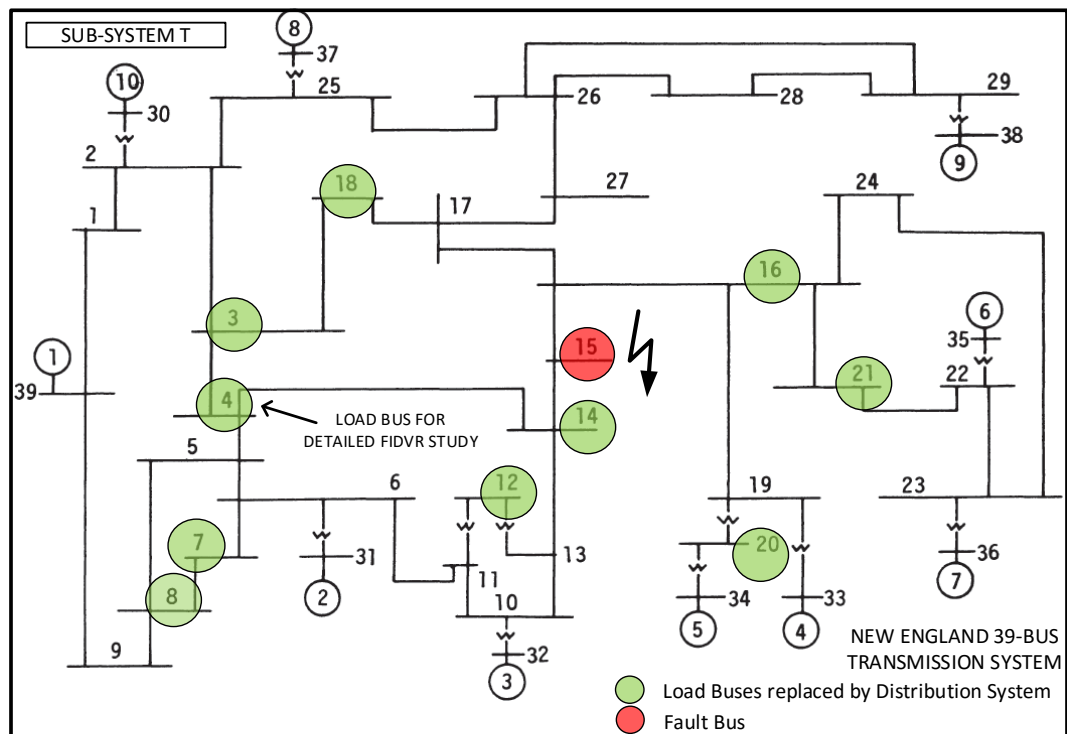
Figure 7.5   New England 39-bus transmission system with PQ load at ten load buses re-
placed by equivalent aggregated CLMs with DG.
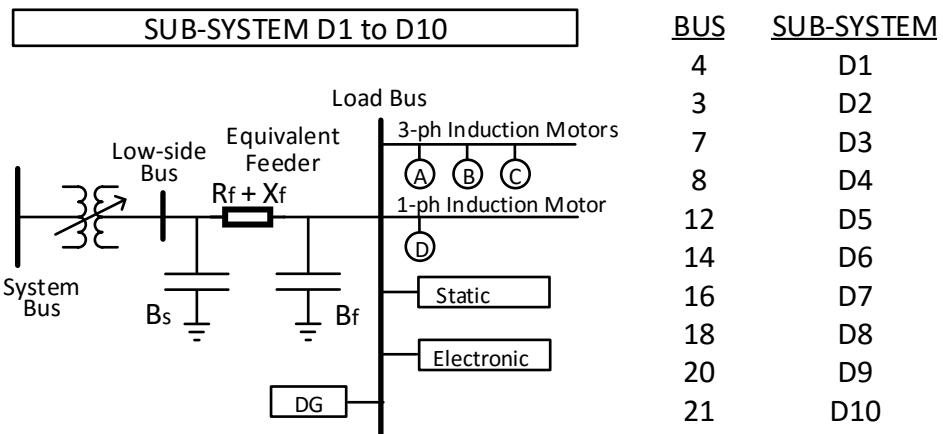
Figure 7.6   The aggregated CLM with DG in the corresponding load buses.

7.4 Simulation Results

The simulation of the case study is setup in PSAT [30] placing the CLM with DG on the identified buses. The CLM and the DG model are developed in MATLAB in conjunction with the PSAT time-domain transient stability program. The simulation is setup to detect for voltage violation of a transient voltage response of the system. In this simulation example, the WECC criteria [61] is used to set the bus voltage limits after a fault is applied. Due to the presence of DG intially, we could expect to see the steady state bus voltage settling at a higher value than without the DG. Therefore, it is assumed that the initial shunt compensation be adjusted for each DG level to keep the bus voltages at levels close to the case of no DG.

7.4.1 Effect of Fdg on voltage recovery

Fig. 7.7(a) shows the effect of the DG levels on the voltage recovery due to a fault as described in the previous section. For the purpose of comparison, the FmD value is set to be 0.2 and the DG power factor is 0.90. Prior to applying the fault, the simulation is run to steady state. As expected, the initial steady state bus voltage is slightly higher for increased values of Fdg due to corresponding lower P_{eff0} and Q_{eff0} from Equation (7.1).

In this study, the DG is always active and not allowed to trip. It can be observed that the initial dip on the bus voltage after the fault is lower with increasing DG levels and correspondingly the voltage recovers faster. This is a result of DG riding through the fault and continuing to deliver power during the recovery and thereby aiding the recovery.

7.4.2 Effect of FmD on voltage recovery

The fraction of single phase A/C motors, FmD, plays a significant role in the recovery of the bus voltage even in the presence of DG. For the purpose of comparison, the case of DGs tripping (when the DG voltage is outside of the boundary of the VRT no-trip zone) is considered. Fig. 7.7(b) shows the variation of recovery profiles for various values of FmD.

It can be seen that the severity of the delayed voltage recovery increases when the FmD increases. This is due to the fact that there is significantly higher reactive power load during post-fault dynamics with higher FmD as demanded by the stalled A/C motors. However, as these motors go through thermal trip, the effective load decreases and so when FmD is higher, the bus voltage settles at a higher value.
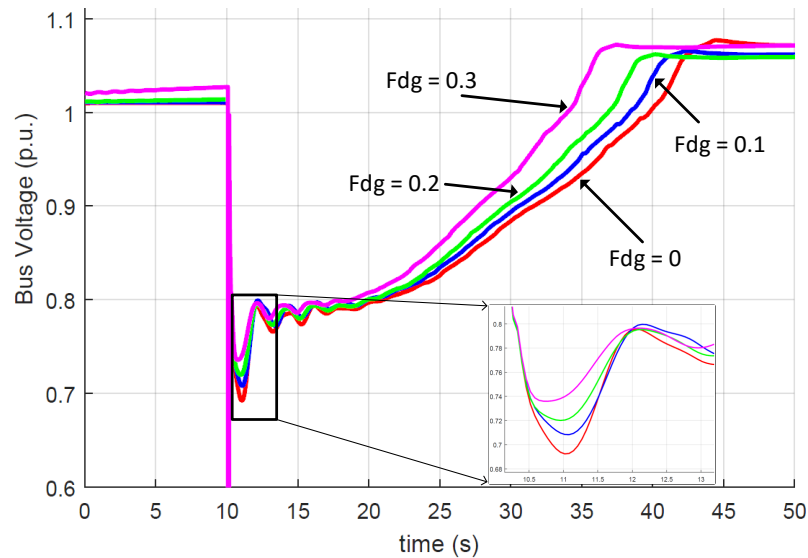
(a)
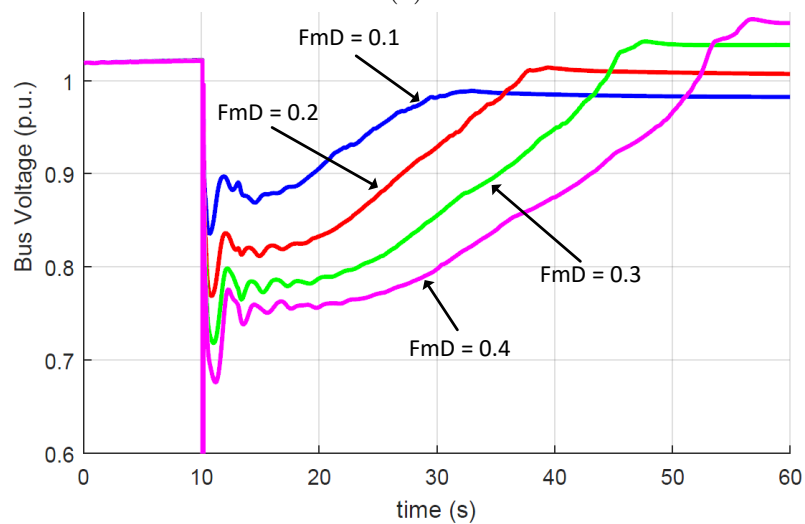
(b)

Figure 7.7   Effect of (a) Fdg on voltage recovery of Bus , (b) FmD on voltage recovery

7.4.3 Effect of DG tripping on voltage recovery

Now, let us consider the case of DG tripping when the voltage excursion is outside of the VRT no-trip zone. Fig. 7.8 compares this case with a) fault recovery in the absence of DG and b) fault recovery in the presence of DG, but DG stays connected and operational. From the plot, it can be ascertained that when DG exists, but then eventually trips, the recovery is much slower and can possibly cause a violation of the transient voltage criteria (Violations are discussed in Section 7.4.4). This behaviour is due to the fact that the DG which was providing local active and reactive power, is suddenly disconnected, the voltage drops as a result of insufficient reactive power. In order to meet the Voltage Ride Through criteria, the DGs are modeled to meet the standards shown in Table 7.1. In this case study, it is assumed that all the DGs will trip when their voltage levels are outside the no-trip boundary. According to IEEE standard 1547, the DGs cannot restart for 5 minutes after tripping, provided that voltage and frequency have recovered to within tolerance. Therefore in this case study, where the simulation is expected to run to approximately 1 minute, the DGs are not set to restart after they trip.
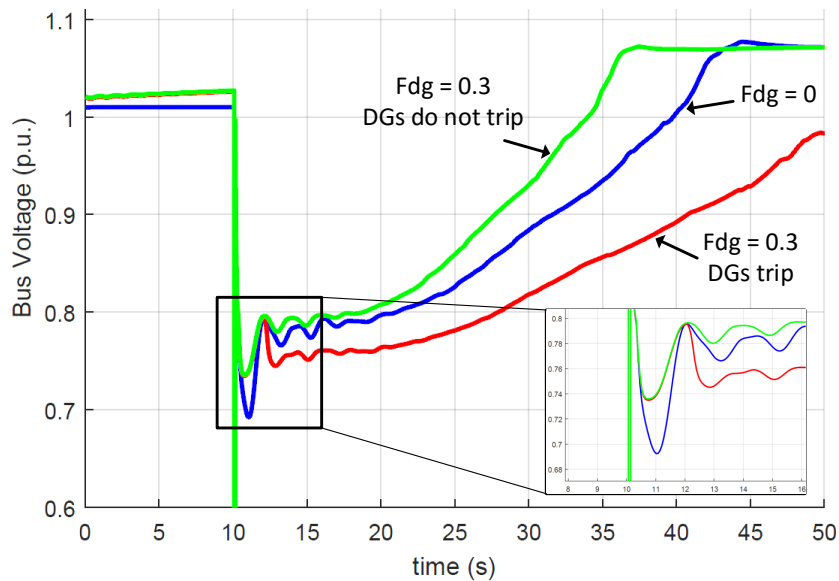
Figure 7.8   Comparison of voltage recovery with DG tripping, not tripping against total absence of DG.

7.4.4   Violation of transient voltage criteria and recovery time

Based on the simulation results presented in the previous sections, it is evident that these factors have an impact on the delayed voltage recovery and correspondingly the violation of the transient voltage criteria. As the DGs trip during post fault dynamics, the bus voltages drop and then the voltage recovery is further delayed.

A total of 16 cases are simulated with FmD varying from 0.1 to 0.4 and Fdg varying from 0.1 to 0.4. A bus is defined as a violating bus if it fails to meet the criteria shown in Fig. 7.2. Furthermore, the delayed voltage recovery is quantified by computing the recovery time from the instant of the fault to the time it finally goes above 0.9 p.u to settle down to its new steady state level.

An example plot of all the bus voltages of the New England 39-bus system is shown in Fig. 7.9 for $FmD = 0.20$, $Fdg = 0.30$. From Fig. 7.9, it can be observed that there are certain buses that traverse below the limit of 80% of initial voltage for more than 2s. These buses violate the transient voltage criteria. The black dashed line is just a representation of 80% nominal voltage, although individual buses need to be checked against their respective initial voltage prior to the fault.

Table 7.3 shows the summary result of the 16 test cases. For a given FmD, the number of violating buses increases for higher Fdg indicating that higher level of DG penetration can result in failure of the transient voltage criteria. Higher FmD can exacerbate the voltage violations. This is also evident from the recovery times where higher FmD and Fdg prolong the voltage sag duration.

Quite remarkably, when the FmD is relatively lower, a higher Fdg can cause the system to not recover as some of the bus voltages settle at below 0.9 p.u. The reason is that the initial steady state voltage is achieved with the load being supported by the DG. Therefore the loss of DG causes the voltage to stay lower. On the other hand, when FmD is higher, the single-phase A/C motor stalls and goes through thermal trip causing partial load shedding. This roughly compensates to help in recovering the voltage back to normal.
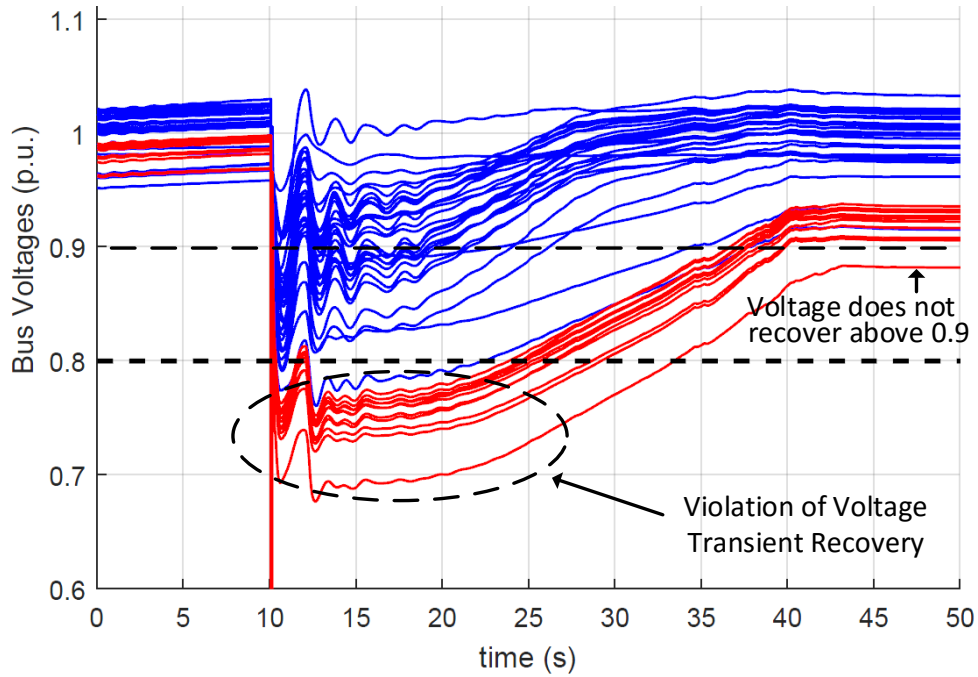
Figure 7.9   All Bus voltages

Table 7.3   Violating Buses and Recovery time

FmD	Fdg	No. of Buses Violating	Recovery time (s) to 0.9 p.u.
0.1	0.1	0	19.3
0.1	0.2	1	N/A
0.1	0.3	1	N/A
0.1	0.4	5	N/A
0.2	0.1	3	25.7
0.2	0.2	11	30.6
0.2	0.3	11	N/A
0.2	0.4	11	N/A
0.3	0.1	11	33.6
0.3	0.2	11	37.6
0.3	0.3	13	40.7
0.3	0.4	14	N/A
0.4	0.1	11	42.8
0.4	0.2	13	46.5
0.4	0.3	14	49.6
0.4	0.4	16	51.0

7.5 FIDVR on load bus 4 replaced by a detailed distribution system

In this section the a detailed distribution system shown in Fig. 7.10 is connected on bus 4 of the New England 39-bus transmission system shown in Fig. 7.5. The distribution system at bus 4 is sub-system D1 which is a 5780-node distribution system made up of 170 IEEE34-node feeders [63]. This feeder has load specification readily available at each node. However, in this simulation the loads at each node of the feeder are replaced by detailed models comprising of static, electronic, 3-phase induction motors and 1-phase induction motors. In addition, the sub-system D1 is composed of 3 categories: residential (40% of total feeders), commercial (30% of total feeders) and industrial (30% of total feeders). In each category, the loading fractions for each type of load is different and therefore appropriately chosen as presented in [49]. This then determines the individual fraction of each load type in each node in each of the feeders. The sub-systems D2-D10 remain the same as in Fig. 7.6, with the exception of $Fdg = 0$.
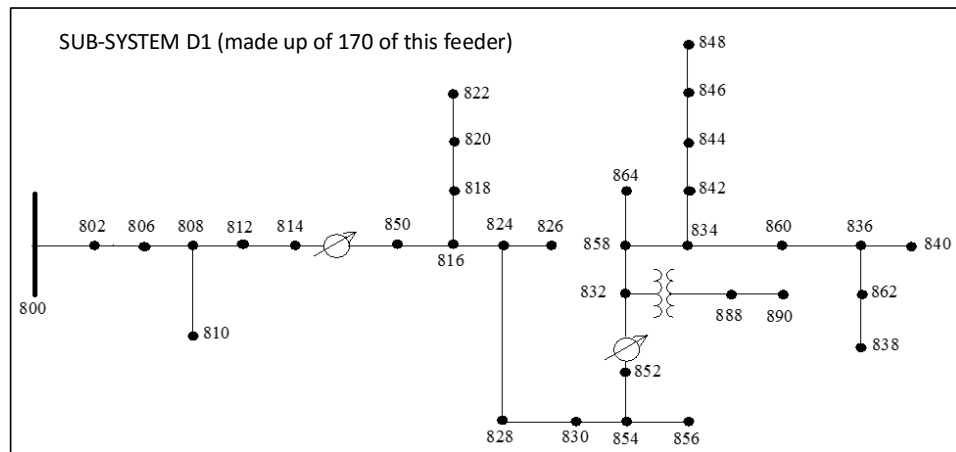
Figure 7.10   Load Bus 4 in the New England 39 bus system.

The CoTDS dynamic co-simulation as described in Section 2.2 using the series computation method is now executed on this complete system (sub-system T and sub-systems D1-D10). A 5-cycle 3-phase to GND fault is applied on Bus 15 of the 39-bus transmission system. The fault leads to an FIDVR phenomenon. The voltage excursion of representative

load nodes of the distribution system in each category is plotted in Fig. 7.11. The detailed effect of under-voltage trip, reconnection and thermal trip characteristics of different types of induction motors in various load nodes can be captured using the co-simulation approach including the entire distribution network.

This results in this section illustrate the effectiveness of the CoTDS co-simulation method to capture the internal dynamic details of the distribution system along with the dynamics of the transmission system. This setup can be further used for advanced studies of the impact of DGs placed in the distribution system including the effect of DG parameters, network impedances, location, penetration levels, etc.

Figure 7.11   FIVDR study on a detailed distribution system on Bus 4 of the New England 39-bus transmission system.

7.6   Conclusions

In this chapter, post fault dynamics due to effect of the variation of DG levels in view of the IEEE standard 1547 VRT requirements is analyzed using the WECC CLM developed in PSAT with the addition of DG model. A case study is developed on the New England 39-bus system by applying the CLM on buses in the neighborhood of the fault. Simulation studies are conducted on a range of DG penetration levels (Fdg) and single-phase A/C induction motor load composition (FmD) to identify violation of the transient voltage as per the NERC TPL-001-4 requirement. It is inferred that higher penetration of DG can cause more violating buses. In addition, it is also observed that when the DG trips following a disturbance, a lower FmD can result in voltages not recovering above 0.9V. These results indicates that increased DG penetration requires additional planning for load shedding and managing reactive power resources to address incidents such as delayed voltage recovery.

It is evident that additional details can be observed in the nodes of the distribution system at bus 4 which cannot be observed by just transmission system simulation alone. The residential feeders show a greater voltage sag than the industrial and commercial feeders due to the stalling of the residential air conditioner motors, whereas the industrial feeders show more transient dips due to the restarting of the three-phase induction motors. Moreover, the effect of the entire distribution system including network impedances and load location are captured using the co-simulation methodology. This setup can be further used for advanced studies of the impact of DGs placed in the distribution system including the effect of DG parameters, network impedances, location, penetration levels, etc.
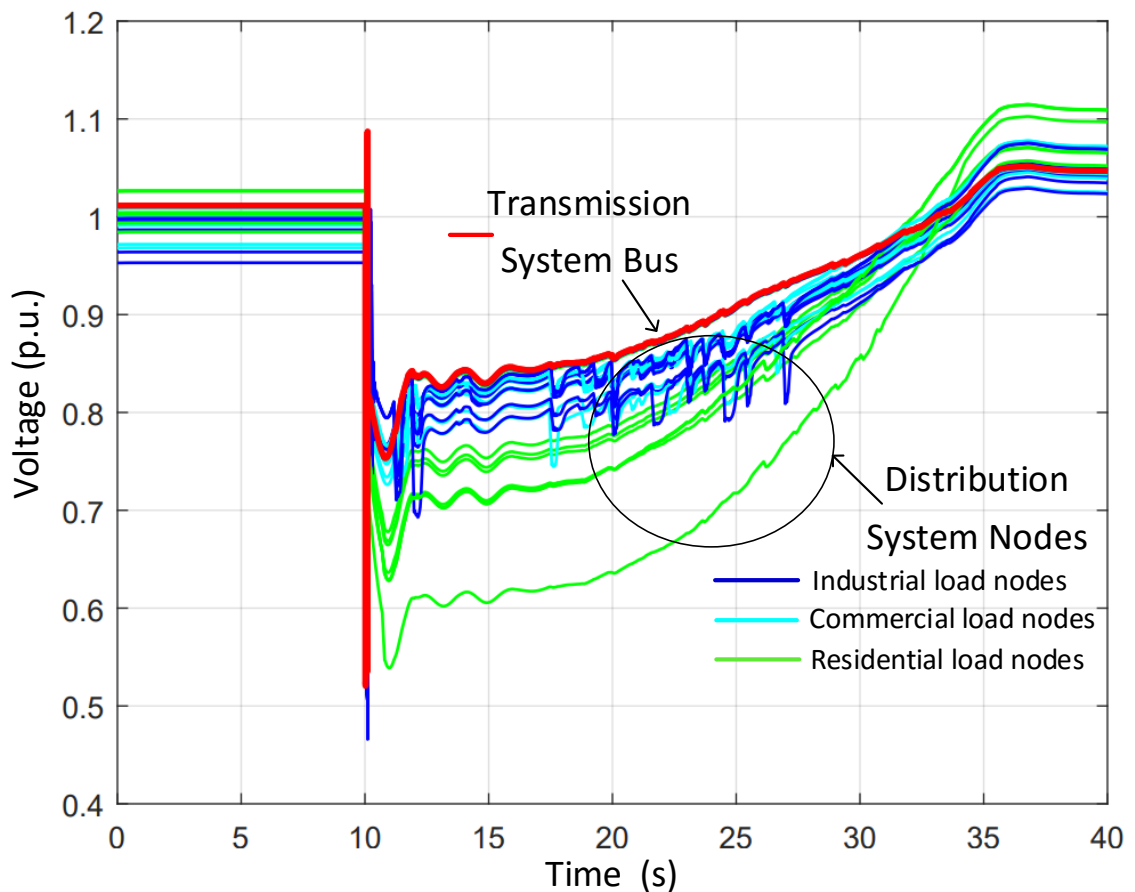
CHAPTER 8.   CONCLUSIONS

8.1   Contributions

1. A methodology for co-simulation of CoTDS are proposed using parallel and series computation of the transmission system and distribution systems. A significant advantage of the proposed co-simulation approach for CoTDS dynamic simulation is that existing software for transmission dynamics and a power flow solver for three-phase distribution system can be used with the addition of an interface to handle the distribution system dynamics. The co-simulation methods are employed in CoTDS dynamic simulation studies and the results correspond well with the total system solution obtained using only one solver for the entire system.

2. The impact of integration time-step on convergence of these two methods is studied against total system simulation. These results are in alignment with what we can expect based on fundamental mathematical analysis of the co-simulation methods. The results presented in this work are a step forward to determine the appropriate integration time step and the co-simulation computation method for numerical convergence. The numerical stability analysis of the proposed co-simulation methods shows that the co-simulation algorithm is stable and convergent as long as the step size, H is not too large. Both the co-simulation methods closely match the true solution. The series computation method is found to be more stable than the parallel computation for relatively larger H.

3. A detailed phasor domain DG inverter model was developed for use in dynamic power system studies with DGs present in the distribution systems. The results of the developed detailed phasor domain model correspond well with the full sine-wave model and capture the details of the dynamics that are not captured using conventional modeling methods used in power system simulations. The effectiveness of the developed co-simulation methods is demonstrated with voltage control methods employed on the distribution side.

4. The CoTDS co-simulation methodology is applied to a distributed load model to represent the load dynamics of the entire distribution system. A procedure to determine the load fractions and the equivalent feeder impedance of the aggregated WECC CLM is developed. The distributed load model using the CoTDS co-simulation approach provides a guidance to calculate the parameters of the aggregated WECC CLM. The delayed voltage recovery profile with calculated parameters matches more closely the distributed load model results than the default impedance of the CLM. The distributed load model using the CoTDS co-simulation can further be utilized for studying parameter sensitivities and an example is provided to illustrate the limitation of the aggregated CLM.

5. The Reduced Distribution System Model is proposed, which is composed of submodels that are analogous to the WECC CLM and aggregates the distribution system into load areas while ensuring the overall dynamics are retained. The stalling and thermal recovery of the single-phase A/C motor is modeled to not only capture extreme severity of FIDVR but also any intermediate level of severity. To test the proposed scheme, a dynamic co-simulation is performed with several fault scenarios on the IEEE 37 node distribution system connected to IEEE 9 bus transmission system. This RDSM is shown to capture the dynamic behavior of the full distribution system under various fault scenarios.

Therefore, the developed RDSM can replace the entire distribution system and can used for performing accurate system dynamic studies and also be used for the development of FIDVR mitigation schemes.

6. The impact of DG penetration levels is studied in view of the IEEE standard 1547 VRT requirements for interconnection of DG to electric grid is analyzed using the WECC CLM developed with the addition of DG model. The developed method is employed in various test cases with combination of 1-ϕ induction motor levels and DG penetration. It is inferred that higher penetration of DG can cause correspondingly more violating buses during a FIDVR event.

8.2   Future Work

1. In this thesis, the time step impact on convergence is studied in the simulation of transmission and distribution system using a dynamic co-simulation method. Further mathematical analysis is required to determine the time step at which the convergence can be guaranteed for successful co-simulation. The parameters that affect the convergence needs to be systematically analyzed using rigorous mathematical analysis.

2. In this work, opensource software for transmission system simulation and distribution system powerflow was used. This method needs to be extended to commercial software integration for large system studies.

3. The parameter estimation of the composite load model was limited to selected parameters of interest. As the WECC CLM has numerous parameters, it would be useful to develop a procedure to determine all these parameters.

4. The CoTDS co-simulation modeling has been developed for performing time-domain simulation. Linearized small-signal analysis was attempted, but needs additional work for completing the model and study the impact of distribution side loads including effect of location, loading, load composition, etc.

5. The impact of DG penetration has been studied in this thesis from the point of view of FIDVR. The work can be extended for other studies like detailed stability analysis including small-signal modeling with DG and the effect of various parameters, location, penetration levels, power factor, etc.

6. In the reduced distribution system modeling, the optimization was performed using available non-linear optimization tools in MATLAB. Customized optimization methods for this application needs to be developed for better and faster solutions including all the parameters. In addition, dynamic parameters of the DG model also can be included into the sub-model that constitutes the RDSM.

8.3   List of Publications

1. R. Venkatraman, S.K. Khaitan, V. Ajjarapu, Dynamic Co-Simulation Methods for Combined Transmission-Distribution System with Integration Time Step Impact on Convergence, IEEE Transactions on Power Systems 2018.

2. A.R.R Matavalam, R. Venkatraman, V. Ajjarapu, "Monitoring and Mitigation of Delayed Voltage Recovery using mPMU based Reduced Distribution System Model," under review with IEEE Transactions on Smart Grid (short paper accepted).

3. R. Venkatraman, S.K. Khaitan, V. Ajjarapu, Impact of Distribution Generation Penetration on Power System Dynamics considering Voltage Ride-Through Requirements, IEEE PES General Meeting, 2018.

4. R. Venkatraman, S.K. Khaitan, V. Ajjarapu, Application of Combined Transmission-Distribution System Modeling to WECC Composite Load Model, IEEE PES General Meeting, 2018.

5. R. Venkatraman, S.K. Khaitan, V. Ajjarapu, A Combined Transmission-Distribution System Dynamic Model with Grid-Connected DG Inverter, IEEE PES General Meeting July 2017.

6. R. Venkatraman and S. K. Khaitan, Optimal Reactive Power Allocation to Minimize Line and DG Losses in a Radial Distribution System, IEEE PES GM, 2016.

7. R. Venkatraman and S. K. Khaitan, Apparent Power Sharing Optimization for Parallel Operated Distributed Generators in Microgrids, IEEE EIT Conference, 2016.

8. R. Venkatraman and S. K. Khaitan, A Single-Stage Single-Switching Leg Microinverter for Single-Phase Photovoltaic Systems, IEEE EIT Conference, 2016.

9. R. Venkatraman and S. K. Khaitan, A Survey of Techniques for Designing and Managing Microgrids, IEEE PES General Meeting, 2015.

BIBLIOGRAPHY

[1] NERC, "Standard TPL-001-4 - Transmission System Planning Performance Requirements," http://www.nerc.com/files/TPL-001-4.pdf, 2014.

[2] P. Palensky *et al.*, "Applied Cosimulation of Intelligent Power Systems," *IEEE Industrial Electronics Magazine*, June 2017.

[3] H. Sun *et al.*, "MasterSlave-Splitting Based Distributed Global Power Flow Method for Integrated Transmission and Distribution Analysis," *IEEE Transactions on Smart Grid*, vol. 6, no. 3, pp. 1484–1492, 2015.

[4] K. Balasubramanium and S. Abhayankar, " A Combined Transmission and Distribution System Co-Simulation Framework for Assessing the Impact of Volt/VAR Control on Transmission System," *IEEE PES General Meeting*, 2017.

[5] K.Kalsi *et al.*, "Integrated Transmission and Distribution Control," *PNNL report for US Dept. of Energy*, 2013.

[6] E. Hale *et al.*, "The Integrated Grid Modeling System (IGMS) for combined transmission and distribution system simulation," *IEEE PES General Meeting*, 2015.

[7] M.A. Al Faruque and F. Ahourai , " GridMat: Matlab Toolbox for GridLAB-D to Analyse Grid Impact and Validate Residential Microgrid Level Energy Management Algorithms ," *IEEE PES Innovative Smart Grid Technologies Conference*, 2014.

[8] T.M. Hansen, B. Palmintier, S.Suryanarayanan, A.A. Maciejewski and H.J. Siegel, " Bus.py: A GridLAB-D Communication Interface for Smart Distribution Grid Simulations," *IEEE PES General Meeting*, 2015.

[9] L. Wen-zhuo *et al.*, "An Electromechanical/Electromagnetic Transient Hybrid Simulation Method that Considers Asymmetric Faults in an Electromechanical Network," *IEEE PES PSCE*, 2011.

[10] Q. Huang and V. Vittal, "Application of Electromagnetic Transient-Transient Stability Hybrid Simulation to FIDVR Study," *IEEE Transactions on Power Systems*, vol. 31, no. 4, pp. 2634–2646, 2016.

[11] Q. Huang and V. Vittal, "OpenHybridSim: An open source tool for EMT and phasor domain hybrid simulation," *IEEE Power Energy Society General Meeting*, 2016.

[12] ——, "Integrated Transmission and Distribution System Power Flow and Dynamic Simulation Using Mixed Three-Sequence/ Three-Phase Modeling," *IEEE Transactions on Power Systems*, vol. 32, no. 5, 2017.

[13] X. Zhang, A. Flueck, and S. Abhyankar, "An Implicitly-Coupled Electromechanical and Electromagnetic Transient Analysis using a Frequency Dependant Network Equivalent," *IEEE Transactions on Power Systems*, 2015.

[14] P. Aristidou and T. V. Cutsem, "Dynamic Simulations of Combined Transmission and Distribution Systems using Decomposition and Localization," *IEEE PowerTech*, 2013.

[15] S. Oh and S. Chae, "A Co-Simulation Framework for Power System Analysis," *energies*, vol. 9, no. 3, 2016.

[16] H. Jain *et al.*, "Integrated Transmission and Distribution System Modeling and Analysis: Need and Advantages," *IEEE PES General Meeting*, 2016.

[17] ——, "Three-Phase Dynamic Simulation of Power Systems Using Combined Transmission and Distribution System Models," *IEEE Transactions on Power Systems, Preprint*, 2016.

[18] R. Huang, R. Fan, J. Daily, A. Fisher, J. Fuller, " Open-Source Framework for Power system Transmission and Distribution Dynamics Co-simulation ," *IET Generation, Transmission and Distribution*, vol. 11, 2017.

[19] S.Ciraci *et al.*, "FNCS: A Framework for Power System and Communication Networks Co-Simulation ," *Proceedings of the Symposium on Theory of Modeling and Simulation*, 2014.

[20] J. Rocabert, A. Luna, F. Blaabjerg, and P. Rodriguez, "Control of power converters in AC microgrids," *Power Electronics, IEEE Transactions on*, vol. 27, no. 11, pp. 4734–4749, 2012.

[21] B. Tamimi, C. Canizares, K. Bhattacharya, "System Stability Impact of Large-Scale and Distributed Solar Photovoltaic Generation: The Case of Ontario, Canada," *IEEE Transactions on Power Systems*, vol. 4, no. 3, 2013.

[22] J.C. Boemer, E. Vittal, M. Rylander, B. Mather, "Derivation of WECC Distributed PV System Model Parameters from Quasi-Static Time-Series Distribution System Simulations," *IEEE PES General Meeting*, 2017.

[23] N.Miller, K. Clark, "Impacts of High Levels of Distributed PV and Load Dynamics on Bulk Power Transient Stability," *CIGRE International Colloquium on the Evolution of Power System Planning*, 2016.

[24] D. Ramasubramanian, R. Ayyanar, V. Vittal, J. Undrill, "Converter Model for Representing Converter Interfaced Generation in Large Scale Grid Simulations," *IEEE Transactions on Power Systems*, vol. 32, no. 1, 2017.

[25] T. Moshagen, "On meeting Energy Balance Errors in Cosimulations," https://arxiv.org/abs/1706.07273, 2017.

[26] M. H. Holmes, "Introduction to Numerical Methods in Differential Equations," 2006.

[27] G. Dahlquist, " Convergence and stability in the numerical integration of ordinary differential equations ," *Mathematica Scandinavica*, 1956.

[28] S. Khaitan and J. McCalley, "High Performance Computing for Power System Dynamic Simulation," *PowerSYS, Springer-Verlag Berlin Heidelberg*, pp. 43–69, 2015.

[29] P. C. Krause, "Analysis of electric machinery," 1986.

[30] F. Milano, "Power System Analysis Toolbox Documetation for PSAT version 2.0.0," 2008.

[31] R. C. Dugan, "Reference Guide, The OpenDSS," 2013.

[32] IEEE Task Force on Load Representation for Dynamic Performance, "LOAD REPRESENTATION FOR DYNAMIC PERFORMANCE ANALYSIS," *IEEE Transactions on Power Systems*, vol. 8, no. 2, pp. 472–482, 1993.

[33] ——, "Standard Load Models for Power Flow and Dynamic Performance Simulation," *IEEE Transactions on Power Systems*, vol. 10, no. 3, pp. 1302–1313, 1995.

[34] IEEE/CIGRE Joint Task Force, "Definition and classification of power system stability," *IEEE Transactions on Power Systems*, vol. 19, no. 2, pp. 1387–1401, 2004.

[35] B.-K. Choi, H.-D. Chiang *et al.*, "Development of Composite Load Models of Power Systems using On-line Measurement Data," *IEEE Power and Energy Society General Meeting*, 2006.

[36] A. Maitra, A. Gaikwad, P. Porbeik and D. Brooks, " Load model parameter derivation using an automated algorithm and measured data," *IEEE Power Energy Society General Meeting*, 2008.

142

[37] H. Renmu, M. Jin, and D. J. Hill, "Composite Load Modeling via Measurement Approach," *IEEE Transactions on Power Systems*, vol. 21, no. 2, pp. 663–672, 2006.

[38] H. Bai, P. Zhang, and V. Ajjarapu, "A Novel Parameter Identification Approach via Hybrid Learning for Aggregate Load Modeling," *IEEE Transactions on Power Systems*, vol. 24, no. 3, pp. 1145–1154, 2009.

[39] P. Regulski, D. Vilchis-Rodriguez, S. Djurovic, and V. Terzija, "Estimation of Composite Load Model Parameters Using an Improved Particle Swarm Optimization Method," *IEEE Transactions on Power Delivery*, vol. 30, no. 2, pp. 553–560, 2015.

[40] H. Wu and I. Dobson, "Cascading Stall of Many Induction Motors in a Simple System," *IEEE Transactions on Power Systems*, vol. 27, no. 4, pp. 2116–2126, 2012.

[41] J. Shaffer, "Air conditioner response to transmission faults," *IEEE Transactions on Power Systems*, vol. 12, no. 2, pp. 614–621, 1997.

[42] M. Paramasivam, A. Salloum, V. Ajjarapu, V. Vittal, N. B. Bhatt, and S. Liu, "Dynamic Optimization Based Reactive Power Planning to Mitigate Slow Voltage Recovery and Short Term Voltage Instability," *IEEE Transactions on Power Systems*, vol. 28, no. 4.

[43] WECC, "WECC Dynamic Composite Load Model Specifications," https://www.wecc.biz/Reliability/WECC%20Composite%20Load%20Model%20Specifications%2001-27-2015.docx, 2015.

[44] R. D. Quint, "A Look into Load Modeling: The Composite Load Model, Dynamic Load Modeling and FIDVR Workshop," https://esdr.lbl.gov/sites/all/files/6b-quint-composite-load-model-data.pdf, 2015.

[45] A. Gaikwad, P. Markham, and P. Porbeik, "Implementation of the WECC Composite Load Model for utilities using the component-based modeling approach," *IEEE Power Energy Society Transmission and Distribution Conference and Exposition*, 2016.

[46] P. Mitra, V. Vittal, P. Pourbeik, and A. Gaikwad, "Load Sensitivity Studies in Power Systems With Non-Smooth Load Behavior," *IEEE Transactions on Power Systems*, vol. 32, no. 1, 2017.

[47] P. Mitra and V. Vittal, " Role of Sensitivity Analysis in Load Model Parameter Estimation ," *IEEE Power Energy Society General Meeting*, 2017.

[48] M. Baran and F. Wu, "Network Reconfiguration in Distribution Systems for Loss Reduction and Load Balancing," *IEEE Transactions on Power Delivery*, vol. 4, no. 2, pp. 1401–1407, 1989.

[49] S. Kolluri and M. Peterson, "Application of Composite Load Model for FIDVR Studies in Entergy System," *IEEE Power Energy Society General Meeting*, 2016 http://resourcecenter.ieee-pes.org/product/-/download/partnumber/PESSLI1247.

[50] R. Argghandeh, "Micro-Synchrophasors for Power Distribution Monitoring, a Technology Review," https://arxiv.org/abs/1605.02813, 2016.

[51] A. von Meier, et al, "Precision Micro-Synchrophasors for Distribution Systems: A Summary of Applications," *IEEE Transactions on Smart Grid*, vol. 8, no. 6, 2017.

[52] S. Robles, "2012 FIDVR Events Analysis on Valley Distribution Circuits," *LBNL report by Southern California Edison*, 2013.

[53] A.R.R. Matavalam, et al, "Monitoring and Mitigation of Delayed Voltage Recovery using MicroPMU Measurements with Reduced Distribution System Model," https://arxiv.org/ftp/arxiv/papers/1810/1810.09510.pdf, 2018.

[54] W. Kersting, "Distribution Feeder Voltage Regulation Control," *IEEE Transactions on Industry Applications*, vol. 46, no. 2, pp. 620–626, 2010.

[55] D.P. Chassin, "ARRA Interconnection Planning - Load Modeling Activities - Report 24425 by PNNL," http://www.pnnl.gov/main/publications/external/technical_reports.

[56] Federal Energy Regulatory Commission, "Requirements for Frequency and Voltage Ride Through Capability of Small Generating Facilities," https://www.ferc.gov/whats-new/comm-meet/2016/072116/E-11.pdf, 2016.

[57] North American Electric Reliability Corporation, "Distributed Energy Resources: Connection Modeling and Reliability Considerations," http://www.nerc.com/comm/Other/essntlrlbltysrvcstskfrcDL/Distributed_Energy_Resources_Report.pdf, 2017.

[58] J.C. Boemer, M. Huque, B. Seal, T.Key, D.Brooks and C.Vartanian, " Status of Revision of IEEE Std 1547 and 1547.1," *IEEE Power Energy Society General Meeting*, 2017.

[59] S. Eftekharnejad, V. Vittal, G.T. Heydt, B.Keel and J.Loehr, "Impact of Increased Penetration of Photovoltaic Generation on Power Systems," *IEEE Transactions on Power Systems*, vol. 28, no. 2, 2013.

[60] V. Singhvi, P. Porbeik, J.C. Boemer and A. Tuohy, " Impact of High Levels of Solar Generation on Steady State and Dynamic Behavior of the Transmission System: Case Studies and Lessons Learned," *International Workshop on Integration of Solar Power into Power Systems*, 2015.

[61] Western Electricity Coordinating Council, "WECC Criterion: Transmission System Planning Performance, TPL-001-WECC-CRT-3.1," https://www.wecc.biz/Reliability/TPL-001-WECC-CRT-3.1.pdf, 2016.

[62] M. A. Pai, "Energy Function Analysis for Power System Stability," 1989.

[63] W. H. Kersting, "IEEE Radial Distribution Test Feeders," ewh.ieee.org/soc/pes/dsacom/testfeeders/testfeeders.pdf, 2000.